Dynamic Assembly of the Type-3 Secretion System in *Yersinia enterocolitica* Probed by Super-Resolution Fluorescence Imaging

Julian Michael Rocha
Lancaster, PA

B.S. in Chemistry, The George Washington University, 2013

A Dissertation presented to the Graduate Faculty of the University of Virginia in Candidacy for the Degree of Doctor of Philosophy

Department of Chemistry

University of Virginia
November 2019

Andreas Gahlmann
David Cafiso
Rebecca Pompano
Jill Venton
Hervé Agaisse

Dedicated

to my wife

and to my family

for their never-ending love and support

ACKNOWLEDGEMENTES

As I come to the end of my graduate career, there are many people that I must thank for their support in the pursuit of my education.

First, I need to start with my graduate advisor Dr. Andreas Gahlmann. We started this journey together at UVA from the beginning, stretching all the way back to our first visitation weekend before either of us had decided to make Charlottesville our home. Through the ups and downs of starting the research lab, we learned to settle into our individual roles of mentor and mentee. His enthusiasm for, and commitment to, his work and to his students is truly inspiring. I owe the success that I've had in my graduate school career to him and his unwavering support of our work. Now it is my turn to wish him success in battling Murphy, as he continues our work and expands his research group.

It is impossible to tell the story of my graduate school career without mentioning Dr. Charles Richardson. I had the privilege of working with our former post-doc Charles for the better part of my 5+ years here at UVA. Anyone who worked with Charles while he was here knows how significant he was in the day-to-day operations of the lab. Even without asking, he was always willing to lend a helping hand or provide his thoughts on a problem (sometimes especially without asking). Charles taught me much about science and research, but also about his general philosophy in life, explicitly or not. I am thankful for all of the experiences we shared during our time in the lab, and must also thank him for much of the success I've had in the projects we've worked on together.

I need to also acknowledge other members of the Gahlmann lab for their support and hard work. First, Mingxing and I started as the first two graduate students in Dr. Gahlmann's lab. While our work eventually diverged into different research projects, we

worked very closely in the first months after joining the lab. I must also thank our first undergraduates, Caroline and Eugene, for programming much of the initial MATLAB software necessary to begin work on the microscope, before I learned how to code. I need to also thank Ting for her help in data collection for fluorescent proteins early on. Ting was my desk-mate and partner-in-crime for the majority of my time here since she joined the lab in my second year. She is one of a kind and I will miss all the time we spent together over the past 4+ years. I'll be sure to continue to send her a post-card from wherever I may travel. I also thank Jackie for all of her help in testing the various diffusion analysis methods. Alecia, while juggling several projects, helped expand the scope of the work on the T3SS by branching out into effector/chaperone proteins. I wish her nothing but success in pursuit of that project and the rest of her work. Finally I want to thank Josh, who has helped me collect much of my most recent data after he joined the lab. I hope he finds success in his graduate school career as he carries on with my work on the T3SS.

Of course I need to thank my family, as they have continued to support me throughout my life. Without their support I would never have been able to pursue the level of education that I have and I would not be the person I am today. I need to especially thank my mom for being the rock-solid foundation of the family all of these years. Her love and dedication for me and all of her children is limitless, and I am extremely grateful to her.

Finally, I need to thank my wife, Katie, for her never-ending love and support. We have grown-up together over the past 11 years since we began dating, and have shared every experience together along the way. I would not have made it this far without the joy and energy she brings to me and everyone around her. She is my best friend, and I can't wait to experience all of the adventures of life together

ABSTRACT

The bacterial Type III Secretion System (T3SS) is a complex membrane spanning molecular machine comprised of over 20 different proteins. The T3SS is employed by pathogenic bacterial species to deliver effector proteins though a hollow needle-like structure, providing the mechanism of eukaryotic host cell infection. While effector proteins differ between species, the structural components of the T3SS remain largely conserved, making the machinery an attractive drug target. However, how secretion substrates are selected and transported by type 3 secretion remain unclear. Secretion activity and substrate selectivity are thought to be controlled by a sub-complex of the system located within the bacterial cytosol, called the sorting platform. Recent work has suggested that a dynamic interaction network of cytosolic sorting platform proteins play a role in effector protein secretion. To examine the diffusive behavior of sorting platform proteins within the bacterial cytosol, I employed 3D single-molecule localization microscopy on fluorescently labeled proteins in live *Yersinia enterocolitica* cells. To extract prevalent diffusive states of sorting platform proteins from a large population of single-molecule trajectories, I developed and thoroughly tested a diffusion analysis framework. By observing the prevalent diffusive states of sorting platform proteins in a variety of genetic backgrounds, we were able to construct a model on cytosolic sorting platform complex formation, further supporting the hypothesis that secretion is regulated through a dynamic interaction network of sorting platform proteins.

Table of Contents

Chapter 1: Introduction

1.1 Type 3 Secretion System

1.1.1 Overview

Bacteria have evolved a variety of specialized secretion systems to transport proteins and other molecules from the bacterial cytoplasm to the outside environment, into other bacteria, or into eukaryotic cells (1, 2). Secreted proteins play a role in a variety of functions, including quorum sensing, cell adhesion, and pathogenicity (2). Some proteins are transported out of the cell in a two-step process, first crossing the inner-membrane into the periplasm by the Sec or Tat pathway, and then across the outer membrane by a second secretion system, while others are transported outside of the cell directly from the cytoplasm by a secretion system spanning both the inner and outer membranes. There are at least nine secretion systems identified to date, referred to as the Type I through Type IX secretion systems, which serve a variety of functions ranging from cell survival to host cell infection (1).

The focus of this work is on the bacterial Type III Secretion System (T3SS), a dual membrane spanning molecular machine comprised of over 20 different proteins used by Gram-negative bacteria for flagellar biogenesis and for virulence (3, 4). The virulence-associated T3SS, also called the injectisome, features a long hollow needle that protrudes from the bacterial cell surface and ultimately anchors itself into the eukaryotic host cell membrane (**Fig. 1.1**) (5-9). The T3SS is employed by several prominent Gram-negative pathogens responsible for a variety of potentially fatal diseases, commonly involving intestinal infection, including *Salmonella*, *Yersinia*, *E. coli*, *Shigella*, and *Psuedomonas*

(10). The injectisome facilitates infection by delivering effector proteins from the bacterial cytosol into a eukaryotic host cell via the hollow needle structure. Effector proteins are species specific and serve a variety of functions, including re-arranging the host-cell actin cytoskeleton, evasion of the host cell immune response, and invasion of the host cell by the bacteria cell (8). While the effector proteins and their respective functions vary between bacterial species, the structural proteins of the T3SS are highly conserved. The secretion machinery is therefore an attractive drug target for combating infection, as well as potential re-programming of the system for various biomedical applications (10, 11). However, elucidating the functional mechanisms regarding delivery of effector proteins has been challenging due to the complex nature of the system as well as its relatively small size, leading to a deficiency in its structural characterization.

Injectisome structure

The injectisome can be broken into four distinct sub-complexes. The first is the membrane spanning rings that extend through both bacterial membranes. Using the commonly used universal nomenclature, the membrane rings are comprised of the proteins SctC, SctD, and SctJ (12). The membrane rings provide a channel through the membranes through which the rest of the machine can be built. The second is the inner membrane embedded export apparatus, comprised of SctR, SctS, SctT, SctU, and SctV (12). As its name suggests, the export apparatus is responsible for export of effector proteins through the third sub-complex, the extracellular needle. This is a hollow, needle-like structure approximately 60 nm in length that protrudes from the cell and includes a needle-tip

complex necessary for host cell detection and pore formation in the host cell membrane (13). The needle structure is primarily composed of SctF, but also includes the inner rod protein SctI, the hydrophilic translocase SctA, and the two hydrophobic translocases SctB and SctE (12, 14). Finally, there is a cytosolic complex associated with the T3SS at the inner-membrane interface, referred to as the sorting platform. As the nomenclature suggests, this sub-complex is believed to be responsible for sorting and selection of effector proteins for secretion. The sorting platform includes the five proteins SctK, SctL, SctN, SctO, and SctQ.

Injectisome assembly and function

Expression and assembly of the injectisome is triggered by a temperature jump to 37°C experienced upon entry into mammalian hosts (5). However, the assembly of the individual sub-complexes and the full injectisome are not completely understood – here, I will give a brief summary of the major assembly steps. A likely starting point of T3SS assembly is the construction of the export apparatus. It has been shown that the export apparatus can form, and is functional, in the absence of the other T3SS components (15-17). In the absence of the membrane spanning rings, the export apparatus can diffuse freely in the inner membrane (16), suggesting that the next logical assembly step would be insertion of the membrane rings around the export apparatus and subsequently embedding the complex in the peptidoglycan layer and outer membrane. Nonetheless, several studies have shown that the membrane ring complex also forms in the absence of the other T3SS proteins (18-21). Finally, the sorting platform associates with the complex, which requires

the membrane rings and, to a lesser extent, the export apparatus (22, 23). The sorting platform is required for the subsequent secretion of effector proteins.

A key feature of virulent T3SSs is that substrate selectivity follows a well-defined temporal hierarchy of early, middle, and late effectors (8). First, early effectors (SctF) are secreted through the system and built upon each other to construct the needle itself (24). Once the needle has reached a certain length, selectivity is switched to middle effectors (needle tip proteins and translocases). While the exact mechanisms of needle-length control and substrate switching is not fully understood, several proteins have been implicated in this process including the ruler protein SctP, the substrate switch protein SctU, and the inner rod protein SctI (14). Finally, there is a second switch to late effectors, or those responsible for host cell disruption, produced by host cell contact (7, 25). Notably, the switch to late effectors can be induced chemically by chelation of calcium in the *Yersinia* T3SS (26, 27), which will be utilized in this work to observe the two states of the system (i.e. secreting vs non-secreting). The switch arises after the translocases SctB and SctE form a pore in the host cell membrane, producing a conformational change in the needle which is transmitted to the base of the T3SS (28, 29). The gatekeeper protein SctW (25), which also binds effector-chaperone complexes (30), is then released from the cytosolic domain of the export apparatus, allowing secretion of late effectors.

Attempts to structurally characterize the intact injectisome have been stymied by its complexity and relatively small size. The entire injectisome is ~30 nm across at its widest point, therefore resolving the fine structure requires high resolution imaging techniques. Fortunately, a large portion of the intact complex, including the membrane

rings, the needle, and the export apparatus, can be purified and structurally characterized by cryo-electron microscopy (cryo-EM) (31-34). However, the purification conditions are too harsh to allow the sorting platform to remain intact, and therefore it was not possible to perform the same *in vitro* characterization of the cytosolic complex. Recent advancements in cryo-electron tomography (cryo-ET) technology, however, have permitted *in situ* visualization of the fully-assembled injectisome in bacterial mini-cells, which are small enough to be observed by cryo-ET (35-40). The sorting platform is the focus of the work presented in this dissertation and is discussed in detail in the following section.

1.1.2 Sorting Platform

A prominent model of T3SS functional regulation posits that selection of different export substrates is enabled through coordinated interactions among the cytoplasmic components of the injectisome (**Fig. 1.1**) (37, 41, 42). The cytosolic complex was termed 'sorting platform' after a complex of SctQ, SctL, and SctK was shown to bind chaperone-effector complexes in *Salmonella* in a temporal sequence consistent with the secretion substrate hierarchy (41). Furthermore, interactions between SctQ, SctK, SctL, and SctN are essential for type 3 secretion (4, 43-47) and for their mutual localization to the injectisome (22, 48, 49). As mentioned in the previous section, the precise structure of the sorting platform proteins SctK, SctQ, SctL, and the ATPase SctN within fully assembled injectisomes has recently been determined by cryo-electron tomography (37-39). The 3D tomogram averages reveal a cytoplasmic injectisome complex of hexametric symmetry,

which is notably different from the continuous cytoplasmic ring (C-ring) structure observed in flagellar T3SSs (50-52). SctQ is a homologue to the flagellar proteins FliM and FliN which form the C-ring, which is essential for flagellar rotation. In contrast, in the virulence-associated T3SS, SctQ localizes into six 'pods', but the functional role of such a pod structure in the secretion mechanism is not yet understood (36-40). Interestingly, SctQ has an internal translation start site, resulting in additional expression of the C-terminal fragment $SctQ_c$, the homologue to FliN (53, 54). Similar to their flagellar homologues FliM and FliN,(55) SctQ and $SctQ_c$ form complexes in a ratio of 1:2 (54), but reports on the requirement of $SctQ_c$ for T3SS functionality are conflicting (48, 54-57).

SctK associates with the inner membrane, and is the likely anchor to the T3SS for each individual pod (38, 58). Each pod further connects to one of six spokes of a cradle-like structure formed by SctL that holds in place the central hexameric ATPase SctN. SctL has been shown to exist as a dimer, which regulates ATPase activity (59). SctN has been shown to detach chaperones and unfold effectors prior to secretion (60).

In addition to the four main sorting platform proteins, SctO, also referred to as the stalk protein, binds to the ATPase SctN (61) and has also been shown to bind to effector protein chaperones (62). Little is known about the stalk protein, but its importance may be limited as it is not required for assembly of the other sorting platform proteins (22, 23, 38). In contrast, assembly of the remaining sorting platform proteins (SctQ, $SctQ_c$, SctL, SctK, and SctN) requires their mutual presence (22, 23). In *Salmonella* however, some assembly of the other sorting platform complexes was observed even in the absence of SctN and $SctQ_c$, indicating the possibility of species-specific differences (38, 57). While the exact

composition of the pods observed by cryo-ET is currently unknown, it is estimated that each pod consists of a SctK:SctQ: $SctQ_c$:SctL:SctN complex with 1:4:8:2:1 stoichiometry (23, 38, 49, 55).

The static *in situ* morphologies provided unprecedented insight into how SctK, SctQ, SctL, and SctN are arranged relative to each other when bound to the injectisome. However, recent studies have shown the sorting platform to be a highly dynamic structure, with rapid exchange of individual subunits (48). Therefore *in vivo* imaging techniques are required in order to probe beyond the static positioning of the sorting platform proteins and obtain insight into its dynamic function, such as how they are assembled and associate with the T3SS interface. More specifically, it is unknown whether the full sorting platform associates with the injectisome as a pre-assembled complex, or whether pods or even single proteins associate individually. We hypothesize that the sorting platform proteins participate in a dynamic interaction network of spontaneously forming complexes in the cytosol, where they may also interact with secretion substrates and their chaperones as a component of secretion regulation. Identifying the cytosolic interactions that functionally regulate type 3 secretion may guide future efforts in anti-virulence drug development. The work described here focuses on the motion behavior of the sorting platform proteins probed by super-resolution fluorescence imaging. The goal is to utilize single-molecule tracking (SMT) to detect diffusive cytosolic complexes of sorting platform proteins, which may play a vital role in the secretion process.

1.2 Outline

The primary method utilized here for analysis of T3SS proteins is Single-Molecule Localization Microscopy (SMLM), a super-resolution fluorescence imaging technique. Briefly, SMLM provides a method for extracting the positions of individual target molecules with a precision in the tens of nanometer range. By employing Single-Molecule Tracking (SMT) with data collected by SMLM, the motion behavior of individual proteins is visualized. This dissertation will detail the properties of SMLM and SMT in Chapter 2, and how they were realized in this work by construction of a fluorescence microscope. Chapter 3 describes data analysis for SMLM as well as a diffusion analysis framework I developed for SMT. The results, Chapters 4-6, are presented in the order in which they were published/completed, and focus on both the diffusion analysis framework itself, as well as results obtained on T3SS proteins by application of the framework. Finally, the overall significance and future direction of the work is described in Chapter 7.

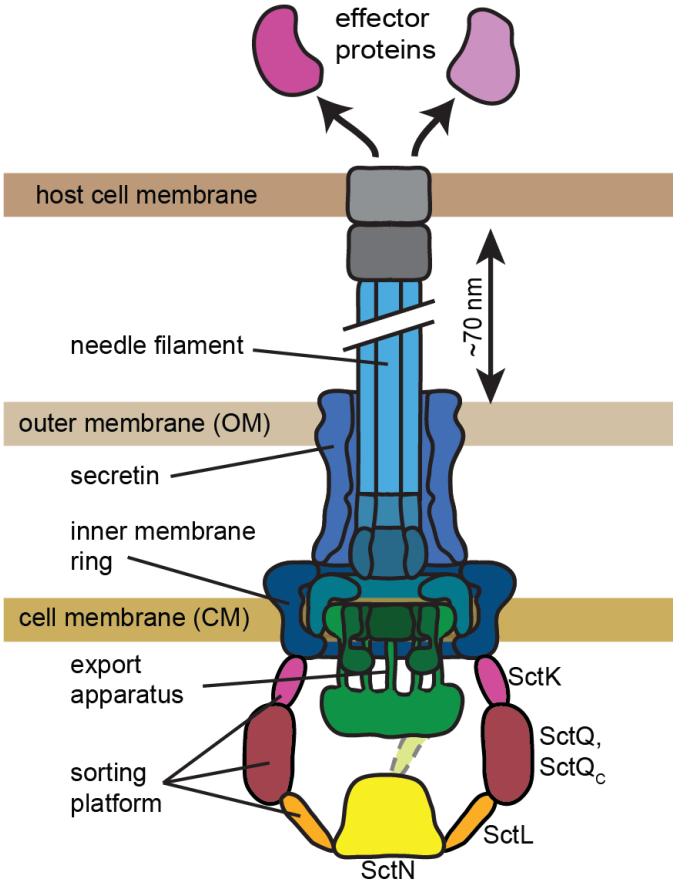

Fig. 1.1 The T3SS injectisome spans both the inner and outer bacterial membranes of Gram-negative bacteria and features a long hollow needle that protrudes away from the cell surface. The injectisome is used to transport effector proteins from the bacterial cytosol into the cytosol of eukaryotic host cells. At the cytoplasmic interface of the fully assembled injectisome, four interacting proteins (SctK,Q,L,N) are essential for the function of the T3SS and together form a so-called sorting platform. SctL forms a cradle-like structure that connects the hexameric ATPase SctN to each of the six pods, which contain multiple SctQ (and likely $SctQ_C$) subunits (38). SctK is an auxiliary protein that resides between the SctQ pods and the inner membrane ring of the injectisome. Figure adapted from Ref. (63).

Chapter 2: Super-Resolution Fluorescence Imaging

2.1 Super-Resolution Fluorescence Imaging

2.1.1 Single-Molecule Localization Microscopy

Fluorescence microscopy provides the means to observe molecules of interest in their native environment, making it a powerful tool for live cell imaging. However, fluorescence imaging techniques have traditionally been limited in their resolution by the diffraction limit. In an imaging system, each individual fluorescent emitter produces a point-spread-function (PSF) that is captured on a camera detector. Due to the effects of diffraction, the width of the observed PSF is much larger than the emitter itself, therefore emitters in close spatial proximity can have overlapping PSFs. In this case, it may be difficult or impossible to pin-point the exact position of each individual emitter. This limit was first described by Ernst Abbe in 1873 and is known as Abbe's diffraction limit:

$$d = \frac{\lambda}{2 \cdot n \cdot \sin\theta} \tag{2.1}$$

where d is the diameter of the PSF, λ is the wavelength of the emitted light, n is the refractive index of the medium the lens is in, and θ is the maximum half-angle of the cone of light entering the lens. The numerical aperture (NA) is equal to $n \cdot \sin\theta$, simplifying equation 2.1 to:

$$d = \frac{\lambda}{2 \cdot NA} \tag{2.2}$$

Given commonly used wavelengths and NA values of modern fluorescence microscopes, this translates to an experimental PSF diameter of ~250 nm. Therefore, it may be impossible to extract desirable information about a biological structure of interest with features smaller than this limit, as the resulting image would appear blurred.

To overcome the resolution limit for optical microscopy, several techniques achieving 'super-resolution' microscopy were conceived starting in 1994 and eventually awarded the Nobel Prize in Chemistry in 2014 (64, 65). Stefan Hell developed Stimulated Emission Depletion microscopy (STED) (64, 66, 67), while W.E. Moerner and Eric Betzig independently developed single-molecule localization microscopy (65, 68, 69). Super-resolution fluorescence microscopy can be categorized into two main approaches that rely on different mechanisms for distinguishing molecules within the diffraction limit. The first method relies on using engineered illumination patterns to selectively control and limit the emission signal to a specified volume. It was first demonstrated with the development of STED microscopy (66, 67). Typically, in STED experiments, the excitation beam is focused in the center of a second 'depletion' beam that is structured as a donut shape. Due to immediate stimulated emission from the excited fluorophores in the volume of the depletion beam, only fluorophores located at the very center of the donut shaped beam can emit fluorescence when excited by the excitation beam. A super-resolved image is achieved by scanning the beams across the sample, similar to laser scanning confocal microscopy. The principles of STED microscopy have been extended to other applications such as reversible saturable optical linear fluorescence transitions microscopy (RESOLFT) (70). Another widely-applied engineered illumination technique is Structured Illumination

Microscopy (SIM) (71, 72), which relies on a series of phase-shifted line patterns to obtain information at higher spatial frequencies that are not otherwise observable, thereby resolving structures with better resolution than the diffraction limit.

The work described in this dissertation utilizes the second approach, which relies on controlling the fluorescent emitter concentration in space and time. A mechanism (photophysical, photochemical, or chemical, discussed further below) ensures that only a small fraction of the fluorescent emitters are in a fluorescence 'on' state at any given time, while the majority are in a fluorescence 'off' state. In this way, the PSFs of the emitters are sparse in space and time and will not overlap. Thus, the localizations of the individual emitters can be extracted with a precision better than the optical diffraction limit. This technique is termed Single-Molecule Localization Microscopy (SMLM). SMLM offers precision in the tens of nanometer range with currently available fluorophores, greatly improving upon the diffraction limited resolution of ~250 nm. If sufficient point localizations are collected over time, a higher resolution image can be constructed to distinguish components that would not be resolvable in the diffraction-limited case. The precision of an individual localization, σ, is predominantly determined by the number of photons collected (i.e. more fluorescence photons provide higher localization precision) (73):

$$\sigma \approx \frac{s}{\sqrt{N}} \tag{2.3}$$

where *s* is the standard deviation of the PSF and *N* is the number of photons collected above background. The localization precision can also be experimentally estimated by calculating the standard deviation of multiple localization measurements of the same stationary

fluorescent emitter (74, 75). However, the overall resolution for a structure in a reconstructed image also depends on the labeling density (i.e. insufficient labeling can result in a 'missing' portion of a structure). This spatial resolution is quantified by the Nyquist criterion, given by:

$$\sigma_{Nyquist} = \frac{2}{\rho^{1/D}} \tag{2.4}$$

where ρ is the number of localizations per area/volume, and D is the dimensionality of the measurement (76, 77). In addition to structural determination, SMLM has been utilized for a variety of other quantitative measurements, including protein copy number counting (78), stoichiometry estimation in protein complexes (79), and co-localization experiments (80-82).

Several methods have been developed in recent years to achieve sparse emitter concentrations. For example, in fluorescence photo-activated localization microscopy (PALM), a photoactivatable fluorophore is utilized (83). These fluorophores require the use of a low intensity activation beam in order to convert a small fraction of fluorophores into a state capable of absorbing photons from a second excitation beam of longer wavelength and emitting fluorescence photons thereafter. By activating only a small portion of the emitter population, the fluorescing emitter concentration can be kept low. Another method, STochastic Optical Reconstruction Microscopy (STORM) relies on an activator-reporter fluorophore pair (74). The reporter is first switched into a dark state by illuminating with a red laser, and can be recovered by illuminating with a wavelength that will excite the activator. However, there is a strict requirement of close proximity (1-2 nm) between the activator and reporter. Molecular state-switching is also applied in direct

STORM (dSTORM), which utilizes organic dyes that exhibit photoswitching without the need for an activator dye (84, 85). In yet another approach, Point Accumulation for Imaging in Nanoscale Topography (PAINT), the fluorescent probe enters an 'on' state only after integrating into a membrane. Certain fluorescent proteins, such as eYFP, undergo photoinduced activation/blinking when illuminated with high intensity excitation light (68, 86).

2.1.2 Fluorescent labeling of target molecules

When designing an experiment for super-resolution fluorescence microscopy, it is important to choose an appropriate labeling method and fluorophore for the application. Fluorescent proteins and fluorescent dyes each provide several key advantages and disadvantages. The most attractive feature of fluorescent proteins is their ability to be genetically encoded and covalently linked to a target protein. Fluorescent protein expression can be achieved *in trans* using expression plasmids, or through genetic incorporation into the chromosomal DNA. Genetic encoding guarantees high specificity and complete labeling of all target protein molecules. A disadvantage of fluorescent proteins is their ~10 times lower fluorescence brightness compared to organic dyes. Since the resolution of the measurement is proportional to the number of collected photons, as given by Eqn 2.3, a lower photon yield results in poorer localization precisions. Additionally, fluorescent proteins are much larger than dyes (~25 kDa to <1 kDa respectively), producing a higher potential for perturbing the system through steric effects. While fluorescent dyes themselves are small, they still require an additional linker to label

the target. For example, fluorescent dye-conjugated antibodies or antigen-binding fragments (FAB) can be used to label a structure after chemical fixation and permeabilization of the sample (87). Live-cell dye staining can be achieved with genetically encoded tags such as the SNAP-, CLIP-, and Halo-tags (88-90). However, chemical dye labeling may result in incomplete labeling of the target protein and/or high background levels if excess dye is not sufficiently removed in one or several wash steps. As is the case for fluorescent proteins, the relatively large size (~20-30 kDa) of SNAP-, CLIP-, and Halo-tags may also be prohibitive depending on the application.

2.1.3 Emitter Localization by PSF Fitting

As mentioned previously, in order to achieve super-resolution levels of imaging, the PSFs must not overlap. Several methods have been developed to extract the emitter localizations from non-overlapping PSFs, the simplest of which includes simply finding the centroid of the intensity profile of the PSF (73). A commonly utilized method involves fitting the PSF to a two-dimensional Gaussian profile by a Least Squares (LS) estimation (65, 91, 92). A more precise method has been developed that uses Maximum Likelihood Estimation (MLE) of the position of a fluorophore (93). MLE is able to achieve the Cramér-Rao Lower Bound (CRLB), the information theoretical limit of best precision, for the fitted parameters, even for non-Gaussian noise distributions. While these methods have been developed for non-overlapping emitters, other algorithms have been developed for fitting of highly overlapping PSFs (94-97), which relax the experimental requirement of spatially

separated emitters and allow for acquisition of more data points in a shorter amount of time.

2.1.4 Optical Engineering of the PSF

Several methods developed using engineered PSFs exhibiting specific shapes to allow for extraction of not only the x,y position, but also the z position. Two commonly used examples of engineered PSFs include the astigmatic (75) and the double-helix (98, 99) PSFs. The astigmatic PSF is elliptically elongated in either the x or y direction, depending on whether the emitter is located above or below the focal plane. The elliptical extent and orientation provides information on the emitter's z position. Different from the astigmatic PSF, the double-helix PSF (DHPSF) exhibits two lobes. The midpoint between the two lobes provides the x,y localization of the emitter. The two lobes rotate around the mid-point as the emitter moves away from the focal plane, therefore the degree of rotation provides the z position. In addition to these examples, there exists several other engineered PSFs for 3D localization including the tetrapod (100), corkscrew (101), bisected-pupil (102), and a side-lobe free self-bending PSF (103). The microscope used in this dissertation employs the DHPSF.

2.1.5 Phototoxicity and Photobleaching

A major advantage of fluorescence microscopy is the ability to image in live cells, because the sample does not necessarily need to be fixed (chemical fixation, frozen, etc). However, in live cell imaging, the phototoxic effects of high-intensity excitation light must be considered. Damage induced by exposure to light can alter the physiology of the cell or even cause cell death (104, 105). The major cause of phototoxic effects is the production of reactive oxygen species (ROS), created after naturally occurring molecules within the organism absorb visible light and subsequently react with oxygen. ROS can cause a variety of issues, including damage to DNA, proteins, and lipids by oxidation. Additionally, fluorophores utilized in fluorescence microscopy can also become oxidized and degraded in a process known as photobleaching, which may also produce ROS. The effects of ROS can be limited with addition of antioxidants such as ascorbic acid to the imaging media (106, 107). Another way to reduce production of ROS is by limiting the amount of excitation light illuminating the sample. For example, in Adaptive Light-Exposure Microscopy, the excitation light is actively adjusted to focus only on areas of the cell where there is observed fluorescence (108). In Total Internal Reflection Microscopy (TIRF), the excitation laser is brought into the objective at a high angle, so that the laser is totally internally reflected, producing an evanescent wave that only excites ~100 nm into the sample volume. Not only does TIRF microscopy have the benefit of limiting phototoxic effects, but can also increase image resolution by limiting emitter concentration (109). Finally, light sheet fluorescence microscopy limits the excitation volume by illuminating with a thin sheet of light that sections through the sample (110-117). For the work presented

in this dissertation, we limited exposure of the samples to high-intensity excitation laser for only a few minutes. We confirmed that living cells imaged under such conditions were still able to divide on the coverslip (118).

2.1.6 Single-Molecule Tracking

In contrast to high resolution imaging methods that require fixed samples, such as cryo-Electron Microscopy (cryo-EM), super-resolution fluorescence microscopy provides the ability to observe target molecules in live cells. The ability to probe the positions and motions of single molecules in living cells has made single-molecule localization and tracking microscopy a powerful experimental tool to study the molecular basis of cellular functions (65, 74, 83). Single-Molecule Localization Microscopy has the unique ability to probe the motion behavior of individual molecules by combining their spatial and temporal information to create a trajectory for each individual molecule. Information such as the apparent diffusion coefficient or the molecular displacements between each time point can be calculated for each detected single molecule. Single-molecule trajectories, if sampled in sufficient numbers, provide the full distribution of molecular motion behavior in cells, and statistical analyses of localization and trajectory data can been used to resolve the prevalent diffusive states as well as their population fractions. A key benefit of tracking single molecules is that individual trajectories can be sorted according to predefined (quality) metrics, for example, to include only non-blinking molecules (119), or molecules localized in specific subcellular regions of interest (120). These advantages are not shared by ensemble-averaged measurements such as fluorescence recovery after photobleaching

(FRAP) and fluorescence correlation spectroscopy (FCS) (121). In the simplest case it is possible to distinguish stationary from mobile molecules. For example, DNA bound lac repressors in search of their promoter region appear stationary at 10 ms frame rates and can thus be clearly distinguished from unbound lac repressors which explore the entire *E. coli* cell volume on the same timescale (122). Similarly, the *E. coli* chromosome-partitioning protein MukB forms stationary clusters only when incorporated into the quasi-static DNA-bound structural maintenance of chromosomes (SMC) complex (123). Single-molecule tracking provides a tool for observing these different states directly, and sophisticated analyses are not required to resolve them. However, other proteins, in particular those involved in delocalized regulatory and signaling networks, may not exhibit such stationary states. These proteins may instead form oligomeric complexes of varying sizes that diffuse at measurably different rates (124-128). A major objective for single-molecule tracking microscopy is therefore to resolve the different diffusive states that manifest in the cytosol of living cells. Extracting this information, however, is difficult in the presence of several diffusive states, and there are many factors that must be taken into consideration. Such cases require an integrated approach in terms of data acquisition, processing and analysis.

Several methods have been developed for extracting the diffusive states and their relative population fractions from single-molecule tracking data (124, 128-135), but there is no consensus in the field as to the most effective approach. As part of the work for this dissertation research, a diffusion analysis framework was developed for extracting the relevant information from short single-molecule trajectories. This approach relies on

Monte Carlo simulations of single-molecule trajectories in the confined volume of a bacterial cell to build a model for confined Brownian motion that is then fitted to match experimental data. A full description of the framework, its applications, and its limitations is found in Chapters 3 and 5.

2.2 Instrumentation

To perform 3D single-molecule localization microscopy, a custom-built microscope was constructed. The microscope consists of excitation and emission pathways for collection of signal from fluorescent emitters, as well as a phase contrast pathway for collecting images of bacterial cell shapes. The following sections will explain the specific details of each pathway.

A custom microscope is advantageous compared to a commercial instrument in several key aspects. First, the up-front cost to build the instrument is significantly reduced compared to purchasing a similar commercial instrument. Second, the costs in servicing the instrument over time are reduced as well, as there is no requirement for external maintenance providers. Members of the research group develop a deep working knowledge of the instrument, so they can service it themselves and therefore avoid long waiting periods for maintenance and alignment otherwise. Third, a custom instrument provides full flexibility in terms of its design and use. For example, the microscope constructed for this research has superior stability than commercial instruments, because the microscope objective is fixed in place while the sample stage itself is scanned by an automated piezo-electric stage. This is in contrast to commercial instruments, where the stage is fixed and

the objective is placed on a height-adjustable objective turret. Such a configuration is more prone to sample stage drift. Finally, home-written, customizable software provides the ability to tailor the experimental data collection to specific experimental requirements.

2.2.1 Fluorescence Imaging

Fluorescence microscopy requires excitation of the sample with an emitter-specific wavelength of light (given by the absorption spectrum), and the subsequent collection of emitted light from the sample with a longer wavelength than the excitation light due to the Stokes shift. Therefore, the fluorescence pathway of the microscope can be broken down into the excitation and emission pathways. The microscope contains three lasers with different wavelengths in the excitation pathway. A 514 nm laser (Coherent Genesis MX514 MTM) and a 561nm laser (Coherent Genesis MX561 MTM) is used for excitation of fluorescent emitters, while a 405 nm laser (Coherent OBIS 405) is used to 'activate' photo-activatable fluorescent emitters prior to excitation with the 561 nm laser. The configuration described here was designed to perform optimally with the fluorescent proteins eYFP (excitation with 514 nm laser) and PAmCherry1 (activation with 405 nm laser and subsequent excitation with 561 nm laser). Each laser begins in a separate excitation pathway. The input laser beam is first expanded by a two lens telescope to create a collimated laser beam with a larger size than the input. The beam then passes through a wavelength-appropriate zero order quarter wave plate to circularly polarize the excitation laser. Additionally, there is a band-pass filter in the 514 nm laser excitation pathway

(Chroma ET510/10bp) to limit the excitation wavelength range. All excitation laser lines are then combined into the same excitation pathway using a set of dichroic mirrors (Chroma T470lpxr and Chroma T525lpxr). Using additional mirrors, the excitation light is directed towards another dichroic mirror (Chroma ZT405-440/514/561rpc-UF1) that allows excitation light to be reflected into the microscope objective (UPLSAPO 60X 1.4 NA), which focuses the light onto the sample. The sample is mounted on a xyz nano-positioning stage (Mad City Labs), which can position the sample with nanometer precision. A drop of immersion oil is placed between the objecting and the cover slip (VWR #1.5, 22mmx22mm) that the sample is mounted on. The immersion oil has a higher refractive index (1.515) compared to air (1) to better match the refractive index of the glass cover slip holding the sample. The diffraction-limited resolution, r, is dependent on the numerical aperture (*NA*) of the lens and is generally given by:

$$r = \frac{0.61 \cdot \lambda}{NA} \tag{3.5}$$

where λ is the wavelength of light. Note that this is similar to Eqn. 2.2, with a different multiplication factor (0.61 instead of 0.5), to account for physical limitations and properties of the lenses. The *NA* is given by:

$$NA = n \cdot \sin\theta \tag{3.6}$$

where θ is the maximum half-angle of the light that can pass through the lens and n, is the index of refraction of the medium which the light passes through before reaching the sample. Therefore, a higher refractive index produces a higher *NA*, resulting in higher resolving power.

After the sample is excited by the excitation laser, the resulting fluorescent signal emitted by the fluorophores is collected by the objective lens, entering the emission pathway after passing back through the dichroic mirror (Chroma ZT405-440/514/561rpc-UF1). The emission signal passes through a series of filter sets including a 514 nm long-pass filter (Semrock LP02-514RU-25, 561 nm notch filter (Semrock NF03-561E-25), and a 700 nm short-pass filter (Chroma ET700SP-2P8). The 514 nm long-pass filter and 561 nm notch filter are used to limit the amount of scattered excitation light entering the emission pathway from the 514 nm or 561 nm excitation lasers, respectively. The 700 nm short pass filter is simply to limit any additional light outside of the range of the fluorescence signal from entering the emission pathway.

All objective lenses used in this work are infinity corrected objective, meaning the image plane is at infinity. Therefore a second lens, referred to as the tube lens, must be placed into the optical path to obtain the image plane. Before the image is formed on the camera detector, the signal is passed through two more lenses, in a configuration known as a 4f system (**Fig. 2.1**). The 4f lenses are achromatic doublet lenses, which help limit effects of chromatic and spherical aberration. The main advantage of inserting a 4f system here, however, is the ability to access the Fourier (pupil) plane in between the two lenses. Here this advantage is utilized by multiplying the Fourier transform of the image (the first lens performs a Fourier transform of the image) by the Double-Helix Point-Spread-Function (DHPSF) transfer function. This is achieved by placing an optics piece, the phase mask (Double Helix LLC), in the Fourier plane of the 4f system (99, 136). The second lens converts the Fourier transform of the image back into the real image. The image observed

on the camera detector now exhibits the DHPSF instead of the normal Gaussian-like PSF. As described at the beginning of Chapter 2, the DHPSF is advantageous as it allows for 3D localization of a fluorescent emitter, compared to the normal PSF which allows for only 2D localization. An in-depth description of the DHPSF and a comparison to the conventional PSF is given in Section 3.1.

Fluorescence is recorded on scientific Complimentary Metal-Oxide Semiconductor (sCMOS) detectors (Hamamatsu ORCA-Flash 4.0 V2). In the past, it was common practice to use electron-multiplying charge coupled device (CCD) cameras for single-molecule localization microscopy. However, in recent years sCMOS cameras have become increasingly popular due to their quicker read times and larger fields-of-view (FOV) at comparable noise levels and detection quantum efficiencies.

A dichroic beam-splitter (Chroma T560lpxr-uf3), placed in the emission pathway after the first 4f lens, divides the emission pathway into a ‘red’ and ‘green’ pathway, each with a dedicated camera detector. The microscope was designed in this way for quickly switching between color channels or simultaneous dual-color imaging. An additional 561nm notch filter (Chroma ZET561NF) was inserted into the ‘red’ channel to block scattered laser light.

2.2.2 Phase Contrast Imaging

In addition to images collected for fluorescence signal, a phase contrast image is acquired for each FOV. Phase contrast microscopy has been widely used for decades, with

Fritz Zernike first describing the method in 1934 (137). A major advantage of phase contrast microscopy is that it permits imaging of structural properties of live cells and does not require fluorescent labeling. For the work described in this thesis, phase contrast microscopy is used to extract the bacterial cell outlines and positions of cells imaged with fluorescence microscopy. The cell outlines are used in post-processing to assign each single-molecule localization obtained from the fluorescence pathway to a specific cell.

A red light-emitting diode (LED) is used as an illumination source for the phase contrast pathway, which sits upon an illumination tower above the inverted microscope stage. After passing through a set of lenses, the illumination light is then passed through an annulus ring, which produces a ring of light. A condenser lens then focuses the ring of light onto the sample stage. As the light passes through the sample, light entering the area of the biological sample can be scattered, while light passing through the surrounding area is unaffected. Importantly, light scattered by the biological material will be phase shifted by -90°, and will be scattered in all directions. The light then travels down through the objective lens and the tube lens. Now, however, instead of travelling through the fluorescence emission pathway, the light is reflecting into a separate pathway by utilizing a 'flip mirror' that can be electronically raised to switch between fluorescence and phase contrast imaging. The light then passes through another 4f system. In this case, an optics piece known as the phase ring is placed in the Fourier plane between the two 4f lenses (**Fig. 2.1**). Here, light that has not been scattered by the sample will pass through the ring, and be phase shifted by +90°, while most of the scattered light will not pass through the ring and will not be phase shifted. The total phase shift of 180° will cause destructive

interference between the background and scattered light. When viewed on the camera detector (Aptina MT9P031), this will result in the sample appearing darker than the light background.

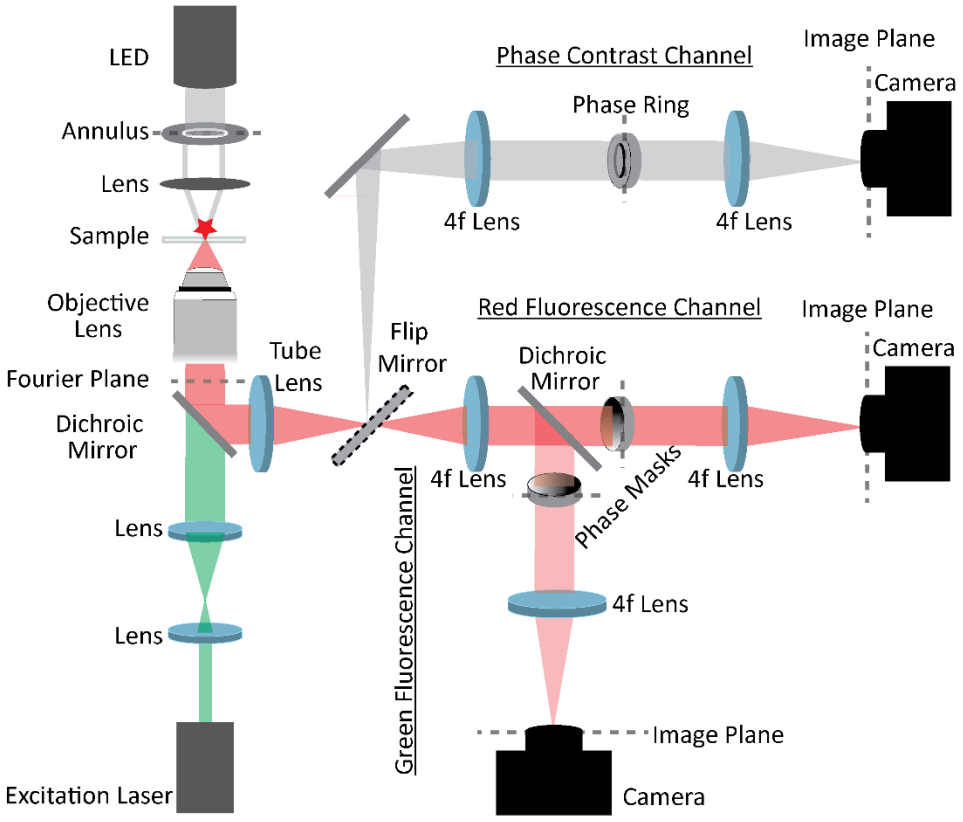

Figure 2.1. Optical diagram of microscope pathways. The excitation pathway (green) directs the excitation laser into the objective lens. Light collected by the objective from the sample is directed into the emission pathway (red). A motorized 'flip-mirror' is used to switch between the fluorescence (red) and phase contrast (grey) pathways. The fluorescence pathway is further split into a 'red' and 'green' fluorescence channel by a dichroic mirror. The camera detectors, excitation lasers, LED, and 'flip-mirror' are controlled remotely by computer.

Chapter 3: Data Processing and Analysis

Data collected by the super-resolution fluorescence microscope, detailed in the previous chapter, is in the form of raw images, which must pass through a series of data processing and analysis techniques to extract meaningful information. As part of the work for this dissertation, the author wrote a substantial amount of MATLAB code to perform the analysis in this section. With the exception of the Easy-DHPSF code (138), which was modified from a published work from the Moerner lab, these programs were written from scratch by the author. In a first step, single-molecule localizations are found by analyzing the fluorescence intensity signals on the raw images. Each localization has an x, y, z spatial coordinate as well as a time stamp of detection. Once localizations are found they are further analyzed to obtain additional information, such as their cellular distribution and the movement of individual proteins. This chapter will detail the initial image processing steps to obtain the localizations, as well as the subsequent analysis steps. The full experimental workflow, including data collection, processing, and analysis is found in Ref. (118).

3.1 Point-Spread-Function Fitting

As described in Chapter 1, single-molecule localization microscopy requires the extraction of point localizations from well separated point-spread-functions (PSFs). A common approach for localization extraction is fitting of the PSF with a Gaussian model, typically utilizing a Least Squares (LS) estimation. However, as detailed in Chapter 2, the PSF for the microscope used in this work is altered to the Double-Helix Point-Spread-Function (DHPSF), therefore simply fitting with a single Gaussian profile is not sufficient. Instead, the DHPSF is fit with a double-Gaussian model, fitting each of the two lobes with

a Gaussian shape. A MATLAB software package called Easy_DHPSF was released by the Moerner laboratory (138). The Easy_DHPSF code fits the DHPSF with a double-Gaussian model using a LS estimator. The fitting relies on a calibration of the DHPSF behavior obtained by scanning a bright fluorescent bead over a large (~2-3 μm) axial range to create a series of template images for different z positions. Potential DHPSF signals are found within the full experimental image by performing a template matching step. Finally the potential DHPSF signals are fit using the double-Gaussian model. In addition, fit localizations are further filtered by certain quality metrics such as lobe distance, lobe intensity ratio, lobe diameter, and photons collected. As the work on this software has already been published elsewhere, I will not go into further detail here, but will focus on the modifications we have implemented for processing our experimental data.

The first modification we made was incorporation of a Maximum Likelihood Estimator (MLE) for the double-Gaussian fitting to extract the single-molecule localizations. As stated in Chapter 1, MLE is able to achieve the Cramér-Rao Lower Bound (CRLB), the theoretical limit of precision, for the fit parameters (93). As the name suggests, the algorithm estimates the most likely value for the fit parameters, such as the width of the Gaussian blob used to fit and the x,y positions of the emitter. LS, on the other hand, finds the set of parameters that produces the least difference. Generally, MLE has been shown to be a more robust estimator for fitting of single-molecule localizations than LS, especially when modeling inaccuracies and noise levels are limited (139). In the application here, the performance of MLE is enhanced since the appropriate noise and gain statistics

for each individual pixel on the sCMOS detector are considered, as described in the following sections. MLE is implemented as described in Ref. (140).

A second modification was an addition of a different background estimation strategy. One of the key image processing steps is to subtract a background image from the full image. The signal-to-noise ratio produced in SMLM is low (~2), therefore it is crucial that the background image is estimated correctly. Sources of background intensity include light from the illumination laser, as well as inherent cell auto-fluorescence. The initial Easy_DHPSF software utilized a wavelet background estimation. However, a problem that may arise in fluorescence imaging of biological samples is the presence of persistent, structured background, such as in the case of cellular auto-fluorescence. A wavelet background estimation cannot accurately remove this type of background. Therefore, in our version we have added the option to use a median background estimator instead (141). As the name suggests, the median filter finds the median image for a rolling window of 100 frames surrounding the frame of interest. Single-molecules only produce signal for an average of ~6 frames. Because they are not in a fluorescence state for the majority of the 100 frame window, single-molecule signals will not be filtered out when the background is subtracted, but any persistent background will be.

The original Easy_DHPSF code was written for processing data collected with a Charged-Couple Device (CCD) camera detector, and it implemented a method for handling the camera gain. The gain is an amplitude ratio of the input electrons (photons are converted to electrons at some probability, termed the Quantum Efficiency) to the output detector value (i.e. a gain of 1.5 means that on average 1 electron produced a detector count value

of 1.5). For a CCD detector there is only a single gain value for the entire camera. However, scientific Complementary Metal–Oxide–Semiconductor (sCMOS) cameras were used for the work presented here, due to their high reading rates and larger fields-of-view (140, 142, 143). For sCMOS detectors, each pixel has its own unique value for the gain, which must be carefully calibrated. Therefore we made modifications to the code to load in a calibration file and use it to convert units of detector counts to photons. The gain for each pixel was estimated as described in Ref. (140).

3.2 Localization Analysis

3.2.1 Single-Molecule Localization and Cell Registration

Single molecule localizations were assigned to individual cells based on the corresponding phase contrast image. Cell outlines were generated based on the phase contrast images using the open-source software OUFTI (144). The outlines are registered to the fluorescence data by a two-step 2D affine transformation using the 'cp2tform' function in MATLAB. In the first step, five control point pairs were manually selected by estimating the position of the cell poles based on single-molecule localization data and the cell outlines generated by OUFTI. An initial transformation was generated, and cell outlines containing less than 10 localizations were removed. The center of mass for all remaining cell outlines and single-molecule localizations within them were then used to generate a second, larger set of control point pairs to compute the final transformation function. A large set of control points ($N \sim 100$ cells) ensures that cells with few

localizations or cells positioned partly outside the field-of-view do not skew the transformation. Only localizations that lie within the cell outlines were considered for further analysis.

3.2.2 Spatial Analysis of Localizations

Radial distributions of single-molecule positions were created using a combination of the cell outlines found with OUFTI and the localizations themselves. The localizations from the full FOV were separated and assigned to specific cells using the cell outlines from OUFTI. The localizations from each cell were further assigned to sections along the long axis of the cell. The central axis of each section was then found by projecting the localizations onto a 2D plane and finding the centroid of the localizations. The localizations were grouped into sections in this way to limit effects of cell curvature on the centroid of the 2D projected localizations. The radial distances were then found by calculating the distance of each 3D localization to the computed central axis.

3.3 Diffusion Analysis

Assigning a single molecule to a specific diffusive state is challenging, especially for fast diffusing cytosolic species. The molecular displacements measured in single-molecule tracking can be used to compute apparent diffusion coefficients for each detected single molecule, but these estimates are prone to large errors, particularly when the

trajectories are short and the number of available molecular displacements are low (126, 145). Short trajectories (<20 displacements) are the norm in live-cell single-molecule tracking with genetically encodable fluorescent protein labels. However, genetically encoded fluorescent proteins offer unmatched labeling specificity and efficiency and therefore remain preferable when off-target labeling with chemical dyes may lead to artifacts (146).

Additionally, the environment surrounding the diffusive molecule must be considered. Particularly relevant to bacterial cell imaging is restriction placed on diffusive cytosolic molecules motion by the cell boundaries. For slowly diffusing molecules in bacteria, it is possible to resolve multiple diffusive states by fitting the experimentally measured distributions of molecular displacements, r, or apparent diffusion coefficients, D^*, using analytical equations describing Brownian, i.e. normal, diffusion (126, 145, 147-149). Such analytical approaches produce acceptable results only if biomolecular motion is slow enough that confinement effects can be ignored. During the time length of a typical trajectory in single-molecule fluorescence microscopy experiments (~100 ms – 1 s), a cytosolic molecule undergoing Brownian motion at a diffusive rate of an unbound fluorescent protein (~10 $\mu m^2/s$) is likely to collide with the cell boundary multiple times. As a result, observed motion of cytosolic proteins in bacteria is strongly confined by the cell boundaries and molecular displacements will, on average, be smaller than those expected for unconfined diffusion. Approaches assuming unconfined Brownian motion are therefore not suitable when tracking fast diffusing molecules in the cytosol of bacterial cells. In contrast, the confinement effect is less pronounced in the larger volume of a eukaryotic cell. However, even utilizing an engineered PSF to allow for 3D localization

will only allow imaging through a depth of ~2-3 μm, therefore freely diffusing molecules in the cytoplasm of a eukaryotic cells may be lost during the course of a trajectory.

Section 3.3 details a diffusion analysis framework that I to extract relevant information, such as the prevalent diffusive states and their relative population fractions, from short single-molecule trajectories in the confined volume of a bacterial cell.

3.3.1 Single-Molecule Tracking

To determine the apparent diffusion coefficients of single molecules, 3D single-molecule localizations in subsequent frames were linked into trajectories using a distance threshold of 2.2 μm. This threshold was determined by calculating the furthest distance a molecule traveling at 20 $\mu m^2/s$ (~2 times the rate of a free fluorescent protein) in 25 ms (typical exposure time), with a 25% buffer in case of localization error. Only trajectories with at least 4 localizations were considered for further analysis. In addition, if two or more localizations were present in the cell at the same time during the length of the trajectory, the trajectory was not considered for further analysis. These steps minimized the linking problem, in which, due to misassignment, two or more molecules could contribute to the same trajectory (150).

The Mean Squared Displacement (MSD) was calculated according to

$$MSD = \frac{1}{N-1}\sum_{n=2}^{N}(x_n - x_{n-1})^2 \tag{3.3}$$

where N is the total number of time points and x_n is the position of the molecule at time point n. The apparent diffusion coefficient, D^*, of a given single-molecule was then computed as

$$D^* = \frac{MSD}{2 \cdot m \cdot \Delta t} \tag{3.2}$$

where m is the dimensionality and Δt is the camera exposure time. In our experiments m=3 and Δt =25 ms. It is important to note that the so-estimated single-step apparent diffusion coefficients do not take into account the static and dynamic localization errors (145), or the effect of confinement within the bacterial cells. Instead of accounting for these effects using analytical models (151, 152), we generated simulated noise and motion-blurred images of diffusing molecules in rod-shaped cell volumes, as described in the following section. The resulting images were then analyzed in the same manner as experimental data. These steps ensured that static and dynamic localization errors and the effect of confinement within the bacterial cells were accurately modeled.

3.3.2 Monte-Carlo Simulations

Calculation of the apparent diffusion coefficients for a large number of tracked molecules will result in a distribution of values even if molecular diffusion is governed by a single diffusive state. In addition, for confined diffusion within small bacterial cell volumes, the movement of molecules is restricted in space. Such confinement results in an overall left shift of the apparent diffusion coefficient distributions for a given diffusive

state (**Fig 3.1a**, dashed lines). The shape of the confined distribution is dependent on the size and shape of the confining volume.

To resolve the unconfined diffusion coefficients of predominant molecular complexes in living cells based on the experimentally measured distribution of apparent diffusion coefficients, we performed Monte Carlo simulations of confined Brownian motion inside the volume of a cylinder using a set of 64 diffusion coefficients ranging from 0.05–20 $\mu m^2/s$ as input parameters. The size of the confining cylinder was chosen to match the average size of a *Y. enterocolitica* cell (radius = 0.4 μm, length = 5 μm). The apparent diffusion coefficient distribution for the average cell length and width are not different from the distribution arising from a population weighted distribution of cell sizes (**Fig. 3.2a**). While a rod-shape bacteria more closely resembles a spherocylindrical shape, the apparent diffusion coefficient distributions in a spherocylinder were indistinguishable from those in a cylinder of the same length and radius (**Fig. 3.2b**). The starting position of the trajectory was randomly set within the volume of the cylinder and Brownian motion was simulated using short time intervals of 100 ns. We assumed a hard sphere reflection at the cell boundaries, i.e. if a molecule was displaced outside of the volume of the cylinder within a time step, it was redirected back towards the inside of the cylinder at a random angle. Choosing a short time step further ensured that the entire volume of the cylinder could be sampled by the diffuser, even the interfacial region near the cell boundary.

To simulate the raw experimental observable, we generated noisy, motion-blurred single-molecule images. Specifically, we generated DHPSF images corresponding to 50 periodically sampled positions of a molecule during the camera exposure time (25ms) and

then summed these 50 sub-images to obtain the motion-blurred DHPSF images, which when analyzed will produce position estimates with limited accuracy and precision due to dynamic localization error (145). The photon count of each simulated image was scaled to match the experimentally measured distribution for eYFP photon counts and a laser background of ~13 photons/pixel was added. Poisson noise was added to the image based on final photon count in each pixel. Finally, a dark offset (50 photons/pixel on average) with Gaussian read noise (σ ~1.5 photons) was added to produce the final image. This image was then multiplied by the experimentally measured pixel-dependent gain of our sCMOS camera to obtain an image in units of detector counts. These simulated images were then processed the same way as experimental data to obtain single-molecule localizations, which were then linked into trajectories. Simulated trajectories were limited to six displacement steps to match the average length of our experimentally measured trajectories.

By explicitly simulating spatially blurred emission profiles with realistic signal to-noise ratios, we can account for both static and dynamic localization error (**Fig 3.3**). Static localization error is the result of finite numbers of fluorescence signal photons that provide an imprecise measure of the PSF shape and thus result in single-molecule localizations of limited precision (65). Dynamic localization errors manifest for moving emitters that generate motion-blurred images on the detector (**Fig 3.1b inset**). When analyzed using common fitting algorithms (which are based on data fitting to well-defined PSF shapes), motion-blurred images provide 2D or 3D position estimates with limited accuracy and precision (153). If the motion blur is too severe, then the point-spread-function (PSF) of

the molecule may become too distorted to result in a successful fit. Motion blur therefore limits the detection efficiency of fast diffusing molecules (**Fig 3.1b**).

We simulated $N = 5000$ trajectories for each of the 64 input diffusion coefficients to obtain an array of N apparent diffusion coefficients (**Fig. 3.1c**). The empirical cumulative distribution functions (eCDFs) corresponding to the 64 diffusion coefficients were then interpolated using a B-spline (order 25) and normalized individually. The interpolated array of 64 CDFs was then interpolated again along the D dimension using the 'scatteredInterpolant' function in MATLAB. This two-step interpolation provides a continuous 2-dimensional function that can then be used to compute the apparent diffusion coefficient distribution we would observe in our chosen confinement geometry for any true diffusion coefficient value in the range of 0.05 and 20 $\mu m^2/s$. This approach revealed that the experimentally measured apparent diffusion coefficients in *Y. enterocolitica*, are systematically decreased by up to 60% compared to unconfined diffusion (**Fig. 3.1a**). The simulated CDFs account for the effects of molecular confinement due to the cell boundaries, signal integration over the camera exposure time, as well as experimentally calibrated signal-to-noise levels.

3.3.3 Data Fitting

To estimate the number of diffusive states, their diffusion coefficients, and their population fractions, the experimentally measured cumulative distribution functions of apparent diffusion coefficients were fit using linear combinations of simulated *CDF(D*)*. Using the CDF for fitting instead of a PDF histogram eliminates bin-size ambiguities that

can bias the fitting results. To determine the number of diffusive states, a constrained linear least-squares fit (using the 'lsqlin' function in MATLAB) was performed with a periodically sampled array of simulated CDFs. Diffusive states that had diffusion coefficient values within 20% of each other were combined into a single diffusive state by a weighted average based on their population fractions. The resulting vector of fitting parameters, consisting of diffusion coefficients of individual diffusive states and their respective population fractions, was used as a starting point to create arrays of trial fitting parameter vectors with different numbers of diffusive states, ranging from a single diffusive state to a user-defined maximum number of states (five in all cases considered here). Trial parameter vectors were generated as follows: adjacent diffusive states were either combined through weighted averaging or diffusive states were split into two states with equal population fractions and diffusion coefficient 20% above and below the original value. All state combination and splitting possibilities were considered. Each trial vector was used as a starting point for non-linear least-squares fitting of 5 separate subsets of the data (using the 'fmincon' function in MATLAB). In each case, the quality of the fit (quantified as the residual sum of squares) was found by comparing the quality of the fit with respect to the remaining subsets (data cross-validation). The average residual sum of squares was used to quantify the quality of the fit corresponding to a given trial vector. This method yielded multiple trial vectors given the number of diffusive states.

For each number of diffusive states, only the trial vector with the best quality of fit was retained. The optimal number of states was then determined by identifying the last trial vector for which adding an additional state resulted in at least a 5% improvement in the quality of the fit. Finally, this trial vector was then used as the starting point to fit the full

data set using non-linear least squares fitting. To estimate error in each of the fitted parameters, we resampled the dataset 100 times by bootstrapping and then fit them individually, initializing the fit with the same starting parameter vector including a small offset. To constrain the optimization, the population fractions of diffusive states below 0.5 $\mu m^2/s$ were not refined through non-linear least-squares fitting, but instead assigned to stationary molecules. This choice was made because even completely stationary molecules exhibit non-zero apparent diffusion coefficients in single-molecule tracking experiments due to finite single-molecule localization precision (static localization error). In our experiments, the *x*, *y*, and *z* localization precisions were 10-46 nm, 10-49 nm, and 16-71 nm, respectively (154). For simplicity, all data and fits are displayed as PDFs instead of CDFs throughout this manuscript.

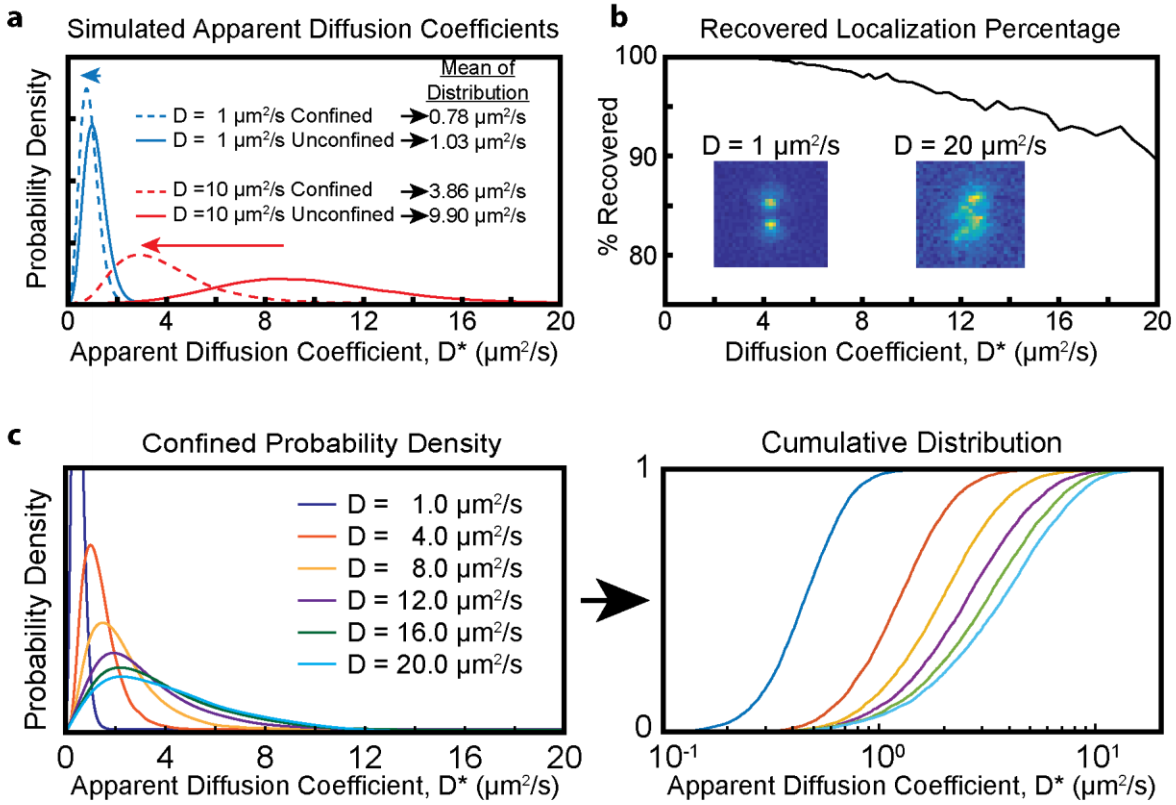

Figure 3.1. Monte-Carlo simulations of expected experimental distribution. (a) Probability density functions showing the effect of spatial confinement. The apparent diffusion coefficients are computed based on the time-integrated (25 ms) center-of-mass coordinates of simulated particles undergoing Brownian diffusion in a cylindrical volume (radius = 0.4 μm, length = 5 μm). The confined distributions are left-shifted (dashed lines) compared to the unconfined distributions. (b) Fraction of successfully localized single-molecules. Time-integrated (25 ms) single-molecule fluorescence signals produce images that resemble PSFs that are blurred to different extents (insets). Faster moving molecules are localized less efficiently due to motion blurring. (c) Expected distributions of apparent diffusion coefficients when confinement and motion blur is taken into account. The

similarity of the distributions increase for faster diffusion coefficients. Figure panels a and c are adapted from Ref. (119).

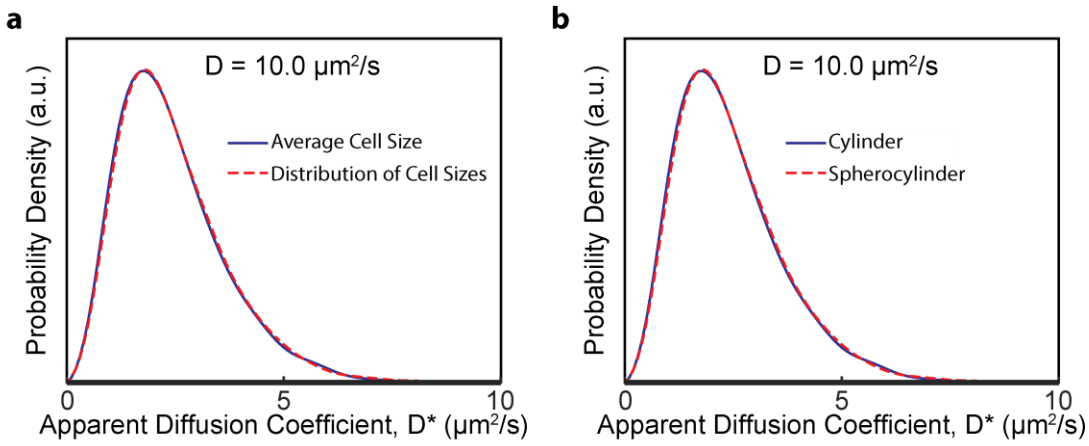

Fig. 3.2. Cell shape and size effect on the apparent diffusion coefficient distribution. (a) We simulated 5000 trajectories each for molecules confined in a single overall average cell size and molecules confined to a normal distribution of cell sizes centered around the average size (length of 4965 ± 880 nm and radius of 470 ± 80 nm). The normal distribution was limited to the range of the minimum and maximum experimental cell sizes (3630-6600 nm for the length and 385-550 nm for the radius). Using a two-sample Komolgorov-Smirnov test with a 5% significance level, these two distributions were not determined to be different. (b) We simulated confined diffusion in the shape of a cylinder and a spherocylinder with equal lengths and radii for a quickly diffusing population (5000 trajectories) with D = 10.0 $\mu m^2/s$. Using a two-sample Komolgorov-Smirnov test with a 5% significance level, these two distributions were not determined to be different.

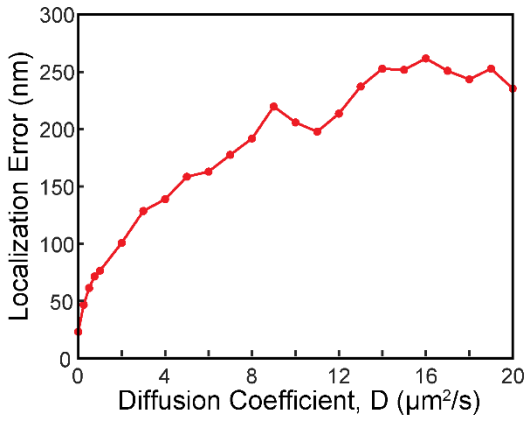

Fig. 3.3. 3D localization error for tracking single-molecule in different diffusive states. Simulations were performed as described in *Materials and Methods*. The localization error is defined as the Euclidian distance between the center-of-mass position of a diffusing molecule in a given camera frame and the fitted position based on the motion-blurred image of the same molecule.

Chapter 4: Single-molecule tracking in live *Yersinia enterocolitica* reveals distinct cytosolic complexes of injectisome subunits

4.1 Abstract

In bacterial type 3 secretion, substrate proteins are actively transported from the bacterial cytoplasm into the host cell cytoplasm by a large membrane-embedded machinery called the injectisome. Injectisomes transport secretion substrates in response to specific environmental signals, but the molecular details by which the cytosolic secretion substrates are selected and transported through the type 3 secretion pathway remain unclear. Secretion activity and substrate selectivity are thought to be controlled by a sorting platform consisting of the proteins SctK, SctQ, SctL, and SctN, which together localize to the cytoplasmic side of membrane-embedded injectisomes. However, recent work revealed that sorting platform proteins additionally exhibit substantial cytosolic populations and that SctQ reversibly binds to and dissociates from the cytoplasmic side of membrane-embedded injectisomes. Based on these observations, we hypothesized that dynamic molecular turnover at the injectisome and cytosolic assembly among sorting platform proteins is a critical regulatory component of type 3 secretion. To determine whether sorting platform complexes exist in the cytosol, we measured the diffusive properties of the two central sorting platform proteins, SctQ and SctL, using live cell high-throughput 3D single-molecule tracking microscopy. Single-molecule trajectories, measured in wild-type and mutant *Yersinia enterocolitica* cells, reveal that both SctQ and SctL exist in several distinct diffusive states in the cytosol, indicating that these proteins form stable homo- and hetero-oligomeric complexes in their native environment. Our findings provide the first diffusive state-resolved insights into the dynamic regulatory network that interfaces stationary

membrane-embedded injectisomes with the soluble cytosolic components of the type 3 secretion system.

4.2 Introduction

Live-cell compatible approaches revealed that the quaternary structure of the cytoplasmic injectisome components is highly dynamic. Fluorescence recovery after photobleaching (FRAP) measurements in *Y. enterocolitica* showed that the sorting platform protein SctQ continuously exchanges between an injectisome bound state and a freely diffusing cytosolic state and that the exchange rate doubled upon chemical activation of protein secretion (48). Other sorting platform proteins, SctK, SctL, and SctN, also exhibit substantial cytosolic populations (49) and fluorescence correlation spectroscopy (FCS) measurements revealed that their diffusion coefficients were altered in different deletion mutants and between secreting and non-secreting conditions (49). These observations suggest that fully-assembled sorting platforms may be natively present in the cytosol as freely diffusing complexes that are functionally relevant for secretion. However, so far, it was not clear whether well-defined cytosolic complexes are responsible for the observed effects.

Here we show formation of distinct homo- and hetero-oligomeric cytosolic complexes of sorting platform proteins using high-throughput 3D single-molecule tracking measurements in live *Y. enterocolitica*. Our results demonstrate that the two central sorting platform proteins, SctQ and SctL, interact with each other and with other T3SS proteins

not just at the injectisome, but also in the cytosol, resulting in the formation of several distinct molecular complexes. We further show that the relative population fractions of these complexes is dependent on the presence of other T3SS proteins and changes with type 3 secretion activity. These results suggest that functional regulation of T3SS may occur away from the membrane-embedded injectisomes through the ordered formation of distinct complexes in the bacterial cytosol.

4.3 Experimental Procedures

4.3.1 Bacterial Strains and Plasmids

Yersinia enterocolitica strains were generated by allelic exchange as previously described (22, 155). Mutator plasmids harboring 250-500 bp flanking regions, the coding sequences of eYFP or PAmCherry1, and a glycine-rich 13 amino acid linker between the fluorescent protein and the target protein were introduced into *E. coli* SM10 λpir for conjugation with *Y. enterocolitica* pIML421asd (35). After sucrose counter-selection for the second allelic exchange event, fluorescent *Y. enterocolitica* were analyzed by PCR to confirm target insertion.

Plasmids for the inducible exogenous expression of fluorescent and fluorescently-tagged proteins were derived from IPTG-inducible pAH12 and arabinose-inducible pBAD vectors. The coding sequences of eYFP and PAmCherry1 were PCR amplified using Q5 DNA polymerase (New England Biolabs, Ipswich, Maine) from pXYFPN-2 and

pVPAmCHY-popZ, respectively (156). The PCR product was isolated using a gel purification kit (Invitrogen, Carlsbad, California) and used as a megaprimer for amplification and introduction into a pAH12-derivative containing a kanamycin resistance cassette, LacI, and a lac promoter to generate pAH12-eYFP and pAH12-PAmCherry1. The pAH12 backbone was a gift from Carrie Wilmot. A series of pBAD expression vectors for eYFP, eYFP-SctQ, eYFP-SctQ$_{M218A}$, PAmCherry1-SctL, and PAmCherry1 were generated from mVenus-pBAD, originally developed by Michael Davidson (Addgene, Cambridge, Massachusetts, plasmid #54845). The coding sequence for eYFP was amplified from pAH12-eYFP. The coding sequence for eYFP-SctQ was amplified from *Y. enterocolitica* strain AD4442 [eYFP-SctQ]. The eYFP-SctQ$_{M218A}$ coding sequence variant was generated using piecewise PCR of AD4442 with both the 5' and 3' fragments containing sequences overlapping the coding region corresponding to the M218A mutation. These fragments were gel purified and combined using outside primers with Q5 DNA polymerase. The coding sequence for PAmCherry1-SctL was amplified from *Y. enterocolitica* strain AD4459. The coding sequence for PAmCherry1 was amplified from pAH12-PAmCherry1. All final PCR products were created with Q5 DNA polymerase and gel purified. Purified products were incubated with Taq DNA polymerase (Thermo Scientific, Waltham, Massachusetts) and dNTPs at 72°C. PCR reactions were TA cloned using pCR2.1-TOPO (Invitrogen) according to the manufacturer's directions. After screening for insert using Taq DNA polymerase, plasmids from positive clones were isolated using a miniprep kit (Omega Biotek, Norcross, Georgia). mVenus-pBAD and pCR2.1 minipreps were digested with EcoRI and XhoI restriction enzymes (New England

Biolabs). Digested vector and inserts were ligated using T4 DNA ligase and transformed into *E. coli* TOP10 cells. Colonies were PCR screened for presence of correct insert. All plasmids were sequenced by GeneWiz (South Plainfield, New Jersey) prior to electroporation into *Y. enterocolitica* for analysis. A list of all strains and plasmids can be found in **Table 4.2**.

4.3.2 Cell Culture

Y. enterocolitica cultures were inoculated from a freezer stock in BHI media (Sigma Aldrich, St. Louis, Missouri) with nalidixic acid (Sigma Aldrich) [35 µg/mL] and 2,6-diaminopimelic acid (Chem Impex International, Wood Dale, Illinois) [8 µg/mL] one day prior to an experiment and grown at 28°C with shaking. After 24 hours, 300 µL of overnight culture was diluted in 5 mL fresh BHI, nalidixic acid, and diaminopimelic acid (dap) and grown at 28°C for another 60-90 minutes. For imaging cells in the secretion ON state, glycerol [4 mg/mL], $MgCl_2$ [20 mM] and EDTA [5 mM] were added to the culture medium. For imaging cells in the secretion OFF state, glycerol, $MgCl_2$, and CaCl2 [5 mM] were added to the culture medium. In both cases, the *yop* regulon was induced by rapidly shifting the cultures to 37°C in a water bath(27), and cells were incubated at 37°C with shaking for another 3 hours prior to imaging. After induction, cells were harvested by centrifugation at 5000 g for 3 minutes and washed 3 times with M2G (4.9 mM Na_2HPO_4, 3.1 mM KH_2PO_4, 7.5 mM NH_4Cl, 0.5 mM $MgSO_4$, 10 µM $FeSO_4$ (EDTA chelate; Sigma), 0.5 mM $CaCl_2$) with 0.2% glucose as the sole carbon source). The remaining pellet was

then re-suspended in M2G, dap, $MgCl_2$, glycerol, and EDTA/$CaCl_2$. Cells were plated on 1.5 – 2% agarose pads in M2G containing dap, glycerol, and $MgCl_2$.

Plasmids were introduced into *Y. enterocolitica* cells using electroporation. Transformed cells were plated on LB agar [10 g/L peptone, 5 g/L yeast extract, 10 g/L NaCl, 1.5% agar] (Fisher Scientific, Hampton, New Hampshire) containing kanamycin [50 µg/mL] or ampicillin [100 µg/mL] for cells containing pAH12- or pBAD-derived plasmids, respectively. For electroporation of *Y. enterocolitica* pIML421asd cells, recovery media and plates also contained dap. Plasmid containing cells were inoculated similarly, except inoculation media also contained kanamycin or ampicillin for pAH12- or pBAD-based plasmids, respectively. Prior to imaging cell cultures were rapidly temperature shifted to 37°C and incubated for 3 hours. Cultures of cells containing pAH12- or pBAD-based plasmids were induced with IPTG (Sigma Aldrich) [0.2 mM, final] or arabinose (Chem Impex) [0.2%], respectively, for the final 2 hours of incubation.

4.3.3 Secretion Assay and Immunoblot

Cultures for protein secretion assays and immunoblot analysis were inoculated to an optical density at 600 nm (OD600) of 0.15 in BHI supplemented with 35 µg/ml nalidixic acid, 80 µg/ml diaminopimelic acid, 0.4% glycerol, 20 mM $MgCl_2$, and 5 mM EDTA. Cultures were agitated at 28°C for 90 min. The *yop* regulon was then induced by shifting the temperature to 37°C in a water bath, where cultures were agitated for another 180 min. Supernatant and whole cells were separated by centrifugation (5 min, 21,000 g). Secreted

proteins were precipitated with 10% trichloroacetic acid overnight at 4°C. An equivalent of proteins secreted by $3 \cdot 10^8$ bacteria was used for further analysis of the supernatant, whereas the lysate of the equivalent of 10^8 bacteria was loaded onto the gel for analysis of total cellular proteins. Proteins were separated on Novex 4–20% gradient SDS–PAGE gels and stained using the Coomassie-based 'Instant blue' staining solution (Expedeon, San Diego, California), or immunoblotted using rabbit polyclonal antibodies against *Y. enterocolitica* SctQ (MIPA235; 1:1,000) (**Fig. 4.6**).

4.3.4 Super-resolution Fluorescence Imaging

Experiments were performed on a custom-built dual-color inverted fluorescence microscope based on the RM21 platform (Mad City Labs, Inc, Madison, Wisconsin). Immersion oil was placed between the objective lens (UPLSAPO 60X 1.4 NA) and the glass cover slip (VWR, Radnor, Pennsylvania, #1.5, 22mmx22mm). Single-molecule images were obtained by utilizing eYFP photoblinking (86) and PAmCherry1 photo-activation (157). A 514 nm laser (Coherent, Santa Clara, California, Genesis MX514 MTM) was used for excitation of eYFP (~350 W/cm^2) and 561nm laser (Coherent Genesis MX561 MTM) was used for excitation of PAmCherry1 (~350 W/cm^2). A 405 nm laser (Coherent OBIS 405nm LX) was used to photo-activate PAmCherry1 (~20 W/cm^2) simultaneously with 561nm excitation. Under these imaging conditions, more than 50 % of the imaged cells underwent cell division on the coverslip (**Fig. 4.14**). Zero order quarter wave plates (Thorlabs, Newton, New Jersey, WPQ05M-405, WPQ05M-514, WPQ05M-

561) were used to circularly polarize all excitation lasers, and the spectral profile of the 514nm laser was filtered using a band-pass filter (Chroma, Bellows Falls, Vermont, ET510/10bp). Fluorescence emission from both eYFP and PAmCherry1 was passed through a shared filter set (Semrock, Rochester, New York, LP02-514RU-25, Semrock NF03-561E-25, and Chroma ET700SP-2P8). A dichroic beam splitter (Chroma T560lpxr-uf3) was then used to split the emission pathway into 'red' and 'green' channels. An additional 561nm notch filter (Chroma ZET561NF) was inserted into the 'red' channel to block scattered laser light. Each emission path contains a wavelength specific dielectric phase mask (Double Helix, LLC, Boulder, Colorado) that is placed in the Fourier plane of the microscope to generate a double-helix point-spread-function (DHPSF) (99, 136). The fluorescence signals in both channels are detected on two separate sCMOS cameras (Hamamatsu, Bridgewater, New Jersey, ORCA-Flash 4.0 V2). Up to 20,000 frames are collected per field-of-view with an exposure time of 25ms. A flip-mirror in the emission pathway enables toggling the microscope between fluorescence imaging and phase contrast imaging modes without having to change the objective lens of the microscope.

4.3.5 Data Analysis

Raw image processing and analysis was carried out as described in section 3.1. Single molecule localizations were assigned to individual cells as described in section 3.2.1. Analysis of high density regions of localizations was carried out using the density based clustering algorithm DBSCAN (158), using a distance parameter of 75 nm and a

minimum number of points parameter of 15. Single-Molecule Tracking was performed as described in section 3.3.1. To resolve the unconfined diffusion coefficients of predominant molecular complexes in living cells based on the experimentally measured distribution of apparent diffusion coefficients, we performed Monte Carlo simulations of confined Brownian motion as described in section 3.3.2. Experimental distributions of apparent diffusion coefficients were fit using a linear combination of simulated distributions as described in section 3.3.3. Confidence intervals for all fitting parameters were obtained by bootstrapping and are reported in **Table 4.3**. The radial distributions in **Fig. 4.11 and 4.12** were created as described in section 3.2.2.

4.4 Results and Discussion

4.4.1 Stationary SctQ localizes near the cell membrane

We introduced the coding sequence of eYFP in-frame near the translation start site of the SctQ coding sequence on the pYV virulence plasmid, which encodes all T3SS proteins in *Y. enterocolitica*, using previously described allelic replacement techniques (22, 155). In this way, the eYFP-SctQ fusion protein is expressed under the control of its native promoter. The cellular levels of eYFP-SctQ were increased compared to the native, unlabeled protein; we confirmed that the resulting fusion proteins did not result in detectable degradation products and were fully functional in an effector protein secretion assay (**Fig. 4.6**). We then used 3D-single molecule localization microscopy (3D-SMLM) to determine the subcellular positions of eYFP-SctQ molecules in live *Y. enterocolitica*

under secreting conditions. The observed single-molecule localizations revealed clustering near the cell surface, and, when rendered as an intensity image, these clusters gave rise to the bright fluorescent foci (**Fig. 4.1a,b**), which are similar to those observed by diffraction-limited and super-resolution microscopy (22, 23, 48). We used DBSCAN (158), a density-based clustering algorithm, to determine the positions and sizes of each cluster and found that clusters are preferentially localized within a 400-450 nm radius from the central cell axis (**Fig. 4.1c,d**). This subcellular preference is consistent with membrane association, given the 469 ± 91 nm (mean ± s.d.) radius of *Y. enterocolitica* cells used in our experiments, and clusters have been previously observed to co-localize with other membrane-embedded injectisome components in two-color fluorescence imaging experiments (22, 23, 48). In contrast, cluster formation was not observed when we exogenously expressed eYFP-SctQ in a *Y. enterocolitica* strain lacking the pYV plasmid (pYV^-) (**Fig. 4.1e**). Instead, eYFP-SctQ was uniformly distributed throughout the bacterial cytosol.

Instead of only considering the localized molecules within clustered regions, as done by Zhang *et al.* (23), we additionally quantified the diffusive properties of all localized molecules. Single-molecule tracking measurements in wild-type cells showed that the eYFP-SctQ population partitioned into a stationary and a mobile fraction (**Fig. 4.1f**). As expected, trajectories with slow apparent diffusion coefficients ($D^* < 0.15$ μm^2/s) spatially co-localize with clusters (**Fig. 4.1g and Fig. 4.12a**), while the faster diffusing molecules ($D^* > 0.15$ μm^2/s) localize randomly throughout the cell volume (**Fig. 4.1f inset, Fig. 4.12a)**. The $D^* = 0.15$ μm^2/s threshold was chosen based on the non-zero

diffusion coefficients obtained for stationary emitters that are repeatedly localized with limited spatial localization precision (**Fig. 4.10**). We conclude that stationary membrane-embedded injectisomes serve as binding sites for SctQ molecules, and we assign the observed clusters or foci to injectisome-bound eYFP-SctQ molecules.

4.4.2 SctQ exists in at least 3 diffusive states in the bacterial cytosol

The majority (~86%) of eYFP-SctQ localizations are not cluster-associated, but instead diffuse randomly throughout the cytoplasm (**Fig. 4.1a,b,d**). To examine the diffusive behaviors of unbound eYFP-SctQ, we determined the 3D trajectories of ~100,000 individual eYFP-SctQ molecules in hundreds of cells and computed the apparent diffusion coefficients for each trajectory (**4.3 Experimental Procedures**). As mentioned in the previous section, the resulting distribution of apparent diffusion coefficients shows two prominent peaks: one near ~0 $\mu m^2/s$ and the other at ~0.5 $\mu m^2/s$ (**Fig. 4.1f**). In addition to the peak at ~0.5 $\mu m^2/s$, the distribution also shows a slow decay towards higher apparent diffusion coefficients. Using Monte Carlo simulations of anisotropically confined Brownian diffusion within rod-shaped bacterial cell volumes, we determined that such a distribution shape is only possible when multiple diffusive states manifest in the cell (**4.3 Experimental Procedures, Fig. 4.7**).

To estimate the unconfined diffusion coefficients (*D*) and population fractions of the diffusive states that are present in the cell, we used linear combinations of the Monte Carlo simulated apparent diffusion coefficient distributions to fit the experimentally

measured distributions (**4.3 Experimental Procedures**). We found that fitting the eYFP-SctQ data required three cytosolic diffusive states corresponding to unconfined diffusion coefficients D = 1.1, 4.0, and 13.9 μm^2/s with population fractions of 17%, 36%, and 22%, respectively (**Fig. 4.2a,b, Table 4.1**). These components are in addition to a stationary component (D < 0.5 μm^2/s) with population fraction of 24%. Confidence intervals for the optimized fitting parameters were obtained by bootstrapping and are reported in **Table 4.3**.

As we did not detect any eYFP cleavage products (**Fig. 4.6**), the eYFP-SctQ monomer is the smallest and likely the fastest diffusing molecular species in our cells. Control experiments to measure the unconfined diffusion coefficients of eYFP confirmed that, when expressed in wild-type *Y. enterocolitica*, eYFP diffused at a similarly fast rate of D = 11.3 μm^2/s (**Fig. 4.9i, Table 4.1**). We also observe a small stationary component for this protein suggesting that, even in the absence of known binding partners, the presence of immobile proteins cannot be ruled out in living cells. Assigning the fastest diffusive eYFP-SctQ state (D = 13.9 μm^2/s) to the monomeric eYFP-SctQ fusion protein implies that the slower diffusive states at D ~ 1 and 4 μm^2/s correspond to two distinct high molecular weight complexes, which could be eYFP-SctQ homo- or hetero-oligomers that involve additional T3SS proteins. To determine the molecular composition of these high molecular weight complexes, we performed further single-molecule tracking measurements in different genetic backgrounds.

4.4.3 SctQ is capable of forming higher-order oligomers in the absence of other T3SS proteins

To test whether SctQ can form high molecular weight complexes in living cells independent of other T3SS proteins, we tracked single eYFP-SctQ molecules in a strain lacking all T3SS components (the pYV$^-$ strain), for which membrane association was not observed (**Fig. 4.1e**). Fitting the distribution of apparent diffusion coefficients of eYFP-SctQ in the pYV$^-$ strain required four diffusive states (**Fig. 4.3a, Table 4.1**). The predominant diffusive state (D = 3.6 μm^2/s, 78%) is similar to the D = 4.0 μm^2/s state observed for eYFP-SctQ in wild-type cells. These data show that formation of a specific oligomeric SctQ species is favored in pYV$^-$ cells and does not require any other T3SS proteins. Conversely, the oligomerization behavior of eYFP-SctQ changes when other T3SS proteins are present, as there is a higher relative abundance of the putative eYFP-SctQ monomer in wild-type cells (22%) compared to pYV$^-$ cells (~5%). If oligomerization of SctQ was completely unregulated we would expect a higher fraction of the D ~ 4 μm^2/s diffusive state in wild-type cells, especially since the eYFP-SctQ fusion is express at slightly higher levels compared to the native, unlabeled protein (**Fig. 4.6**).

4.4.5 Formation of the oligomeric SctQ complex is dependent on expression of SctQ$_C$

Previous work in *Yersinia* has shown that elimination of the internal translation initiation site through a mutation in the *sctQ* coding sequence that replaces the methionine residue at position 218 with an alanine (M218A) results in a secretion-deficient phenotype

and that wild-type secretion levels can be restored upon expression of $SctQ_C$ *in trans* (48, 54). We therefore hypothesized that the $D \sim 4$ μm^2/s diffusive state measured for eYFP-SctQ in wild-type cells and pYV$^-$ background is due to a molecular complex containing SctQ and its C-terminal fragment $SctQ_C$ (53-55). To test this hypothesis, we utilized the *eyfp-sctQ*$_{M218A}$ coding sequence to express full length eYFP-SctQ, but not $SctQ_C$, in the *Y. enterocolitica* pYV$^-$ strain (48).

In the absence of $SctQ_C$, the distribution of apparent diffusion coefficients of eYFP-$SctQ_{M218A}$ was best fit with four diffusive states (**Fig. 4.3b, Table 4.1**). The previously observed diffusive state ($D \sim 4$ μm^2/s) of eYFP-SctQ is absent upon elimination of $SctQ_C$ expression. We instead observe a different, faster moving diffusive state ($D = 6.8$ μm^2/s), which is not observed for eYFP-SctQ in either wild-type or pYV$^-$ genetic backgrounds. We therefore assign the $D = 6.8$ μm^2/s diffusive state to a homo-oligomeric SctQ species. Indeed, an oligomeric SctQ-only species was previously detected by co-immunoprecipitation in the absence of $SctQ_C$ (53). We conclude that the presence of $SctQ_C$ enables the formation of a well-defined oligomeric SctQ:$SctQ_C$ complex, which diffuses at $D \sim 4$ μm^2/s and forms spontaneously in *Y. enterocolitica* in the absence of other T3SS proteins.

The existence of an oligomeric SctQ:$SctQ_C$ complex is supported by several reports in the recent literature. Bzymek *et al.* expressed *Y. pseudotuberculosis* SctQ and $SctQ_C$ in *E. coli* and co-purified a SctQ:$SctQ_C$ complex with 1:2 stoichiometry ($MW = 52.8$ kDa) (54). McDowell *et al.* found that *S. flexneri* SctQ:$SctQ_C$ was further able to form higher order oligomers consisting of up to six copies of the minimal 1:2 complex and that

formation of such higher order oligomers was essential for secretion (55). The quaternary structure of *in situ* injectisomes, recently provided by cryo-electron tomography of *Shigella flexneri* and *Salmonella enterica* minicells (37-39), allows us to further speculate on the stoichiometry of the oligomeric SctQ:$SctQ_C$ complex. The sub-tomogram averaged injectisomes displayed six cytoplasmic "pods" that, on one side, attach to the membrane-embedded ring of the needle complex and, on the other side, to hexameric SctN. The observed protein densities of the pods are large enough to contain a tetramer of SctQ proteins, such that 24 SctQ molecules (six tetramers) can be bound to the injectisome at any one time. This value agrees with previously estimated numbers of fluorescently-labelled SctQ proteins within a single diffraction-limited fluorescent focus/cluster (N = 22 ± 8, 28 ± 7, ~24 ± 5) (23, 48, 49). Based on the available data to date, we speculate that the $D \sim 4\ \mu m^2/s$ diffusive state observed in wild-type *Y. enterocolitica* cells is the oligomeric SctQ:$SctQ_C$ complex that consists of four SctQ and eight $SctQ_C$ subunits.

4.4.6 SctQ and SctL co-diffuse as a complex in the cytoplasm

Our single-molecule tracking measurements of eYFP-SctQ in wild-type *Y. enterocolitica* reveal the presence of a slowly diffusing $D \sim 1\ \mu m^2/s$ species with a population fraction of 17%. The increased abundance of this diffusive state compared to pYV^- cells could indicate the regulated formation of a slowly diffusing high-molecular weight complex. Indeed, high molecular weight complexes with estimated molecular weights ~1 MDa containing SctQ, SctL, SctK, and SctN have been previously identified

in pull-downs and size-exclusion chromatography (41, 47). Given the established interactions between SctK-Q-L-N (43-46), we hypothesized that the $D \sim 1$ μm^2/s diffusive state consists, at least partially, of a complex containing not just SctQ:SctQ$_C$, but also SctK, SctL, and possibly SctN (see **Fig. 1.1**).

To test whether the $D \sim 1$ μm^2/s or $D \sim 4$ μm^2/s diffusive states of eYFP-SctQ are complexes that contain SctL, we used allelic-replacement of the native SctL coding sequence on the pYV virulence plasmid to express the PAmCherry1-SctL fusion protein in wild-type *Y. enterocolitica*. Fitting the apparent diffusion coefficient distribution of PAmCherry1-SctL revealed a substantial stationary population ($D < 0.50$ μm^2/s) with a population fraction of 56%. Stationary PAmCherry1-SctL trajectories localized preferentially near the cell boundary (**Fig. 4.12f**). Based on the same arguments made for eYFP-SctQ, we assign the stationary PAmCherry1-SctL trajectories to injectisome-bound molecules. Fitting the non-stationary components of the apparent diffusion coefficient distribution revealed the presence of five diffusive states (**Fig. 4.4a, Table 4.1**). The only observed diffusive states in common between eYFP-SctQ and PAmCherry1-SctL in wild-type *Y. enterocolitica* is the $D \sim 1$ μm^2/s state. The presence of this common state raises the possibility that these two proteins co-diffuse as a high-molecular weight complex in the cytosol of living cells.

To test whether the $D \sim 1$ μm^2/s diffusive state of PAmCherry1-SctL is dependent on the presence of SctQ and other T3SS proteins, we expressed PAmCherry1-SctL in the pYV$^-$ strain. In this genetic background, the apparent diffusion coefficient distribution is fit by four diffusive states (**Fig. 4.4b, Table 4.1**). A majority of the stationary component

is lost in the absence of other T3SS proteins and the population fractions are redistributed to other cytosolic states. Notably absent is a diffusive state near 1 $\mu m^2/s$, indicating that the presence of other T3SS proteins is required for the formation of this state.

As an additional control, we analyzed the diffusive states of eYFP-SctQ in a *ΔsctL* background (**Figure 4.4c**). The obtained diffusive states, closely resemble those found in the pYV- background, namely, a predominant population in a $D \sim 4\ \mu m^2/s$ diffusive state (60%), in addition to two smaller populations, one in a $D \sim 12\ \mu m^2/s$ diffusive state (15%), and one in a $D \sim 1\ \mu m^2/s$ diffusive state (13%). We assign the fast diffusive state to monomeric eYFP-SctQ, as before. The molecular species responsible for the limited amounts of the $D \sim 1\ \mu m^2/s$ diffusive state remains unclear, but the presence of this state is consistent with the results obtained for eYFP-SctQ and eYFP-$SctQ_{M218A}$ in the pYV- backgrounds. The higher population fraction of eYFP-SctQ in wild type cells could thus be due to two different high molecular weight complexes that diffuse at the same rates. The slightly increased population fraction of the stationary component compared to those in the pYV- background could indicate limited binding of eYFP-SctQ to membrane-embedded injectisome precursors, which are known to assemble in absence of SctL(38).

The existence of a high molecular weight complex containing SctQ, $SctQ_C$, SctK, SctL, and SctN is consistent with previous FCS measurements showing that the population-averaged diffusion rate of eGFP-SctQ and eGFP-SctL increased when SctN was deleted (49). It is therefore possible that the $D \sim 1\ \mu m^2/s$ diffusive state observed in our work is due to the cytosolic presence of a large supramolecular complex that contains six SctK-Q-L pods, which are each connected to a central hexameric ATPase. Such a supramolecular

complex would have a molecular weight of ~2 MDa, assuming previously estimated stoichiometries (23, 38, 39, 48, 49), and could form either through the stepwise assembly in the cytoplasm or upon concerted dissociation from membrane-embedded injectisomes. An alternative explanation is that the $D \sim 1$ μm^2/s diffusive state represents a single pod that is connected to SctL and possibly SctK and SctN. Even though the Stokes-Einstein relation is not expected to hold in the crowded cytoplasm of living bacterial cells (159, 160), it is not clear how the rather modest addition of SctL (2x25 kDa), SctK (24 kDa), and SctN (48 kDa) subunits to an existing $SctQ_4$:$SctQ_{C8}$ complex (330 or 220 kDa with and without the eYFP tag, respectively) could change its diffusion coefficient by a factor of four. Future work to determine the complete molecular composition of the species responsible for the $D \sim 1$ μm^2/s diffusive state will help address this question.

4.4.7 Induction of T3SS secretion alters diffusion behaviors of select cytosolic species

FRAP measurements established that, under secreting conditions, injectisome-bound eGFP-SctQ was dynamically replaced by new cytosolic proteins within $t_{½} \sim 70$ seconds ($t_{½} \sim 135$ seconds in non-secreting *Y. enterocolitica* cells) (48). Additionally, FCS measurements found that the population-averaged diffusion rates of SctK, SctQ, and SctL correlate with the secretion state (49). Our results show that the T3SS proteins SctQ and SctL form high molecular weight complexes in the cytosol and that formation of these states is dependent on the presence of other T3SS proteins. Together, these findings suggest the possibility that the type 3 protein secretion pathway is, at least

in part, regulated from within the cytosol. We therefore asked whether the diffusion rates or population fractions of SctQ and SctL diffusive states correlate with the secretion state of the cells.

To compare the diffusion behaviors of eYFP-SctQ and PAmCherry1-SctL in secretion ON vs. OFF states we used the fact that the *Y. enterocolitica* T3SS can be switched between secretion ON and OFF states by the addition of EDTA or $CaCl_2$, respectively (27). We observed that stimulation of secretion increased the mean apparent diffusion coefficient for mobile molecules ($D^* > 0.15$ μm^2/s) from 1.43 μm^2/s to 1.69 μm^2/s for eYFP-SctQ and from 0.86 μm^2/s to 1.10 μm^2/s for PAmCherry1-SctL, which is consistent with recent FCS and earlier 2D-PALM measurements (48, 49). (**Table 4.4)**.

The apparent diffusion coefficient distribution of eYFP-SctQ in secretion OFF conditions was fit with three diffusive states (**Fig. 4.5a, Table 4.1**), while that of PAmCherry1-SctL was fit with four diffusive states (**Fig. 4.5b, Table 4.1**). The diffusion coefficients obtained for eYFP-SctQ are similar between secretion ON and OFF conditions, suggesting that the oligomerization states of SctQ are not altered upon induction of secretion. However, the relative population fractions do change, suggesting that the relative abundances of SctQ containing complexes are regulated. For PAmCherry1-SctL on the other hand, there seems to be a more complex rearrangement among diffusive states of low abundance. Nonetheless, the presence of the D ~ 1 μm^2/s diffusive state for both eYFP-SctQ and PAmCherry1-SctL under secretion ON and secretion OFF conditions indicates that the cytosolic interaction between SctQ and SctL is

robustly present in both secreting and non-secreting cells. Furthermore, we observe a similar decrease in the relative population fractions of the $D \sim 1\ \mu m^2/s$ diffusive states upon induction of secretion, namely a 26% decrease for eYFP-SctQ and a 24% decrease for PAmCherry1-SctL. These results support our conclusion that SctQ and SctL co-diffuse as high molecular weight complex in the cytosol and suggest that the strength of the SctQ and SctL interaction is not subject to functional regulation of the T3SS ON/OFF switch.

4.5 Conclusions

While it's currently unknown how the cytosolic sorting platform proteins exert their role in the function of the T3SS, it has become clear that their ability to form dynamic cytosolic complexes is linked to function. However, these complexes have remained poorly defined. Using high-throughput 3D single-molecule tracking in living bacterial cells, we resolved the diffusive states of eYFP-SctQ and PAmCherry1-SctL and quantified their respective population fractions. This allowed us to analyze the cytosolic complex formation of the two central sorting platform proteins SctQ and SctL. Our data are consistent with a model in which cytosolic SctQ undergoes dynamic assembly and disassembly steps to interconvert between at least three distinct molecular species that diffuse at different rates. SctQ monomers diffuse freely in the cytosol ($D \sim 14\ \mu m^2/s$) or self-assemble into oligomeric SctQ:$SctQ_C$ complexes ($D \sim 4\ \mu m^2/s$) with the help of the C-terminal fragment $SctQ_C$. The self-assembly process does not require the presence of other T3SS proteins as evidenced by the observation that a $D \sim 4\ \mu m^2/s$ diffusive state is present

in both wild-type and pYV$^-$ backgrounds. The SctQ:SctQ$_C$ complexes do not yet contain SctL, because SctL molecules tracked in wild-type cells do not exhibit a $D \sim 4$ μm^2/s diffusive state. However, it remains a possibility that SctQ:SctQ$_C$ complexes in wild-type cells contain SctK, which has been shown to interact with SctQ (43-46). Ultimately, the SctQ:SctQ$_C$ complexes further associate with SctL, SctK, and possibly SctN to form hetero-oligomeric high molecular weight complexes that diffuses at a rate of $D \sim 1$ μm^2/s. The presence of a $D \sim 1$ μm^2/s diffusive state in both the eYFP-SctQ and PAmCherry1-SctL data suggest that SctQ and SctL co-diffuse as part of high molecular weight complexes, but it remains to be determined whether these complexes are individual sorting platform pods or large supramolecular complexes containing six pods that are each connected to a central hexameric ATPase.

At this stage, it is still unclear which of the defined complexes detected in this manuscript plays which role in the secretion process. However, our work reveals two distinct fundamental changes in the architecture of the cytosolic complexes upon activation of the T3SS: either the relative abundances of diffusive states (for SctQ) or the diffusive states themselves (for SctL) are altered upon induction of secretion suggesting a delocalized mechanism of T3SS functional regulation. The diffusive-state-resolved insights add to a growing body of evidence that points to the existence of a dynamic network of cytosolic interactions among structural injectisome proteins and complexes thereof. The activity and substrate selectivity of T3SSs may thus not be programmed into the quaternary structure of the injectisome itself, but instead established in the cytosol through dynamic interactions between T3SS components. Given the *in situ* morphology of

injectisomes, it is tempting to speculate that molecular turnover at the injectisome is the result of dynamic binding and unbinding events of individual sorting platform pods and/or entire injectisome cytoplasmic complexes. Such dynamics may help regulate the secretion activity of the T3SS or enable the shuttling of secretion substrate:chaperone complexes to the injectisome. Similar mechanisms might be at play to regulate the structurally similar flagellar motor complex. Chaperone:substrate:$FliH_2$-FliI complexes (SctL and SctN homologues) have been isolated from cell extracts (161, 162), and FliI, possibly as part of such a complex, exchanges between the cytosol and the flagellar basal body (163). The bound FliI interacts with the switch complex, which is responsible for controlling the direction of the flagellar rotation, through an interaction between FliH and FliN (SctQ homologue) (164, 165). Regulated assembly of cytosolic protein may thus be a widespread mechanism through which the T3SS and similar bacterial secretion systems are functionally regulated. The present work provides a general strategy to resolve and quantify cytosolic complex formation in living bacterial cells.

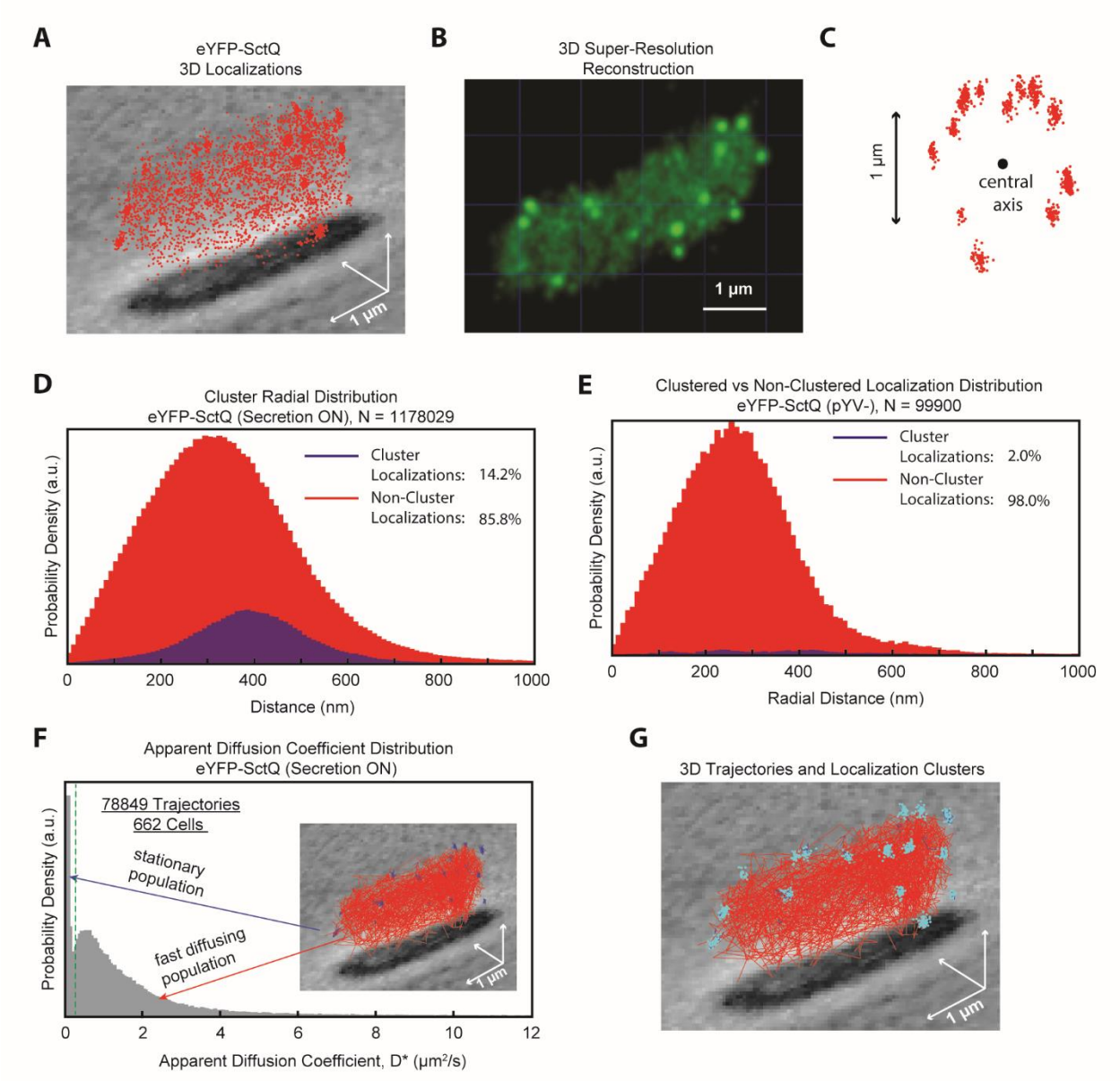

Fig. 4.1. Fluorescently labelled eYFP-SctQ localizes throughout the cytosol and forms distinct clustered foci near the membrane. (a) Scatter plot of 3D localizations of eYFP-SctQ in a representative wild-type *Y. enterocolitica* cell overlaid on a phase contrast image of the cell. (b) Super-resolution image of the data shown in (a). Each single-molecule localization was rendered as a Gaussian sphere of width σ equal to the average localization

precision. Closely overlapping spheres generate high intensity in the reconstructed image. An example cell for each data set can be found in **Fig. 4.13**. (c) Clustered localizations of eYFP-SctQ in a single cell, viewed along the central axis of the cell. (d) Radial distribution of clusters as determined by the DBSCAN clustering algorithm (158). Clustered localizations are enriched near the cell membrane. The distributions are broadened by cell width heterogeneity in the bacterial population and uncertainty in defining the central axis of the cells (e) 3D radial distribution of clusters for eYFP-SctQ in the pYV^- strain. Fewer clusters are present and do not preferentially localize near the cell membrane. (f) Probability density function of apparent diffusion coefficients for eYFP-SctQ. Two visually distinguishable populations emerge: a stationary ($D^* < 0.15$ $\mu m^2/s$) and a mobile population ($D^* > 0.15$ $\mu m^2/s$). (f inset) Stationary (blue) and diffusive (red) trajectories in a single *Yersinia* cell. (g) Clustered localizations (teal) overlaid on the trajectory plot. Across the population (N = 662 cells) 60% of all stationary trajectories co-localized with clustered regions (within 100 nm of the cluster center-of-mass). The remaining 40% do not co-localize with clusters, because clustering algorithms rely user-defined parameters and are not 100% efficient in identifying clusters, especially in the presence of numerous diffuse localization, as is the case here.

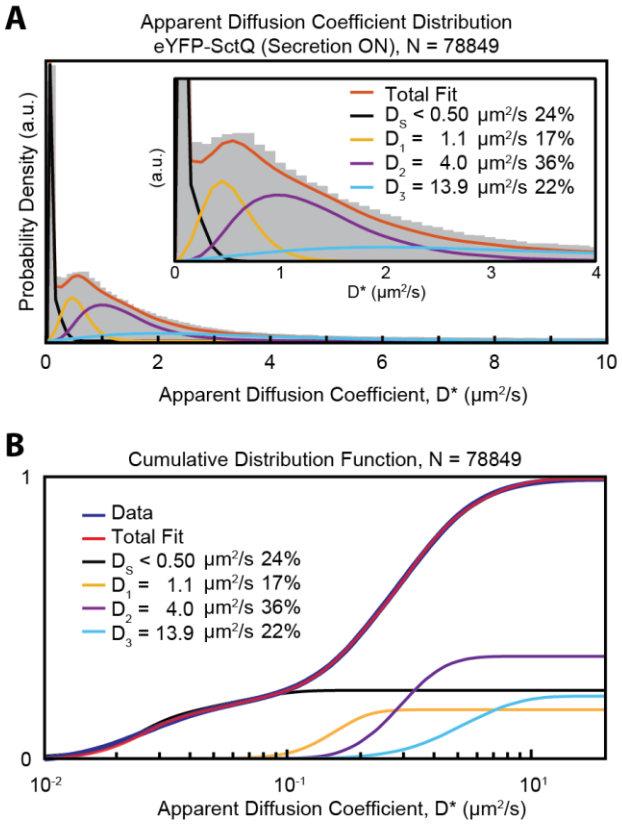

Fig. 4.2. Fit of the distribution of apparent diffusion coefficients for eYFP-SctQ. (a) Fitting the distribution of eYFP-SctQ apparent diffusion coefficients required at least three diffusive states ($D_{1\text{-}3}$) in addition to a stationary population (D_S). (b) The cumulative distribution function (CDF) of eYFP-SctQ apparent diffusion coefficients is fit using the indicated CDFs obtained by Monte-Carlo simulation of confined Brownian motion characterized by the indicated diffusion coefficients.

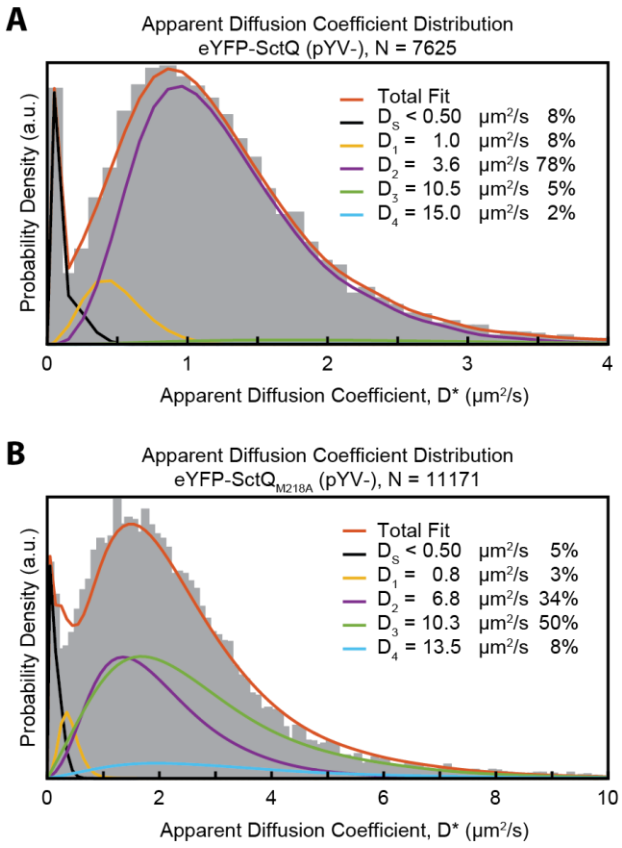

Fig. 4.3. Fit of the apparent diffusion coefficient distributions for eYFP-SctQ in the absence of other T3SS proteins. (A) Fitting of the eYFP-SctQ apparent diffusion coefficients distribution in the pYV$^-$ strain shows a dominant population at ~3.6 μm^2/s. (B) A mutation in the SctQ coding sequence that suppresses the expression of SctQ$_c$ eliminates the 3.6 μm^2/s state and favors a faster diffusing state at 6.8 μm^2/s.

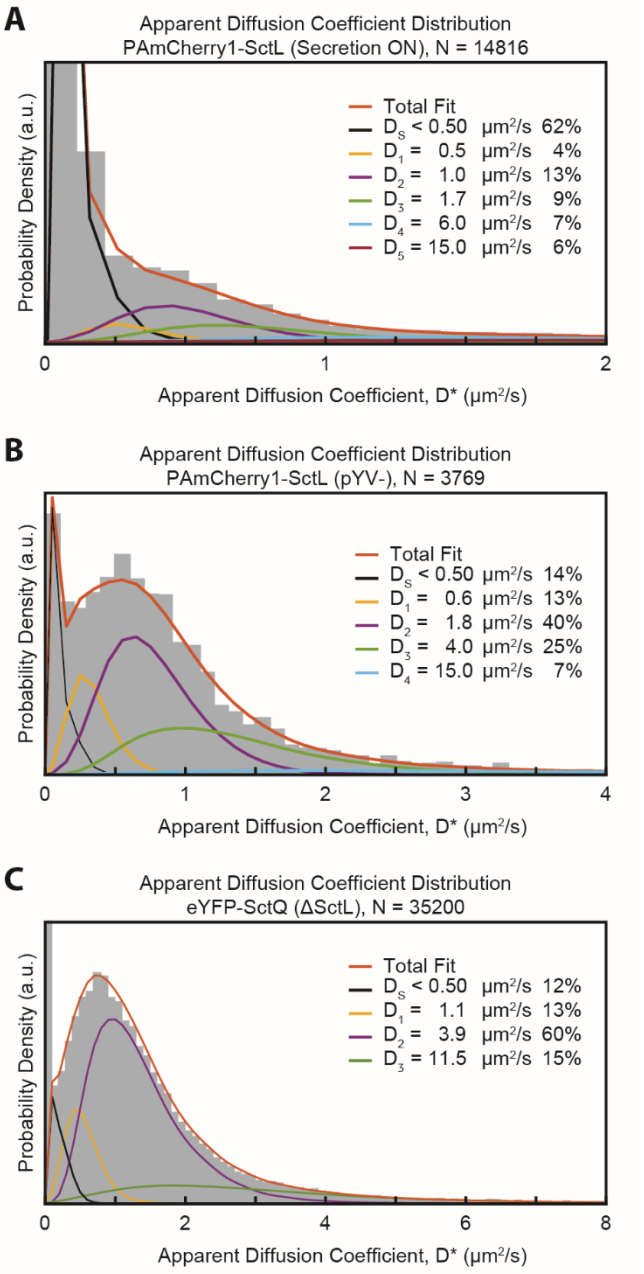

Fig. 4.4. Comparison of PAmCherry1-SctL in the wild-type vs the pYV$^-$ strain. (a) Fitting of the apparent diffusion coefficient distribution for PAmCherry1-SctL shows the majority of the population in a stationary state. (b) In the absence of other T3SS proteins the

stationary state is depleted, and PAmCherry1-SctL favors faster diffusive states. (c) Apparent diffusion coefficient fitting of eYFP-SctL in a ΔSctL background. Note that the peak near D*=0 is not fit well in this case due to large bin-sizes used in the histogram. We therefore assess the quality of fit using the cumulative distribution function shown in **Fig. 4.8e**.

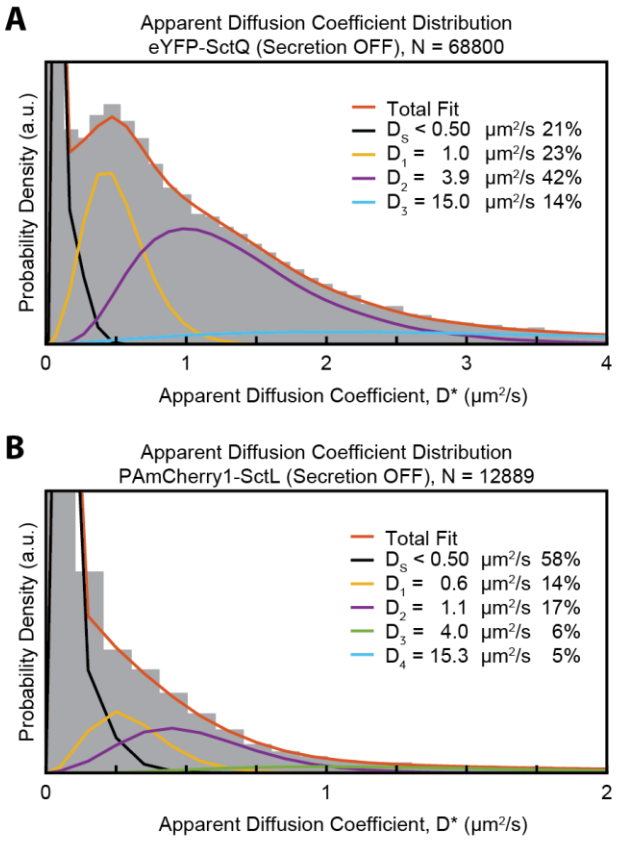

Fig. 4.5. Apparent diffusion coefficient distribution fits for eYFP-SctQ and PAmCherry1-SctL under secretion OFF conditions. (a) Fitting of secretion OFF conditions for eYFP-SctQ. While the individual diffusion coefficients remain the same as for secretion ON conditions, there is an overall population shift towards slower diffusing states. (b) Fitting of secretion OFF conditions for PAmCherry1-SctL. As is the case for eYFP-SctQ, there is a shift towards slower diffusing states for secretion OFF conditions.

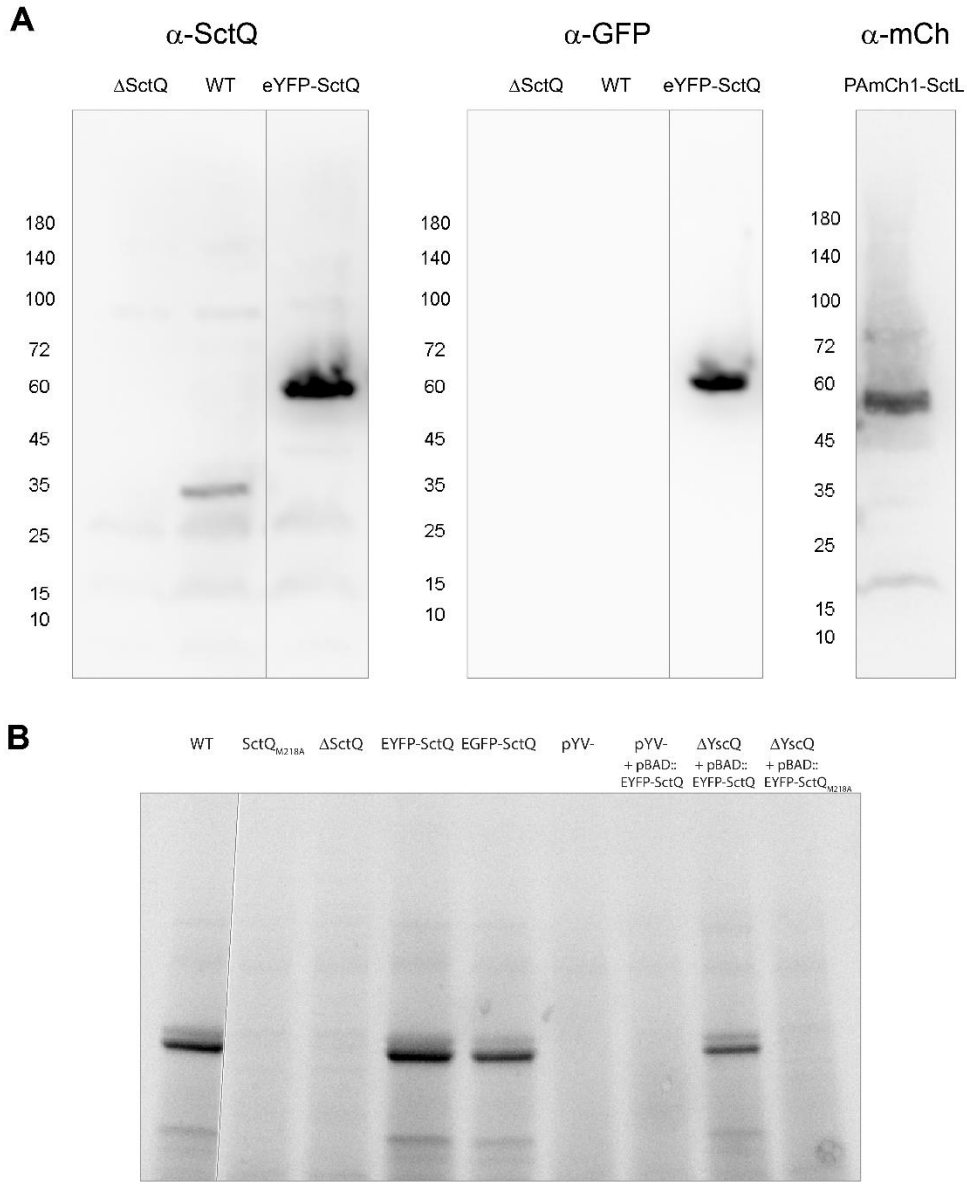

Fig. 4.6. The fusion proteins used in this study are stable and functional. (a) Immunoblot of total cellular proteins of *Y. enterocolitica* dHOPEMTasd strains expressing the denoted fusion proteins (as well as WT and *ΔsctQ* controls) probed against *Y. enterocolitica* SctQ (left), GFP (center), or mCherry (right) show expression of the full length fusion proteins (expected sizes of WT SctQ, 34.4 kDa; eYFP-SctQ, 62.8 kDa; PAmCherry1-SctL,

53.7 kDa) at higher expression levels compared to wild type, but with no detectable cleavage products. (b) Secretion profile of the indicated strains under secreting conditions. Cells were incubated at 37°C for three hours and the cell culture supernatant was TCA-precipitated. All samples were run and analyzed on the same gel after Coomassie staining; vertical lines indicate omission of intermediate lanes.

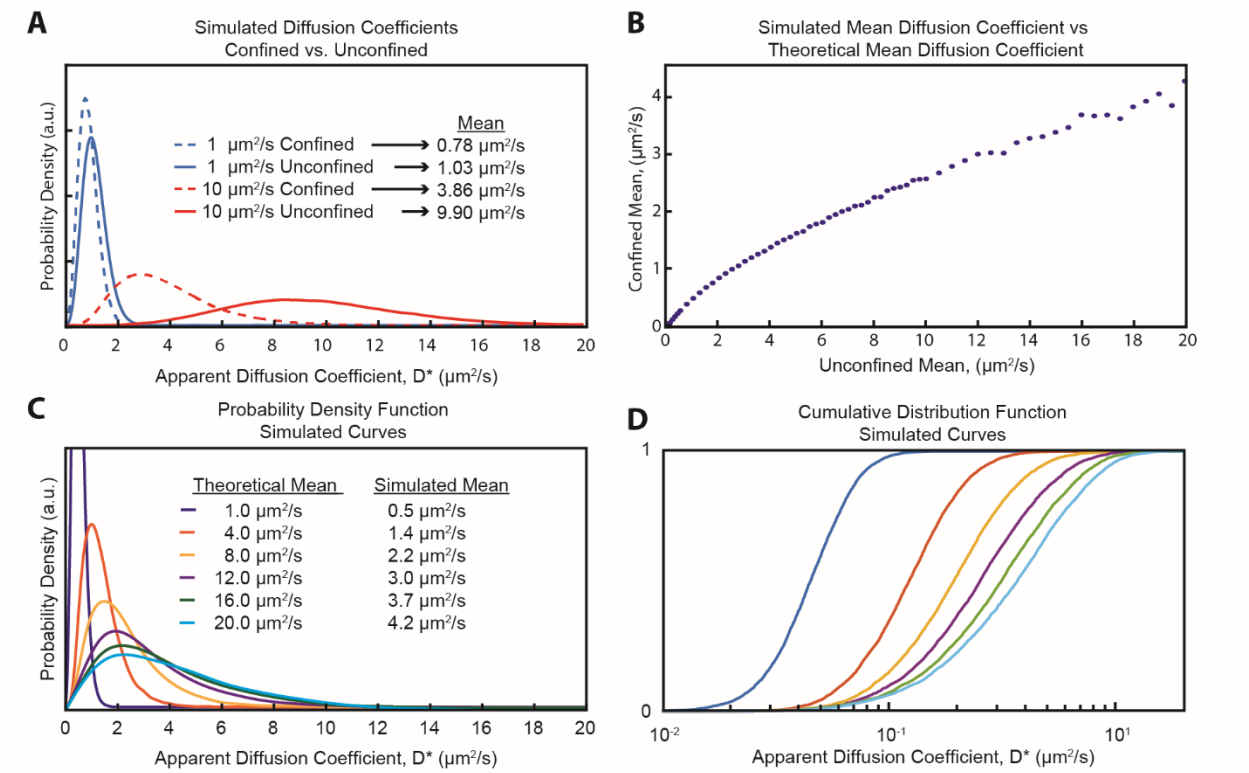

Fig. 4.7. Monte-Carlo simulation of apparent diffusion coefficient distributions. (a) Left-shift of apparent diffusion coefficient distributions due to cellular confinement for simulated trajectories. (b) Decrease in mean apparent diffusion coefficient for simulated trajectories when taking into account cellular confinement and motion blur. (c) Subset of simulated probability density functions when taking into account cellular confinement and motion blur. (d) Subset of simulated cumulative distribution functions when taking into account cellular confinement and motion blur. Colors are the same as in panel C.

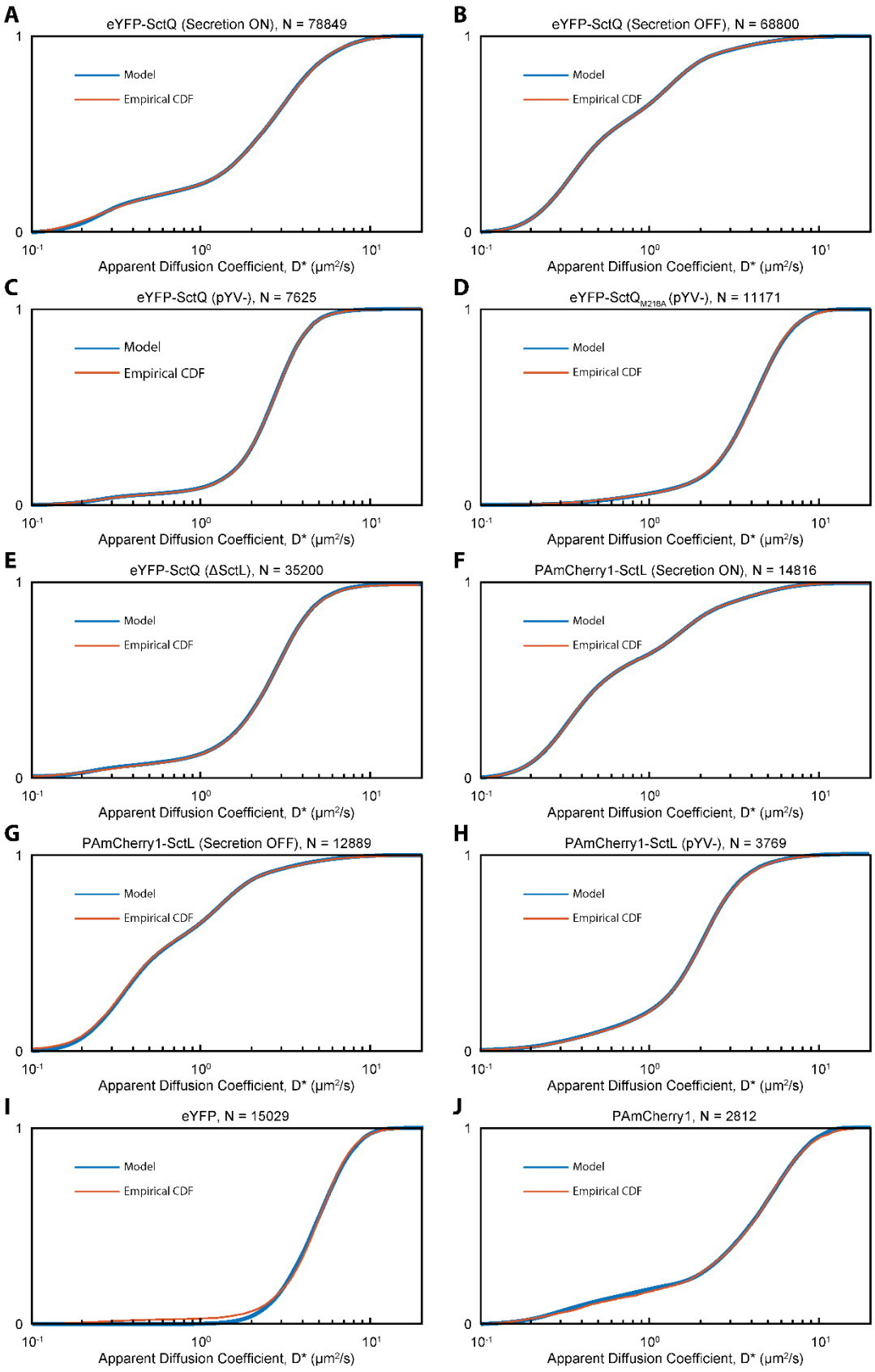
A
eYFP-SctQ (Secretion ON), N = 78849
B
eYFP-SctQ (Secretion OFF), N = 68800
C
eYFP-SctQ (pYV-), N = 7625
D
eYFP-SctQ$_{M218A}$ (pYV-), N = 11171
E
eYFP-SctQ (ΔSctL), N = 35200
F
PAmCherry1-SctL (Secretion ON), N = 14816
G
PAmCherry1-SctL (Secretion OFF), N = 12889
H
PAmCherry1-SctL (pYV-), N = 3769
I
eYFP, N = 15029
J
PAmCherry1, N = 2812
Model
Empirical CDF
Apparent Diffusion Coefficient, D* (μm²/s)

Fig. 4.8. Apparent diffusion coefficient distributions measured in live *Y. enterocolitica* cells and corresponding fits (shown as CDFs). (a) eYFP-SctQ Secretion ON, (b) eYFP-SctQ Secretion OFF, (c) eYFP-SctQ in pYV- background, (d) eYFP-$SctQ_{M218A}$ in pYV- background, (e) eYFP-SctQ, ΔSctL (f) PAmCherry1-SctL Secretion ON, (g) PAmCherry1-SctL Secretion OFF, (h) PAmCherry1-SctL in pYV- background, (i) eYFP, (j) PAmCherry1.

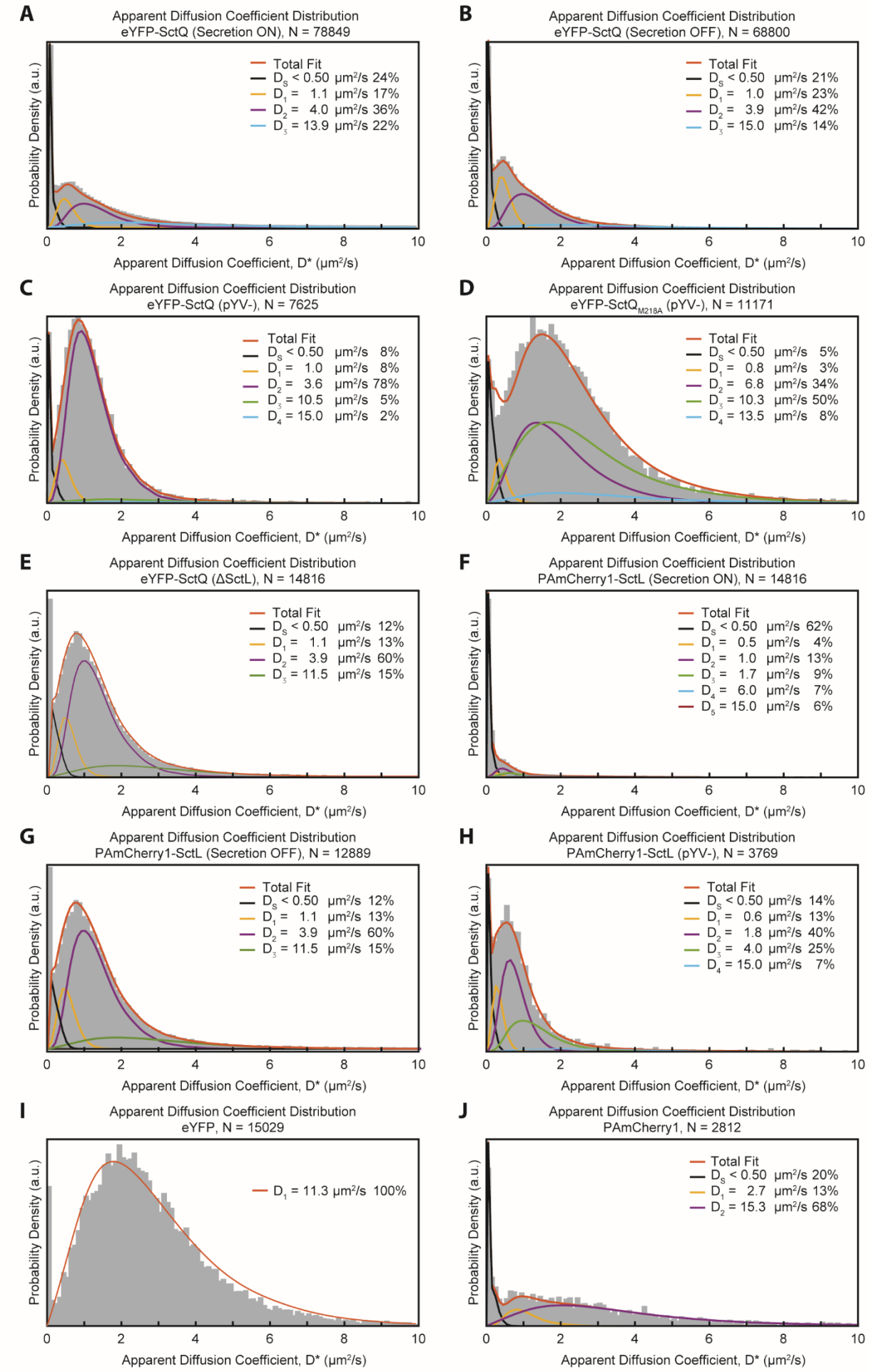
A
Apparent Diffusion Coefficient Distribution
eYFP-SctQ (Secretion ON), N = 78849
Total Fit
D_S < 0.50 µm²/s 24%
D_1 = 1.1 µm²/s 17%
D_2 = 4.0 µm²/s 36%
D_3 = 13.9 µm²/s 22%
B
Apparent Diffusion Coefficient Distribution
eYFP-SctQ (Secretion OFF), N = 68800
Total Fit
D_S < 0.50 µm²/s 21%
D_1 = 1.0 µm²/s 23%
D_2 = 3.9 µm²/s 42%
D_3 = 15.0 µm²/s 14%
C
Apparent Diffusion Coefficient Distribution
eYFP-SctQ (pYV-), N = 7625
Total Fit
D_S < 0.50 µm²/s 8%
D_1 = 1.0 µm²/s 8%
D_2 = 3.6 µm²/s 78%
D_3 = 10.5 µm²/s 5%
D_4 = 15.0 µm²/s 2%
D
Apparent Diffusion Coefficient Distribution
eYFP-SctQ$_{M218A}$ (pYV-), N = 11171
Total Fit
D_S < 0.50 µm²/s 5%
D_1 = 0.8 µm²/s 3%
D_2 = 6.8 µm²/s 34%
D_3 = 10.3 µm²/s 50%
D_4 = 13.5 µm²/s 8%
E
Apparent Diffusion Coefficient Distribution
eYFP-SctQ (ΔSctL), N = 14816
Total Fit
D_S < 0.50 µm²/s 12%
D_1 = 1.1 µm²/s 13%
D_2 = 3.9 µm²/s 60%
D_3 = 11.5 µm²/s 15%
F
Apparent Diffusion Coefficient Distribution
PAmCherry1-SctL (Secretion ON), N = 14816
Total Fit
D_S < 0.50 µm²/s 62%
D_1 = 0.5 µm²/s 4%
D_2 = 1.0 µm²/s 13%
D_3 = 1.7 µm²/s 9%
D_4 = 6.0 µm²/s 7%
D_5 = 15.0 µm²/s 6%
G
Apparent Diffusion Coefficient Distribution
PAmCherry1-SctL (Secretion OFF), N = 12889
Total Fit
D_S < 0.50 µm²/s 12%
D_1 = 1.1 µm²/s 13%
D_2 = 3.9 µm²/s 60%
D_3 = 11.5 µm²/s 15%
H
Apparent Diffusion Coefficient Distribution
PAmCherry1-SctL (pYV-), N = 3769
Total Fit
D_S < 0.50 µm²/s 14%
D_1 = 0.6 µm²/s 13%
D_2 = 1.8 µm²/s 40%
D_3 = 4.0 µm²/s 25%
D_4 = 15.0 µm²/s 7%
I
Apparent Diffusion Coefficient Distribution
eYFP, N = 15029
D_1 = 11.3 µm²/s 100%
J
Apparent Diffusion Coefficient Distribution
PAmCherry1, N = 2812
Total Fit
D_S < 0.50 µm²/s 20%
D_1 = 2.7 µm²/s 13%
D_2 = 15.3 µm²/s 68%
Probability Density (a.u.)
Apparent Diffusion Coefficient, D* (µm²/s)
0
2
4
6
8
10

Figure 4.9. Apparent diffusion coefficients distributions measured in live *Y. enterocolitica* cells and corresponding fits (shown as PDFs). (a) eYFP-SctQ Secretion ON, (b) eYFP-SctQ Secretion OFF, (c) eYFP-SctQ in pYV- background, (d) eYFP-SctQ$_{M218A}$ in pYV- background, (e) eYFP-SctQ, ΔSctL (f) PAmCherry1-SctL Secretion ON, (g) PAmCherry1-SctL Secretion OFF, (h) PAmCherry1-SctL in pYV- background, (i) eYFP, (j) PAmCherry1.

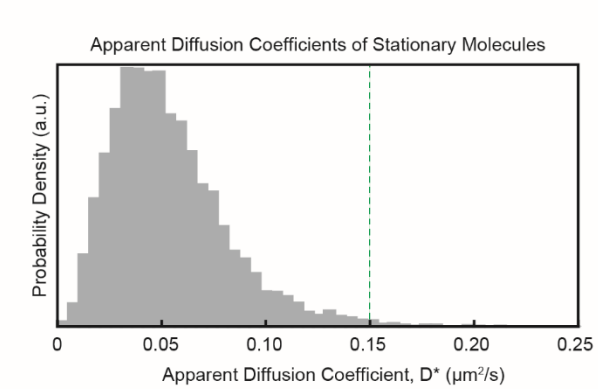

Fig 4.10. Diffusion coefficient distribution of simulated stationary emitters. Mean localization precisions for x, y, and z positions are 30 nm, 30 nm, and 50 nm, respectively. A threshold of 0.15 $\mu m^2/s$ (dashed green line) was chosen to score trajectories as originating from stationary emitters.

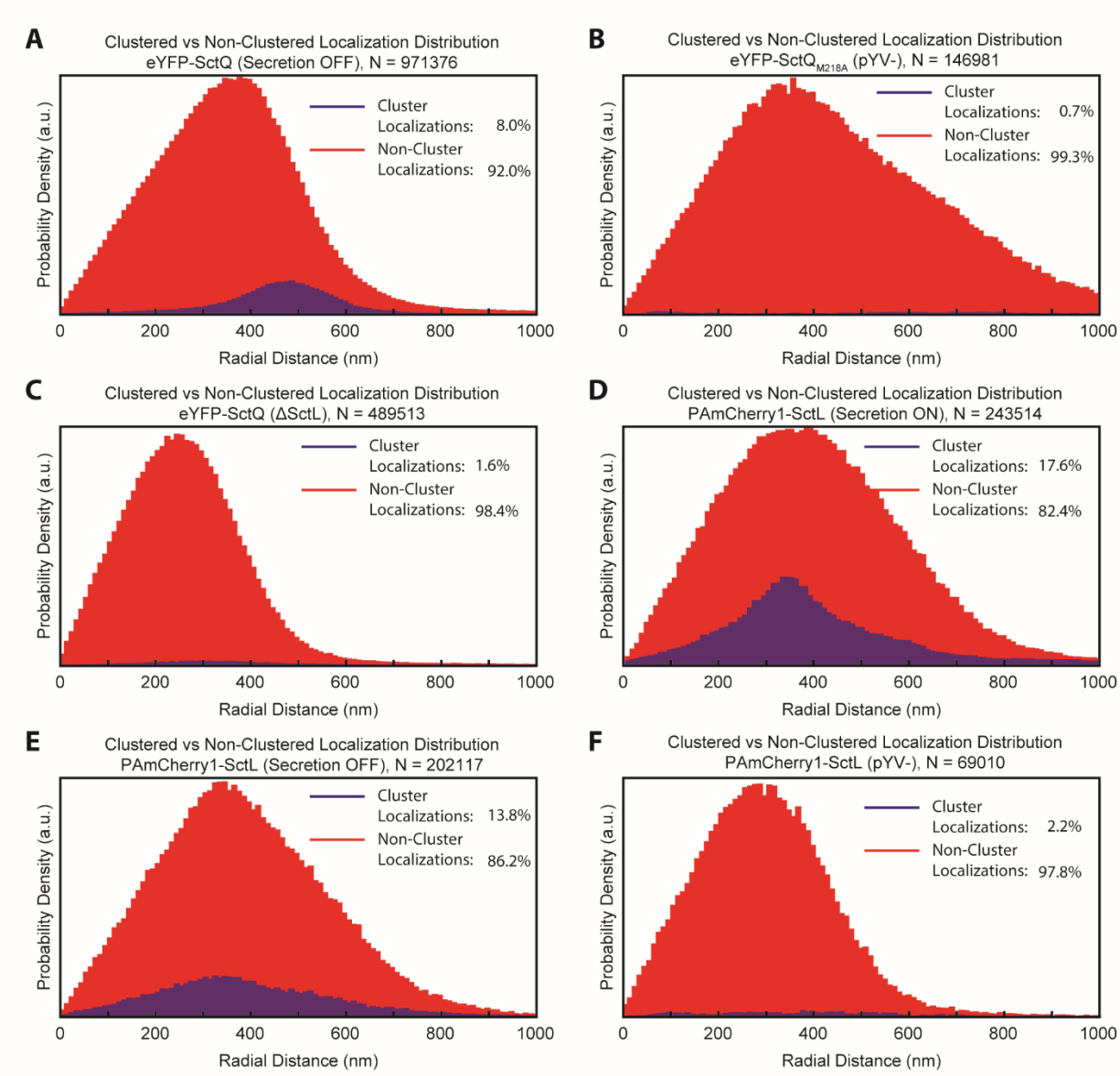

Fig. 4.11. Radial distribution functions of clustered vs. non-clustered single-molecule localizations. (a) eYFP-SctQ Secretion OFF, (b) eYFP-SctQ$_{M218A}$ in pYV- background, (c) eYFP-SctQ, ΔSctL (d) PAmCherry1-SctL Secretion ON, (e) PAmCherry1-SctL Secretion OFF, (f) PAmCherry1-SctL in pYV- background.

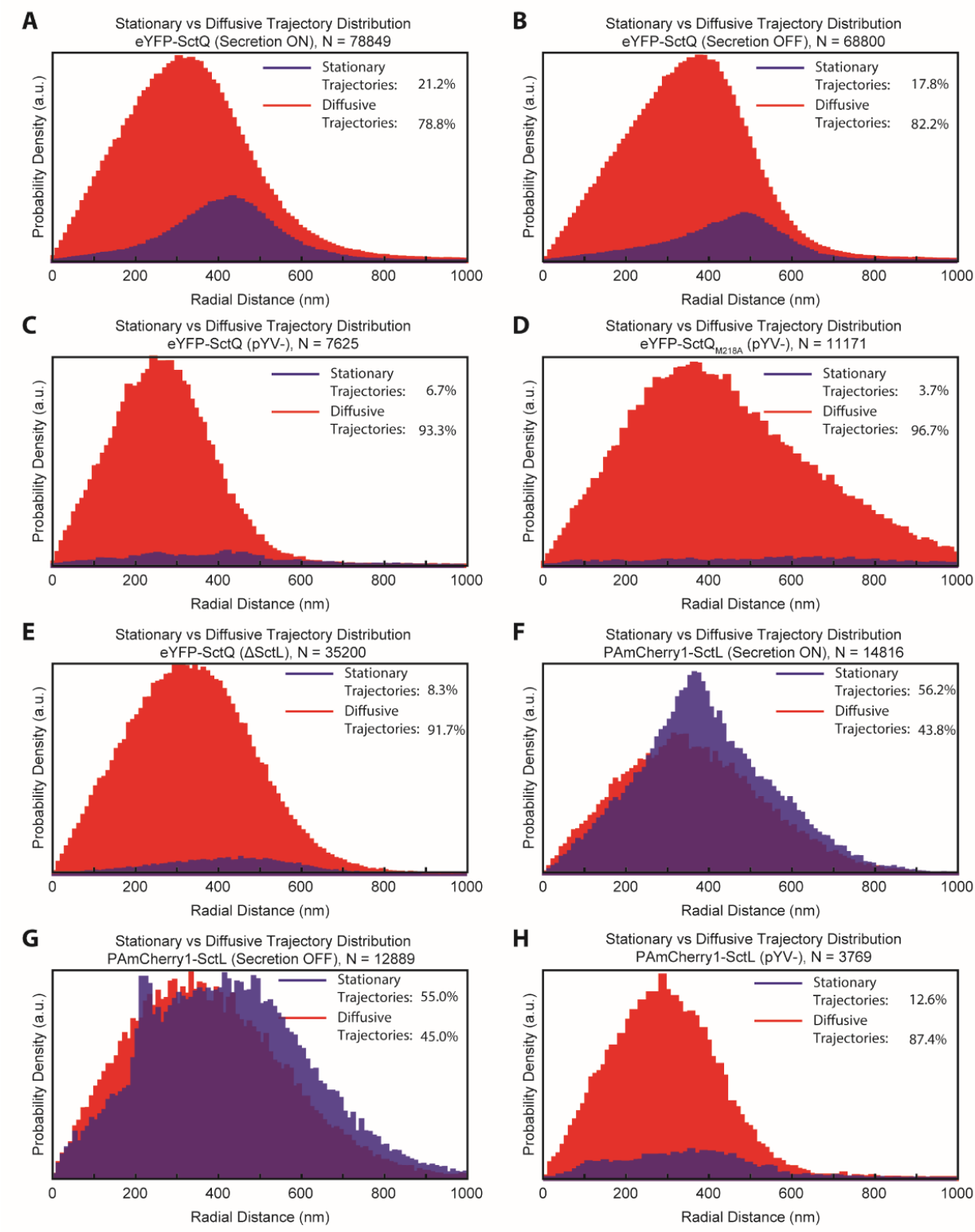
A
Stationary vs Diffusive Trajectory Distribution
eYFP-SctQ (Secretion ON), N = 78849
Stationary Trajectories: 21.2%
Diffusive Trajectories: 78.8%
B
Stationary vs Diffusive Trajectory Distribution
eYFP-SctQ (Secretion OFF), N = 68800
Stationary Trajectories: 17.8%
Diffusive Trajectories: 82.2%
C
Stationary vs Diffusive Trajectory Distribution
eYFP-SctQ (pYV-), N = 7625
Stationary Trajectories: 6.7%
Diffusive Trajectories: 93.3%
D
Stationary vs Diffusive Trajectory Distribution
eYFP-SctQM218A (pYV-), N = 11171
Stationary Trajectories: 3.7%
Diffusive Trajectories: 96.7%
E
Stationary vs Diffusive Trajectory Distribution
eYFP-SctQ (ΔSctL), N = 35200
Stationary Trajectories: 8.3%
Diffusive Trajectories: 91.7%
F
Stationary vs Diffusive Trajectory Distribution
PAmCherry1-SctL (Secretion ON), N = 14816
Stationary Trajectories: 56.2%
Diffusive Trajectories: 43.8%
G
Stationary vs Diffusive Trajectory Distribution
PAmCherry1-SctL (Secretion OFF), N = 12889
Stationary Trajectories: 55.0%
Diffusive Trajectories: 45.0%
H
Stationary vs Diffusive Trajectory Distribution
PAmCherry1-SctL (pYV-), N = 3769
Stationary Trajectories: 12.6%
Diffusive Trajectories: 87.4%
Probability Density (a.u.)
Radial Distance (nm)
0
200
400
600
800
1000

Fig. 4.12. Radial distribution functions of diffusive (D > 0.15 $\mu m^2/s$) vs. stationary (D < 0.15 $\mu m^2/s$) trajectories. (a) eYFP-SctQ Secretion ON, (b) eYFP-SctQ Secretion OFF, (c) eYFP-SctQ in pYV- background, (d) eYFP-$SctQ_{M218A}$ in pYV- background, (e) eYFP-SctQ, ΔSctL, (f) PAmCherry1-SctL Secretion ON, (g) PAmCherry1-SctL Secretion OFF, (h) PAmCherry1-SctL in pYV- background.

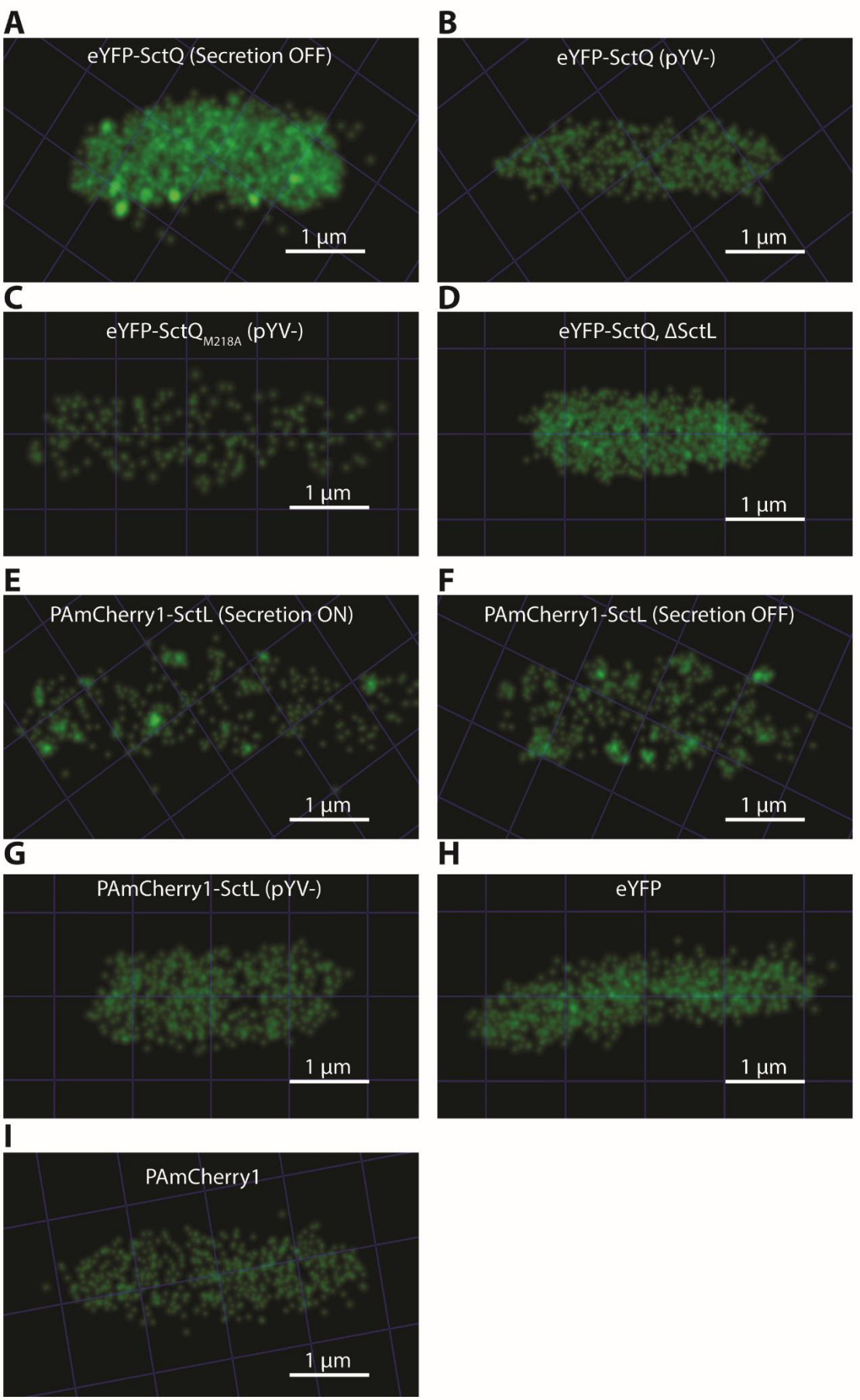
A
eYFP-SctQ (Secretion OFF)
1 µm
B
eYFP-SctQ (pYV-)
1 µm
C
eYFP-SctQ$_{M218A}$ (pYV-)
1 µm
D
eYFP-SctQ, ΔSctL
1 µm
E
PAmCherry1-SctL (Secretion ON)
1 µm
F
PAmCherry1-SctL (Secretion OFF)
1 µm
G
PAmCherry1-SctL (pYV-)
1 µm
H
eYFP
1 µm
I
PAmCherry1
1 µm

Fig. 4.13. Rendering of individual cells for each strain. (a) eYFP-SctQ Secretion OFF, (b) eYFP-SctQ in pYV- background, (c) eYFP-$SctQ_{M218A}$ in pYV- background, (d) eYFP-SctQ, ΔSctL (e) PAmCherry1-SctL Secretion ON, (f) PAmCherry1-SctL Secretion OFF, (g) PAmCherry1-SctL in pYV- background, (h) eYFP, (i) PAmCherry1.

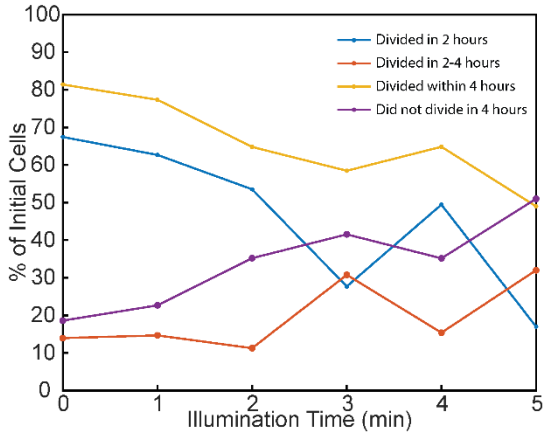

Fig. 4.14. Cell Viability Tests. Fields-of-view (FOV) containing ~80-100 cells were illuminated with 514 nm laser light at experimental laser intensities (~350 W/cm^2) for different lengths of time and then observed over the course of 4 hours. At time points of 0, 2, and 4 hours, a phase contrast image was acquired for each FOV. The phase contrast images were compared to quantify cell division occurring between time points.

Table 4.1. Fitted diffusion coefficients and relative population fractions.

eYFP-SctQ Secretion ON		**eYFP-SctQ Secretion OFF**		**eYFP-SctQ pYV$^-$**		**eYFP-SctQ$_{M218A}$ pYV$^-$**		**eYFP-SctQ ΔSctL**	
(%)	*D* (μm^2/s)	%	*D* (μm^2/s)	%	*D* (μm^2/s)	%	*D* (μm^2/s)	%	*D* (μm^2/s)
24	<0.50	21	<0.50	8	<0.50	5	<0.50	12	<0.50
17 (±2)	1.1 (±0.05)	23 (±1)	1.0 (±0.05)	8 (±3)	1.0 (±0.2)	3 (±1)	0.8 (±0.2)	13 (±3)	1.1 (±0.1)
36 (±2)	4.0 (±0.2)	42 (±4)	3.9 (±0.2)	78 (±7)	3.6 (±0.2)	34 (±16)	6.8 (±0.9)	60 (±3)	3.9 (±0.2)
22 (±3)	13.9 (±1.4)	14 (±7)	15.0 (±2.3)	5 (±5)	10.5 (±1.0)	50 (±26)	10.3 (±1.4)	15 (±2)	11.6 (±0.3)
				2 (±2)	15.0 (±3.7)	8 (±8)	13.5 (±1.5)		
PAmCherry1-SctL Secretion ON		**PAmCherry1-SctL Secretion OFF**		**PAmCherry1-SctL pYV$^-$**		**eYFP**		**PAmCherry1**	
%	*D* (μm^2/s)	%	*D* (μm^2/s)	%	*D* (μm^2/s)	%	*D* (μm^2/s)	%	*D* (μm^2/s)
62	<0.50	58	<0.50	14	<0.50			20	<0.50
4 (±4)	0.5 (±0.1)	14 (±7)	0.6 (±0.1)	13 (±5)	0.6 (±0.15)	100	11.3 (±0.2)	13 (±6)	2.7 (±0.6)
13 (±8)	1.0 (±0.2)	17 (±7)	1.1 (±0.15)	40 (±11)	1.8 (±0.25)			68 (±5)	15.3 (±0.7)
9 (±4)	1.7 (±0.4)	6 (±2)	4.0 (±0.75)	25 (±10)	4.0 (±0.8)				
7 (±2)	6.0 (±0.7)	5 (±1)	15.3 (±3.0)	7 (±3)	15.0 (±3.2)				
6 (±1)	15.0 (±2.8)								

Table 4.2. List of strains and plasmids.

Strain Name	pYV Background	Characteristics	Ref
Wild-type	IML421	pYV40 *yopO*$_{\Delta 2\text{-}427}$ *yopE*$_{21}$ *yopH*$_{\Delta 1\text{-}352}$ *yopM*$_{23}$ *yopP*$_{23}$ *yopT*$_{135}$ Δ*asd*	(35)
pYV-	--	Lacking pYV40 plasmid	
AD4085	Wild-type	*egfp-yscQ*	(35)
AD4442	Wild-type	*eyfp-yscQ*	This work
AD4459	Wild-type	*pamcherry1-yscL*	This work
AD4601	Wild-type	*eyfp-yscQ*, ΔyscL	This work
AG0001	pYV-	pBAD-eYFP-YscQ	This work
AG0002	pYV-	pBAD-eYFP-YscQ$_{M218A}$	This work
AG0003	Wild-type	pAH12-eYFP	This work
AG0004	Wild-type	pAH12-PAmCherry1	This work
AG0005	pYV-	pBAD-PAmCherry1-YscL	This work
AD4419	Wild-type	*ΔyscQ*	(48)
	ΔyscQ	pBAD-eYFP-YscQ	This work
	ΔyscQ	pBAD-eYFP-YscQ$_{M218A}$	This work

Table 4.3: Confidence intervals obtained by bootstrapping.

eYFP-SctQ Secretion ON

	Population Fraction			Diffusion Coefficient		
	min	**mean**	**max**	**min**	**mean**	**max**
State 1	0.16	0.17	0.19	1.06	1.09	1.14
State 2	0.35	0.36	0.37	3.84	3.92	4.21
State 3	0.20	0.23	0.24	13.43	13.62	15.00

eYFP-SctQ Secretion OFF

	Population Fraction			Diffusion Coefficient		
	min	**mean**	**max**	**min**	**mean**	**max**
State 1	0.22	0.23	0.24	0.94	0.97	1.01
State 2	0.37	0.41	0.42	3.71	3.92	3.97
State 3	0.00	0.01	0.10	6.65	9.61	11.50
State 4	0.07	0.14	0.15	15.00	15.16	17.55

eYFP-SctQ pYV-

	Population Fraction			Diffusion Coefficient		
	min	**mean**	**max**	**min**	**mean**	**max**
State 1	0.05	0.08	0.11	0.75	0.96	1.19
State 2	0.68	0.76	0.82	3.43	3.57	3.70
State 3	0.00	0.07	0.33	8.89	9.91	10.64
State 4	0.00	0.00	0.06	11.00	13.72	17.55

eYFP-SctQ$_{M218A}$ pYV-

	Population Fraction			Diffusion Coefficient		
	min	**mean**	**max**	**min**	**mean**	**max**
State 1	0.03	0.03	0.04	0.71	0.80	1.03
State 2	0.15	0.35	0.51	6.53	6.84	7.70
State 3	0.24	0.50	0.95	10.06	10.31	11.7
State 4	0	0.07	0.19	11.97	13.55	15.1

PAmCherry1-SctL Secretion ON

	Population Fraction			Diffusion Coefficient		
	min	**mean**	**max**	**min**	**mean**	**max**
State 1	0.01	0.04	0.09	0.41	0.55	0.65
State 2	0.05	0.13	0.18	0.82	1.01	1.09
State 3	0.05	0.08	0.12	1.33	1.71	1.97
State 4	0.05	0.07	0.09	5.09	5.88	6.00
State 5	0.05	0.06	0.07	13.68	14.97	17.88

PAmCherry1-SctL Secretion OFF

	Population Fraction			Diffusion Coefficient		
	min	**mean**	**max**	**min**	**mean**	**max**
State 1	0.09	0.14	0.21	0.49	0.56	0.66
State 2	0.10	0.17	0.22	0.99	1.09	1.26
State 3	0.05	0.06	0.08	3.34	3.93	4.75
State 4	0.04	0.05	0.06	13.69	15.21	18.28

PAmCherry1-SctL pYV-

	Population Fraction			Diffusion Coefficient		
	min	**mean**	**max**	**min**	**mean**	**max**
State 1	0.08	0.13	0.18	0.49	0.63	0.75
State 2	0.32	0.40	0.51	1.50	1.76	2.00
State 3	0.15	0.25	0.34	3.57	3.96	4.74
State 4	0.05	0.07	0.10	11.50	14.73	17.61

eYFP

	Population Fraction			Diffusion Coefficient		
	min	**mean**	**max**	**min**	**mean**	**max**
State 1	1.00	1.00	1.00	11.12	11.26	11.38

PAmCherry1

	Population Fraction			Diffusion Coefficient		
	min	**mean**	**max**	**min**	**mean**	**max**
State 1	0.08	0.13	0.19	2.10	2.84	3.90
State 2	0.62	0.67	0.72	14.64	15.34	15.89

eYFP-SctQ, ΔSctL

	Population Fraction			Diffusion Coefficient		
	min	**mean**	**max**	**min**	**mean**	**max**
State 1	0.12	0.13	0.16	1.04	1.12	1.21
State 2	0.58	0.60	0.61	3.81	3.89	4.07
State 3	0.14	0.15	0.16	11.36	11.57	11.81

Table 4.4: Mean apparent diffusion coefficients (D* > 0.15 µm^2/s) for all data sets.

	Mean D* (µm^2/s)
eYFP-SctQ Secretion ON	1.69
eYFP-SctQ Secretion OFF	1.43
eYFP-SctQ pYV-	1.30
eYFP-SctQ$_{M218A}$ pYV-	2.35
eYFP-SctQ, ΔSctL	1.33
PAmCherry1-SctL Secretion ON	1.10
PAmCherry1-SctL Secretion OFF	0.86
PAmCherry1-SctL pYV-	1.07
eYFP	2.87
PAmCherry1	2.93

Chapter 5: Resolving Cytosolic Diffusive States in Bacteria by Single-Molecule Tracking

5.1 Abstract

The trajectory of a single protein in the cytosol of a living cell contains information about its molecular interactions in its native environment. However, it has remained challenging to accurately resolve and characterize the diffusive states that can manifest in the cytosol using analytical approaches based on simplifying assumptions. Here, we show that multiple intracellular diffusive states can be successfully resolved if sufficient single-molecule trajectory information is available to generate well-sampled distributions of experimental measurements and if experimental biases are taken into account during data analysis. To address the inherent experimental biases in camera-based and MINFLUX-based single-molecule tracking, we use an empirical data analysis framework based on Monte Carlo simulations of confined Brownian motion. This framework is general and adaptable to arbitrary cell geometries and data acquisition parameters employed in 2D or 3D single-molecule tracking. We show that, in addition to determining the diffusion coefficients and populations of prevalent diffusive states, the timescales of diffusive state switching can be determined by stepwise increasing the time window of averaging over subsequent single-molecule displacements. Time-averaged diffusion (TAD) analysis of single-molecule tracking data may thus provide quantitative insights into binding and unbinding reactions among rapidly diffusing molecules that are integral for cellular functions.

5.2 Introduction

Several approaches have been developed in recent years to extract the diffusion rates and population fractions of different diffusive states that manifest for unbound molecules in confined cellular environments. These approaches account for confinement effects by the cell boundaries either (semi-)analytically (129-132) or numerically through Monte Carlo simulation of Brownian diffusion trajectories (124, 128, 133-135). Here, we test and experimentally validate a numerical analysis framework based on Monte Carlo simulations for both 2D and 3D single-molecule tracking in bacterial cells (**Fig. 5.1**). By explicitly accounting for confinement as well as 'motion-blur' of diffusing molecules inside small bacterial cells, we extract the *unconfined* diffusion coefficients for two genetically encoded fluorescence proteins, eYFP and mEos3.2, in living *Y. enterocolitica* cells. Using simulated 2D or 3D single-molecule tracking data of known diffusive state composition, we quantify to what extent two or more simultaneously present diffusive states can be resolved by numerical fitting of the displacement or apparent diffusion coefficient distributions. Finally, we consider the influence of dynamic transitions between different diffusive states that may manifest upon association and dissociation of freely diffusing molecules. We propose a new approach, based on time-averaged diffusion (TAD) analysis, to determine the timescales of such association and dissociation dynamics. We conclude that quantitative numerical analysis of 2D and 3D single-molecule trajectories can provide accurate estimations of diffusion rates, population fractions, and interconversion rates of prevalent intracellular diffusive states. Such information is crucial

for investigating the dynamic molecular-level events that regulate the functional outputs of signaling and control networks in living cells.

5.3 Materials and Methods

5.3.1 Super-resolution Fluorescence Imaging Setup

Experiments were performed on a custom-built dual-color inverted fluorescence microscope as described in section 4.3.4.

5.3.2 Data Analysis

Raw image processing and analysis for DHPSF (3D) images was carried out as described in section 3.1. Standard (2D) PSF images were analyzed using centroid estimation (166). Single molecule localizations were assigned to individual cells as described in section 3.2.1. Analysis of high density regions of localizations was carried out as described in section 3.2.2. Single-Molecule Tracking was performed as described in section 3.3.1. To resolve the unconfined diffusion coefficients of experimentally measured apparent diffusion coefficients, we performed Monte Carlo simulations of confined Brownian motion as described in section 3.3.2 for 3D simulations. However, the procedure in section 3.3.2 was slightly modified for 2D simulations. For 2D simulations, we summed 50 standard PSFs (approximated as 2D Gaussians with FWHM ~ 325 nm) corresponding to 50 periodically sampled positions of a fluorescent emitter during the camera exposure

time (25ms). Because the DHPSF has a larger cross section than the standard PSF, fewer photons are necessary for localizing emitters in 2D. To match photon counts measured experimentally, we scaled the photon count of each simulated image to 500 photons per localization for the standard PSF and 1000 photons per localization for the DHPSF. To normalize to the total photon budget, we simulated 3D trajectories with 5 displacements (3D) and 2D trajectories with 11 displacements. Experimental distributions of apparent diffusion coefficients or displacements were fit using a linear combination of simulated distributions as described in section 3.3.3.

5.3.6 Simulation of MINFLUX Trajectories

To simulate experimental tracking data obtained by MINFLUX microscopy, we first computed three-dimensional isotropic Brownian motion trajectories, sampled at high time resolution and confined within a spherocylinder of length l = 5 μm and radius r = 0.4 μm (same as for camera-based tracking). The short time-step for each displacement was 1 μs and the total trajectory length was 20 ms. We assumed exponentially distributed fluorescence blinking on- and off-times with t_{on} = 2 ms and t_{off} = 0.6 ms, in agreement with experimental measurements of the fluorescent protein mEos2 (167). As before, we simulated 5000 trajectories for 64 diffusion coefficients in the range of $D \in [0.05,15]$ μm^2/s to create libraries of distributions used for fitting of simulated experimental data. We then projected the 3D motion trajectories onto the *xy*-plane and tracked the blinking emitters using a doughnut intensity profile scanned over the emitter using a 4-step multiplex cycle, as described previously (167). The doughnut size parameter was set to *fwhm* = 800 μm and

the field-of-view scanning parameter was set to L = 400 μm. Choosing larger values for *fwhm* and L minimizes the probability of fast moving emitters (D > 5 $\mu m^2/s$) escaping from the MINFLUX observation region during tracking. The multiplex cycle time was Δt = 200 μs. To account for motion blurring during a multiplex cycle, we considered the excitation and emission probabilities from each of the computed emitter positions (sampled at 1 μs time steps). The detected photon counts were assumed to follow Poisson statistics. Emitter localization was performed with the previously described modified least mean squared (mLMS) estimator (167), with k=2, β_0 = 0.96 and β_1 = 5.75. The resulting trajectories each had 100 localizations, which were sampled every 200 μs.

5.3.7 Modeling State Transition Simulation

To address the effect of a dynamic equilibrium between two diffusive states, we simulated trajectories for which one or more state transitions take place during a single-molecule trajectory. 3D state-switching trajectories were simulated with track lengths of 5 displacements. 2D MINFLUX state-switching trajectories were simulated with track lengths of 99 displacements. We considered a two-state system in which molecules spend equal amounts of time in each state, resulting in a populations fractions of 50% for each state. The average time, T, that a molecule takes to switch from one state to the other and back again is

$$T = t_1 + t_2 \qquad (5.1),$$

where t_1 and t_2 are the average time spent in states 1 and 2, respectively. The state-switching kinetics were modeled as follows: Each individual molecule trajectory randomly started in

one of the two states. The time *t* spent in a given state before transitioning to the other was modeled as the exponential decay

$$p(t) = e^{-\frac{t}{t_1}} \tag{5.2}$$

Thus, the time spent in a given state is given by

$$\mathrm{t} = -\ln(p(t)) \cdot t_1 \tag{5.3}$$

where the value of *p(t)* was a value between 0 and 1 randomly chosen from a uniform distribution. This process was repeated, allowing the molecule to switch back and forth between the two states, until the total amount of time reached the total length of the trajectory. State-switching trajectories were then simulated for camera-based or MINFLUX-based tracking as described above.

5.3.8 Bacterial Strains and Plasmids

Plasmids for the inducible exogenous expression of fluorescent and fluorescently-tagged proteins were derived from IPTG-inducible pAH12 and arabinose-inducible pBAD vectors. The coding sequences of eYFP were PCR amplified using Q5 DNA polymerase (New England Biolabs, Ipswich, Maine) from pXYFPN-2 (156). The PCR product was isolated using a gel purification kit (Invitrogen, Carlsbad, California) and used as a megaprimer for amplification and introduction into a pAH12-derivative containing a kanamycin resistance cassette, LacI, and a lac promoter to generate pAH12-eYFP. The pAH12 backbone was a gift from Carrie Wilmot.

For the pBAD-mEos3.2, the protein coding sequence was amplified from a mEos3.2-N1 plasmid, gifted to us by Michael Davidson (Addgene plasmid # 54525). The PCR products were gel purified, and both the PCR products and the pBAD-backbone were digested with EcoRI and XhoI restriction enzymes (New England Biolabs). Digested vector and inserts were ligated using T4 DNA ligase and transformed into *E. coli* TOP10 cells. Colonies were PCR screened for presence of correct insert using GoTaq DNA Polymerase (Fisher Scientific, Hampton, New Hampshire), and plasmid was isolated from positive clones (Omega Biotek, Norcross, Georgia)

All plasmids were sequenced by GeneWiz (South Plainfield, New Jersey) prior to electroporation into *Y. enterocolitica* for analysis. Transformed cells were plated on LB agar [10 g/L peptone, 5 g/L yeast extract, 10 g/L NaCl, 1.5% agar] (Fisher Scientific, Hampton, New Hampshire) containing kanamycin [50 µg/mL] or ampicillin [200 µg/mL]. For electroporation of *Y. enterocolitica* pIML421asd cells, recovery media and plates also contained diaminopimelic acid (dap). A list of all strains and plasmids can be found in **Table 5.1**.

5.3.9 Cell Culture

Y. enterocolitica cultures were inoculated from a freezer stock in BHI media (Sigma Aldrich, St. Louis, Missouri) with nalidixic acid (Sigma Aldrich) [35 µg/mL] and 2,6-diaminopimelic acid (Chem Impex International, Wood Dale, Illinois) [80 µg/mL] one day prior to an experiment and grown at 28°C with shaking. After 24 hours, 300 µL of overnight culture was diluted in 5 mL fresh BHI, nalidixic acid, and diaminopimelic acid

(dap) and grown at 28°C for another 60-90 minutes. In addition, inoculation media also contained kanamycin or ampicillin for pAH12- or pBAD-based plasmids, respectively. Cultures of cells containing pAH12- or pBAD-based plasmids were induced with IPTG (Sigma Aldrich) [0.2 mM, final] or arabinose (Chem Impex) [0.2%], respectively, for the final 2 hours of incubation. Cells were pelleted by centrifugation at 5000 g for 3 minutes and washed 3 times with M2G (4.9 mM Na_2HPO_4, 3.1 mM KH_2PO_4, 7.5 mM NH_4Cl, 0.5 mM $MgSO_4$, 10 µM $FeSO_4$ (EDTA chelate; Sigma), 0.5 mM $CaCl_2$) with 0.2% glucose as the sole carbon source). The remaining pellet was then re-suspended in M2G and dap. Cells were plated on 1.5 – 2% agarose pads in M2G containing dap.

5.4 Results and Discussion

5.4.1 eYFP and mEos3.2 undergo confined Brownian Diffusion in *Y. enterocolitica*

To experimentally validate the numerical analysis framework based on Monte Carlo simulations of confined diffusion, we tracked the 3D motion of individual eYFP and mEos3.2 fluorescent proteins in living *Y. enterocolitica* cells. Previous studies in *E. coli* (134, 168) and *C. crescentus* (169) have established that small cytosolic proteins undergo Brownian motion. Non-specific interactions due to macromolecular crowding reduce the diffusion coefficient for small cytosolic proteins, but do not by themselves lead to measurable deviations from normal Brownian diffusion (170). In contrast, the motion of large macromolecular complexes (>30 nm in diameter) is best described by anomalous diffusion due to glass-like properties of the bacterial cytoplasm (171).

The experimentally measured distributions of apparent diffusion coefficients are fit well using a single diffusive state with D = 11.5 μm^2/s (for eYFP, **Fig. 5.2a**) and D = 15.0 μm^2/s (for mEos3.2, **Fig. 5.2b**). The close agreement between simulations and experiment confirms that the assumption of spatially confined Brownian diffusion is valid for both eYFP and mEos3.2 in *Y. enterocolitica* under our experimental conditions. These diffusion coefficient values are in agreement with previously measured values of GFP in bacteria (134, 159, 172-176). The structure and molecular weights of eYFP (27 kDa) and mEos3.2 (26 kDa) are very similar. The differences in their diffusion coefficients may thus be due to differences in non-specific transient interactions with other cellular components. We also note that there is a small (6% or less) stationary (<0.5 μm^2/s) population for both fluorescence proteins. We find small numbers of stationary trajectories in all of our single-molecule tracking datasets, which indicates that even freely diffusing cytosolic proteins may become immobilized. However we did not find that that these stationary molecules exhibit any subcellular preference.

5.4.2 2D vs 3D Single-Molecule Tracking to Estimate Diffusion Coefficients

Most single-molecule tracking results reported to-date utilize the standard PSF for 2D single-molecule tracking. Acquiring 3D trajectories requires engineered PSFs, such as astigmatic, double-helix, or tetra-pod PSFs (99, 101-103, 177, 178). A common feature of engineered PSFs is their increased footprint on the detector compared to the standard PSF. Due to their increased size, engineered PSFs require higher photon counts to achieve lateral localization precisions equivalent to those obtained with the standard PSF. Given the finite

photon-budgets of fluorescent labels, 2D tracking can thus yield longer single-molecule trajectories that contain roughly twice the number of displacements than 3D trajectories acquired with engineered PSFs.

To determine whether diffusion coefficients are more accurately estimated by 2D or by 3D tracking, we repeated the 3D DHPSF simulations using the standard PSF. We generated simulated distributions of apparent 2D diffusion coefficients in the same way as for the 3D data (**5.3 Materials and Methods**). However, the simulated 2D trajectories had twice as many displacements as the 3D trajectories to provide an equivalent total photon count over the course of a trajectory. We found that the resulting 2D apparent diffusion coefficient distributions are broader and their peaks are systematically right-shifted compared to their 3D equivalents (**Fig. 5.3a**). The increased left-shift of the 3D distribution is due to the additional confinement of the molecule's motion in the *z*-dimension that is not measured in 2D tracking.

We then performed numerical fitting of simulated 2D tracking data to estimate the diffusion coefficient. We found that there is a slight increase in accuracy when fitting 2D data compared to 3D data for a single diffusive state, particularly for fast diffusion. (**Fig. 5.3b,c**). The improved accuracy of 2D tracking may be due to the decreased similarity of the 2D distributions for fast diffusion coefficients (**Fig. 5.7**), which enables more accurate parameter estimation.

5.4.3 Single-molecule tracking can be used to resolve different diffusive states

The free fluorescent proteins examined in the previous section each exhibited a single predominant diffusive state, which means that these two proteins do not exhibit stable interactions with other cellular components. This property is important for their use as non-perturbative labels that do not alter the diffusive behaviors of the target proteins beyond an overall reduction in their native diffusion rate. An overall reduction in diffusion rate is expected due to the increased molecular weight and hydrodynamic radius of the fusion protein. If the target protein stably interacts with cognate binding partners to form homo- or heterooligomeric complexes of different sizes, then single-molecule tracking of non-perturbatively labeled target proteins may be used to resolve the corresponding diffusive states. Examples of different diffusive states reported in the recent literature include the cytosolic pre-assembly of the bacterial type 3 secretion system proteins SctQ and SctL (119), ternary complex formation of the elongation factor Tu (EF-Tu) which can bind to aminoacyl-tRNA, GTP, and translating ribosomes(128), the nucleotide excision repair initiation molecule UvrB (125), and short-lived ribosome binding of EF-P(124).

To test the resolving capability of single-molecule tracking, we simulated mixed distributions of 3D displacements or apparent diffusion coefficients that contain two different diffusive states. We then fit these distributions to obtain the unconfined diffusion coefficients and relative population fractions of each diffusive state. By systematically varying the diffusion coefficients, we assessed the error in the optimized fitting parameters for various combinations. We examined both equal (50:50) and unequal population fractions (80:20). In all cases, the distributions were based on 5000 trajectories with five

displacements each. We found that the errors in the optimized fitting parameters increased when the diffusion coefficients were similar, as evidenced by the wedge-shaped diagonal (**Fig. 5.4a**). Slight differences in diffusion rate are thus more readily resolved for slowly diffusing molecules than for faster moving ones. We reason that the ability to resolve fast diffusive states is further compromised by the confinement effect, which causes the distributions of apparent diffusion coefficients to become more similar in the high diffusion coefficient limit (**Fig. 3.2c**).

Current detector technologies, in particular large field-of-view sCMOS detectors, have made it possible to readily acquire single-molecule trajectories in thousands of cells in a single imaging session. Thus, 5,000 trajectories can be obtained even for proteins expressed at low levels. For highly expressed proteins up to 100,000 trajectories can be obtained. We therefore repeated our analysis using distributions based on 100,000 trajectories. As expected, the errors in the parameter estimates decreased (~7% on average) when fitting the now more thoroughly-sampled distributions (**Fig. 5.9**). Therefore, the resolving capability improves when additional measurements are available to sample the shape of experimental distributions. However, larger errors persist along the diagonal of the error matrices, highlighting the difficulty in resolving states with similar diffusion coefficients. When the population fractions are split 80:20, larger errors manifest due to the smaller number of proteins in the diffusive state with a 20% population fraction. In those cases, the relative error in the smaller fraction can approach 100%, i.e. the smaller fraction is completely eliminated when the fitting routine converges on a one-state solution (**5.3 Materials and Methods**).

To test whether the above results may be extrapolated to more complex state distributions, we simulated a few selected examples of mixed distributions containing three and four diffusive states, maintaining N = 5000 total trajectories in each case. We found that three states can be simultaneously resolved as long as their diffusion coefficients are sufficiently different and their population fractions are similar (**Fig. 5.10a**). Again, the errors in the fitting parameters increase for faster (i.e. more similar) diffusion coefficients (**Fig. 5.10b**). In the case of a 4-state population, the distribution is best fit with a 3-state results, even when the values of the diffusion coefficients are well separated (**Fig. 5.10c**). Specifically, the two fastest states are combined into a single state with a correspondingly larger population fraction. The 3- and 4- state simulations thus recapitulate the trends observed for binary diffusive state mixtures.

To test whether 2D tracking is also more discriminating when multiple diffusive states are present, we constructed simulated 2-state distributions of apparent diffusion coefficients based on 2D data. Again, we observed only a slight increase in the accuracy of the fitting (~3%) for the 2D fitting compared to 3D for a two state fitting **(Fig 5.4b**). We therefore conclude that 2D and 3D single-molecule tracking are roughly equivalent in their ability to resolve different diffusive states. We note however that 3D single-molecule localization microscopy has the additional advantage of providing more detailed spatial information on the subcellular locations of diffusing molecules, which may provide important additional information in select cases. We also note that the above analysis only pertains to diffusion of cytosolic proteins. The diffusion of membrane proteins is subject to different confinement effects that may make it more appropriate to track in 3D (120).

5.4.4 Transitions between diffusive states

Thus far, we have only considered diffusive states that do not interconvert on the time-scale of a single-molecule trajectory (~100-300 ms on average). Under physiological conditions, however, molecules may frequently bind to or dissociate from cognate interaction partners and thereby transition between different diffusive states. The time-resolution for making single-step displacement measurements (~25 ms) is shorter than the time resolution for determining apparent diffusion coefficients (~5 · 25 ms = ~125 ms). We therefore hypothesized that, in the presence of diffusive state switching, more accurate parameter estimates may be obtained by fitting single-step displacement distributions. To test this hypothesis, we simulated distributions for two states, D_1 = 1 μm^2/s and D_2 = 10 μm^2/s, that can interconvert on timescales comparable to a single-molecule trajectory. We then gradually decreased the average diffusive state switching time $T = (k_1)^{-1} + (k_2)^{-1} = t_1 + t_2$ and imposed $k_1 = k_2$ to keep the population fractions equal (**5.3 Materials and Methods**). To fit the single-step displacement distributions, we generated a library of simulated single-step displacement distributions as described before for apparent diffusion coefficients (**Fig. 5.8**). Both the apparent diffusion coefficient distributions and single-step displacement distributions were then fit with their respective library. To quantify the overall accuracy of the fit, we averaged the relative errors of all fitting parameters (in this case the diffusion coefficients D_1 and D_2 and the population fractions f_1 and $f_2 = 1 - f_1$. We found that, in the limit of infinitely long switching times (no state transitions), both approaches produce parameter estimates with similar accuracy (**Fig. 5.5a,b** and **Fig. 5.11**). As the average switching time is decreased, the mean relative errors start to increase for

both methods. Importantly, fitting distributions of apparent diffusion coefficients produced parameter estimates that deviated sooner from the ground truth (as a function of decreasing average switching time) than those obtained by fitting single-step displacement distributions. In the limit of short switching times, fitting of both the apparent diffusion coefficient and single-step displacement distributions produced large errors, because a single molecule can sample both diffusive states repeatedly during the timescale of the measurement. When using 25 ms exposure times, accurate parameter estimates can be made for this two-state system, if $T > 75$ ms and $T > 500$ ms for displacement and apparent diffusion coefficient fitting, respectively. For accurate extraction of the parameters, the time resolution of the measurement should be about three times shorter than the average switching time T.

The above observations suggest that it should be possible to estimate the timescale of diffusive state switching by time-averaged diffusion (TAD) analysis, i.e. by varying the number of averaged displacements. We therefore evaluated the apparent diffusion coefficients for overlapping sub-trajectories having different numbers of displacements/localizations. Specifically, within each single-molecule trajectory, we define overlapping sub-trajectories with N_i localizations and $N_i - 1$ displacements. The number of sub-trajectories for a given N_i is $S=N-N_i+1$, where N is the number of localizations in the full-length trajectory. Defining the first localization in the sub-trajectories as P, we modified Eqn 3.1 to

$$MSD_{N_i,P} = \frac{1}{N_i-1}\sum_{n=P+1}^{N_i+P-1}(x_n - x_{n-1})^2 \qquad (5.4),$$

to obtain mean squared displacement values for different sub-trajectory lengths and starting points, namely N_i = 2, 3, …, 6 and $P=1...S$.

Based on these sets of observables, we generated five new apparent diffusion coefficient libraries corresponding to the five different values of N_i (on average our experimental 3D trajectories are 5 displacements long). The state-switching trajectories were then re-analyzed using Eqn 5.4 and fit with the corresponding library. Again, we used the mean relative error over all fitting parameters to quantify the overall accuracy of the fit for each value of N_i (**Fig. 5.5c**). Consistent with the results above, the accuracy of the fitting parameters is poor for short switching times and good for long switching times. Importantly, the mean relative errors are constant for all N_i in both of these limiting cases. Thus, if the state switching time is substantially shorter or longer than the time resolution of the measurement, then the mean error does not change. In contrast, the mean errors increase for increasing N_i, if switching times are comparable to the timescale of a single-molecules trajectory (0.05-0.5s). The same trends are also observed when plotting the individual parameter fitting results (**Fig. 5.5d**). Based on these results, we conclude that the timescale of diffusive state switching can be estimated by determining the rate of change of individual fitting parameters as a function of the number of averaged displacements. For example, based on the results in **Fig. 5.5c,d**, observing a consistent increase or decrease of individual fitting parameters as a function of N_i would indicate a diffusive state switching time between 20 and 500 ms. We note that the ground truth is unknowable in experimental work. We therefore computed an error relative to the parameter values obtained when fitting single displacement distributions (i.e. N_i = 2). Single displacement distributions offer the best time resolution and thus should be least

affected by diffusive state averaging. The parameter deviations relative to the parameter estimates at $N_i = 2$ displayed similar trends as those referenced to the ground truth (**Fig. 5.5e**).

It is clear that the dynamic range of TAD analysis improves if trajectories contain a large number of displacements. However, in camera-based tracking of fluorescent fusion proteins, only $N = 5$ or $N = 12$ displacements can be observed on average for 3D and 2D tracking, respectively. Longer trajectories can be acquired using chemical dyes (130, 179, 180) or multiple fluorophores as labels (181), but potential of non-specific labeling or the size of multivalent fluorescent tags have to be weighed against this benefit. An important advantage of camera-based tracking is that the temporal dynamic range is tunable to access slow switching timescales (>500 ms) by adjusting the exposure time and/or by acquiring single-molecule trajectories in time-lapse mode (128, 133, 182). On the other hand, exposure times shorter than a few milliseconds come at the expense of data acquisition throughput, because the full chip of current sCMOS cameras cannot be read out faster than 100 Hz (128). Thus, faster timescales are difficult to assess by camera-based tracking.

A solution to access faster time scales is MINFLUX microscopy (167). The time resolution of MINFLUX-based single-molecule tracking is two orders of magnitude better than camera-based tracking (0.2 ms vs 25 ms) and the number of localizations N is larger by one order of magnitude (N~100 vs. N~10). MINFLUX microscopy may thus be able to provide access to state switching dynamics on 0.2 ms to 20 ms timescales, whereas camera-based tracking can cover state switching dynamics on millisecond to minute timescales. To test the capability of MINFLUX microscopy to quantify fast state switching times, we applied TAD analysis to simulated MINFLUX data. MINFLUX trajectories were

generated in the same way as the camera-based trajectories, i.e. through Monte Carlo simulations of confined Brownian diffusion, but the MINFLUX localization algorithm was used instead of PSF fitting (**5.3 Materials and Methods**). We then used libraries of N_i-fold averaged MINFLUX displacement distributions to fit state-switching trajectories for different switching times T (D_1 = 1 μm^2/s, D_2 = 10 μm^2/s, $k_1 = k_2$). We found that the mean % error vs. N_i curves (**Fig. 5.6a**) displayed two key characteristics that correlate linearly with switching time T or with switching rate 1/T. First, for each switching time T, there exists a threshold value $N_{i,T}$, after which the mean % error increases linearly as a function of N_i. $N_{i,T}$ and T are linearly correlated (**Fig. 5.6a,b**). Second, the slope of the initial linear increase and the switching rate 1/T are linearly correlated as well (**Fig 5.6a,c**). Based on these linear relationships, we conclude that the timescale of state transitions can be determined from the position of $N_{i,T}$ and from the slope of the following linear increase.

Since the ground truth is not accessible by experiment, we repeated the above analysis by referencing all parameter estimates to the parameters obtained at N_i = 3 (**Fig. 5.6d**). N_i = 3 corresponds to a time resolution of 600 μs. The curves obtained by plotting the mean % deviation from the N_i = 3 parameter estimates vs. N_i displayed the same characteristic linear increases as a function of N_i. The onset of the linear increase $N_{i,T}$ and the slope of the linear increase still correlated linearly with T and 1/T, respectively (**Fig. 5.6d,e,f**). These results show that the switching rate between two diffusive states can be reliably determined by TAD analysis of 2D and 3D single-molecule tracking data.

5.5 Conclusions

In this work, we present and test a robust analysis method for estimating diffusive state parameters of fluorescently labeled biomolecules in confined bacterial cell volumes based on single-molecule tracking. We show that it is possible to resolve the unconfined diffusion coefficients and the population fractions of multiple diffusive states based on a few thousand short single-molecule trajectories obtained by camera-based tracking. The numerical analysis framework presented is generally applicable to both 2D and 3D tracking and any confinement geometry. We show that 2D and 3D single-molecule tracking are roughly equivalent in their ability to resolve multiple diffusive states. To address the issue of diffusive state switching during the timescale of measurement, we propose time-averaged diffusion (TAD) analysis. By averaging over different number of subsequent displacements, the timescale of state switching can be determined, if that timescale is comparable to the duration of the recorded trajectories. For example, MINFLUX microscopy can provide access to state switching dynamics occurring on 2-200 ms timescales using data acquisition parameters relevant for fluorescent protein localization in living cells. On the other hand, camera-based tracking can be used to detect state switching dynamics on 20 ms to seconds timescales either by using longer exposure times or by acquiring data in time-lapse mode. TAD analysis of experimental single-molecule trajectories thus provides a general and robust approach to quantify the diffusive states and diffusive state transitions that manifest in living cells.

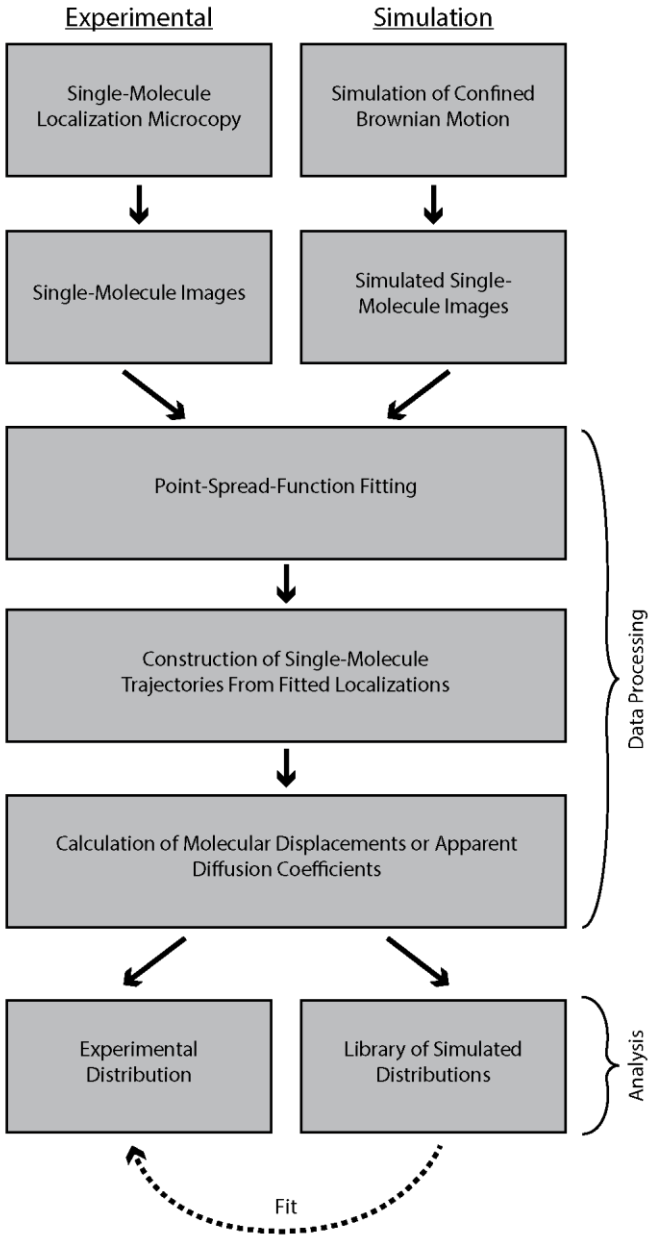

Figure 5.1. Diagram of numerical diffusion fitting analysis workflow. Experimental and simulated data are analyzed using the same data processing routines so that experimentally determined apparent diffusion coefficient (or displacement) distributions can be analyzed using linear combinations of simulated distributions.

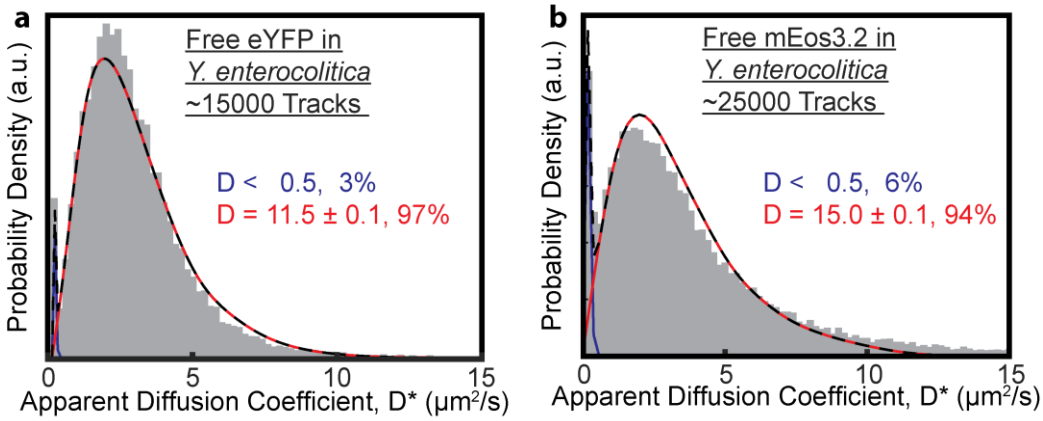

Figure 5.2. The 3D diffusion of cytosolic fluorescent proteins eYFP and mEos3.2 in *Y. enterocolitica* can be explained using a single diffusive state. (a) eYFP diffuses at 11.5 $\mu m^2/s$ (red). (b) mEos3.2 diffuses at 15.0 $\mu m^2/s$ (red). A small fraction (<6%) of stationary trajectories is present in both datasets (blue). The total fit is shown as a dashed black line.

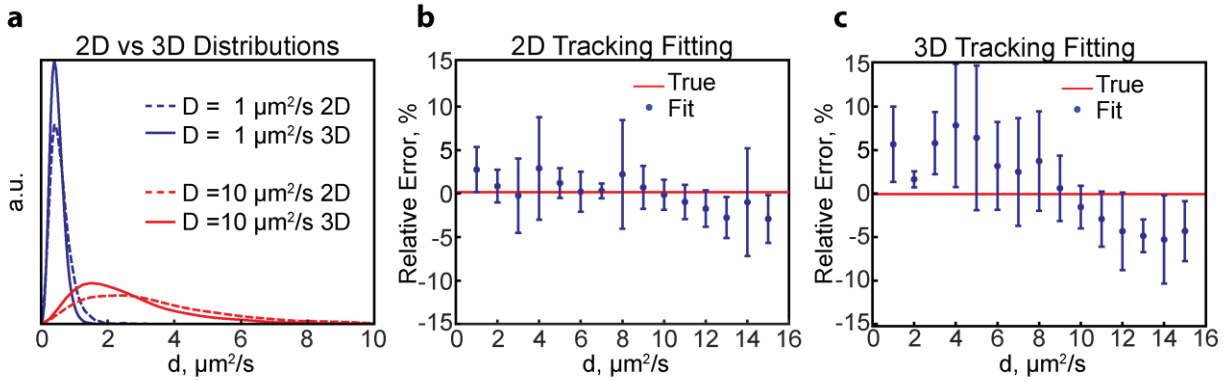

Figure 5.3. Comparison of 2D and 3D tracking. (a) Comparison of 2D and 3D apparent diffusion coefficient distributions corresponding to 1 $\mu m^2/s$ and 10 $\mu m^2/s$. The distributions for 3D tracking are left-shifted to a larger extent due to the additional confinement in the 3rd dimension. (b,c) Relative errors in determining the diffusion coefficient of a single diffusive state using 2D (b) and 3D (c) single-molecule tracking. Shown are the averages and standard deviations of four independent simulations containing N = 5000 trajectories each resampled 10 times by bootstrapping.

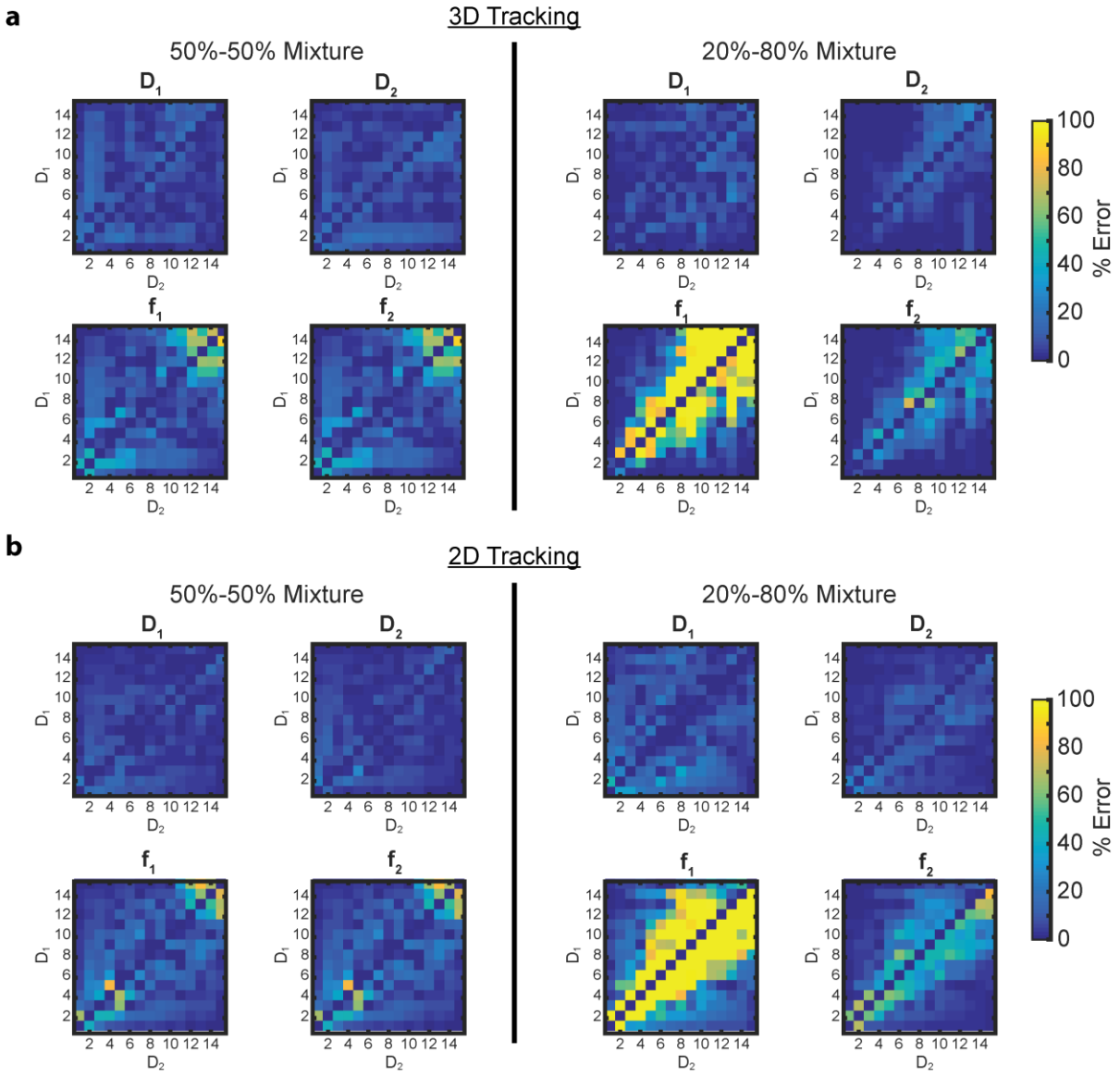

Figure 5.4. Multiple diffusive states can be resolved by numerical fitting of single-molecule tracking data using 2D and 3D tracking. (a,b) Relative errors for determining the diffusion coefficients and population fractions of binary mixtures of diffusive states using 3D (a) and 2D (b) tracking. The relative population fractions in the two state mixtures were either 50%-50% (left) or 20%-80% (right). The relative error for each fitting parameter (diffusion coefficients D_1 and D_2, and their corresponding population fractions f_1 and f_2) is

represented as a matrix for different diffusion coefficient combinations. Each pixel represents the mean (relative) error of the parameter's fit value after analyzing ten datasets (resampled by bootstrapping) each containing 5000 tracks.

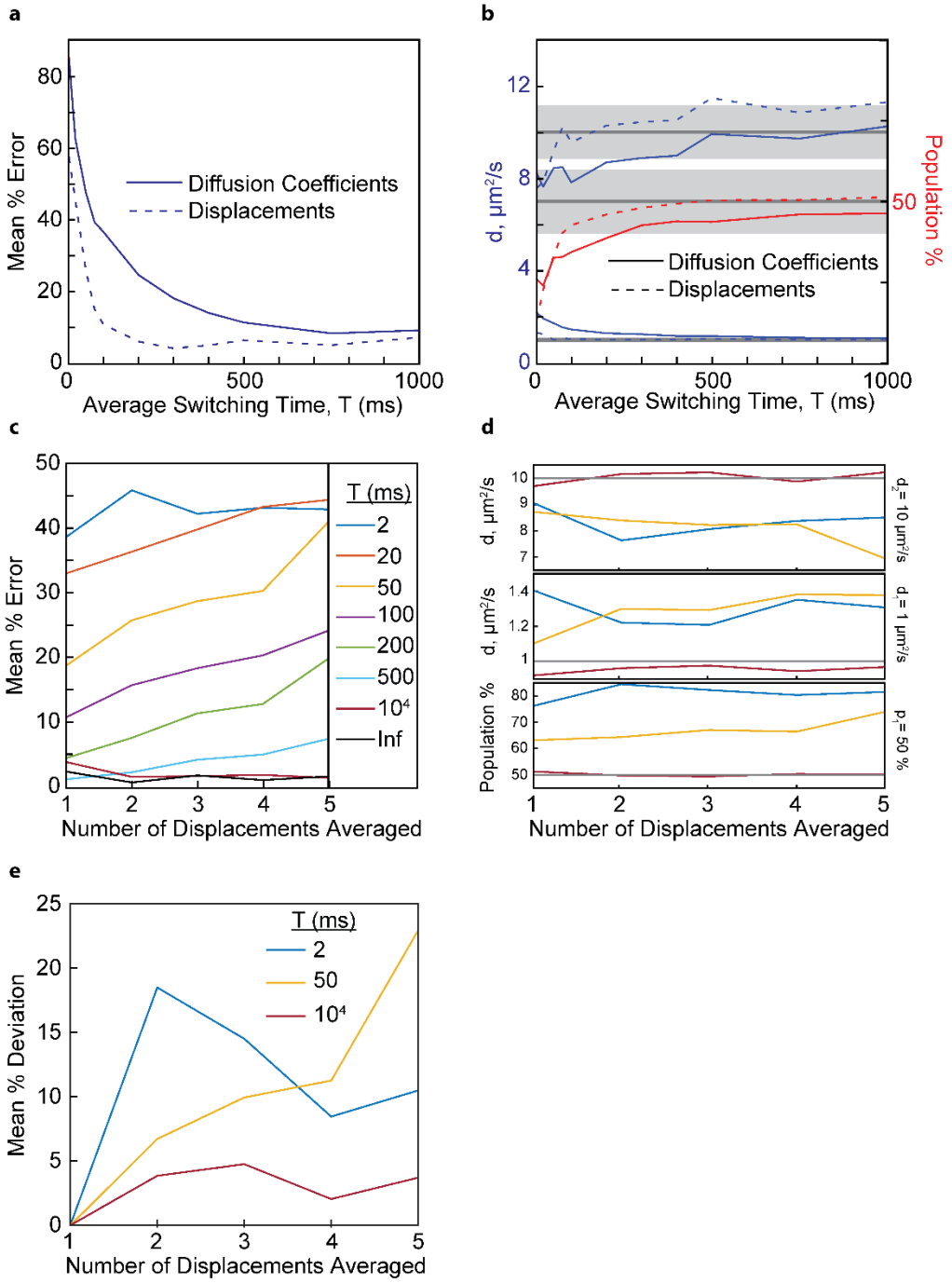

Figure 5.5. Resolving diffusive states in the presence of dynamic state transitions. (a) The mean relative errors of the fitting parameters for a 2-state mixture (D_1 = 1 μm^2/s, D_2 = 10

μm^2/s, 50:50 population fraction) as a function of different switching times between two diffusive states. The mean % error obtained by fitting the single-step displacement distributions diverges for T < 75 ms, whereas the mean % error obtained by apparent diffusion coefficient fitting diverges for T < 500 ms. (b) Individual parameter estimates as a function of state switching time for the same simulations as in (a). Population fraction $f_2 = 1 - f_1$ is not shown for clarity. (c) The mean relative errors of the fitting parameters as a function of the number of averaged displacements. The shaded areas represent 10% error limits for each parameter. (d) Parameter estimates as a function of averaged displacements for the same simulations as in panel c. Color scheme is the same as the legend in panel c. Grey lines represent the ground truth. The fitted individual parameter value produces horizontal curves for both the very short (2 ms) and very long (10^4 ms) switching times. For intermediate switching times (50 ms), the fitted values trend away from the true value as the number of averaged displacements increases. (e) Mean deviation relative to the single displacement parameter estimates (N_i = 2) for different switching times.

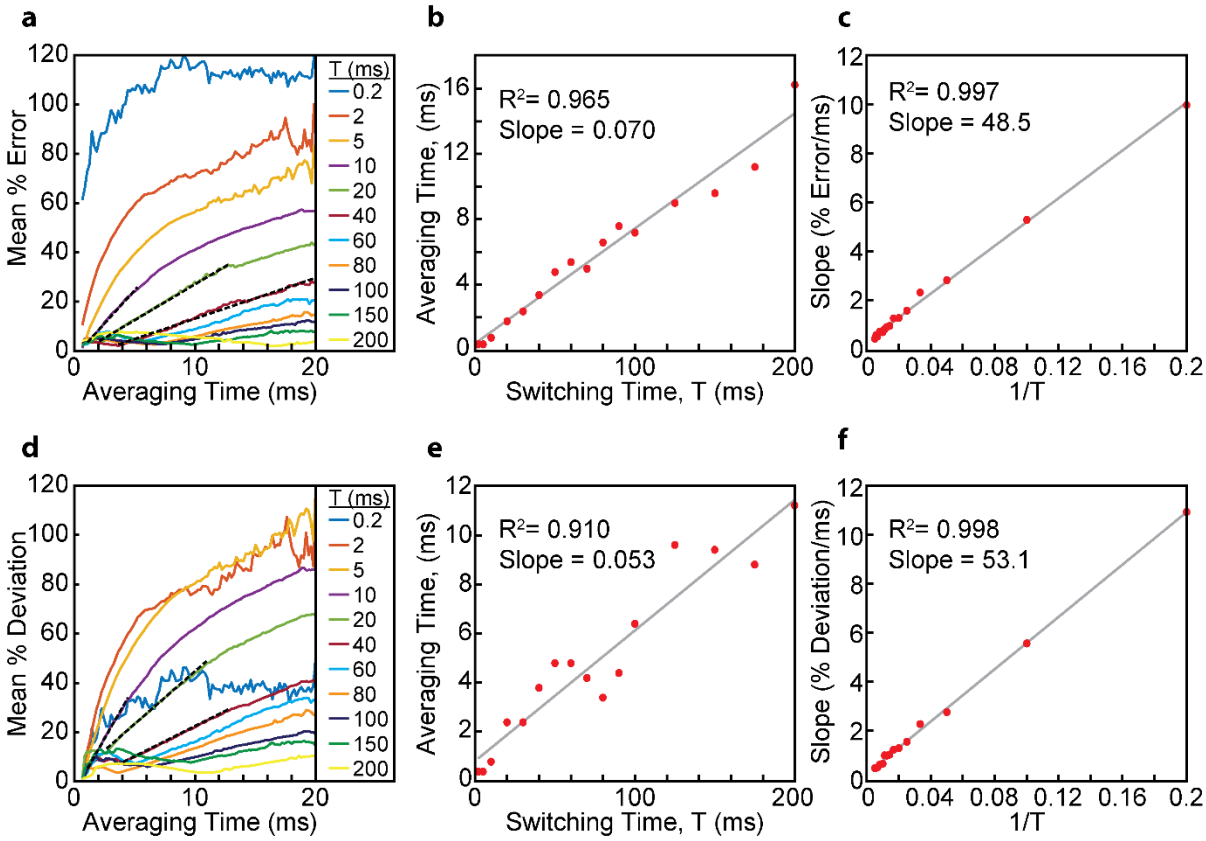

Figure 5.6. Resolving diffusive states in the presence of dynamic state transitions for MINFLUX data. (a) Mean % error in the parameter estimates compared to the ground truth for various switching times (D_1 = 1 μm^2/s, D_2 = 10 μm^2/s, $k_1 = k_2$). Initial slope determinations (dashed black lines) are shown for the T = 10, 20, and 40 ms datasets. The averaging time is the value of N_i multiplied by the multiplex cycle time Δt = 200 μs. (b) Averaging time at which the mean % error begins to linearly increase. (c) Slope of the initial linear increase of the mean % error. Switching times of 0.2 and 2 ms are not included here, because the linear section of their curves in panel are not sufficiently resolved. (d) Mean % deviation in the parameter estimates relative to the parameter estimates at N_i = 3. Again, initial slope determinations (dashed black lines) are shown for the T = 10, 20, and

40 ms datasets. (e) Averaging time at which the mean % deviation in panel d begins to linearly increase. (f) Slope of the initial linear increase of the mean % deviation in panel d. Again, switching times of 0.2 and 2 ms are not included.

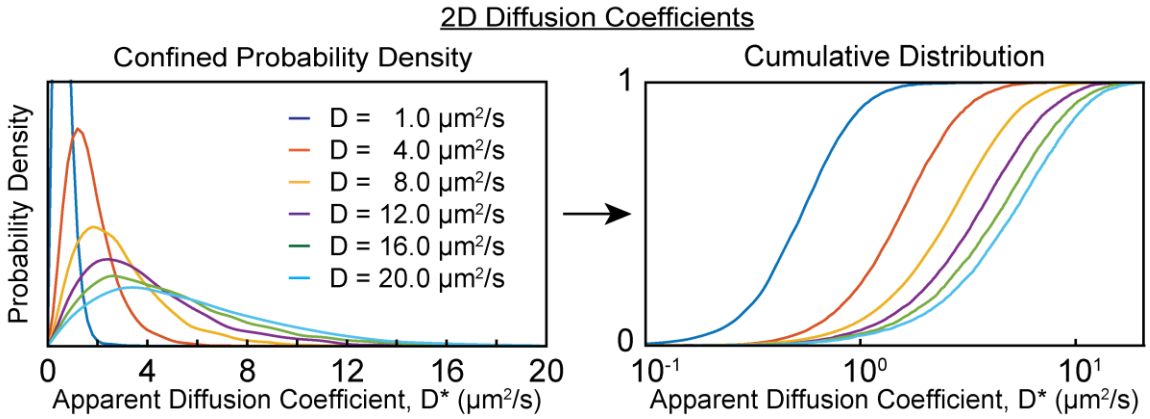

Fig. 5.7. Examples of the apparent diffusion coefficient distribution library for 2D tracking.

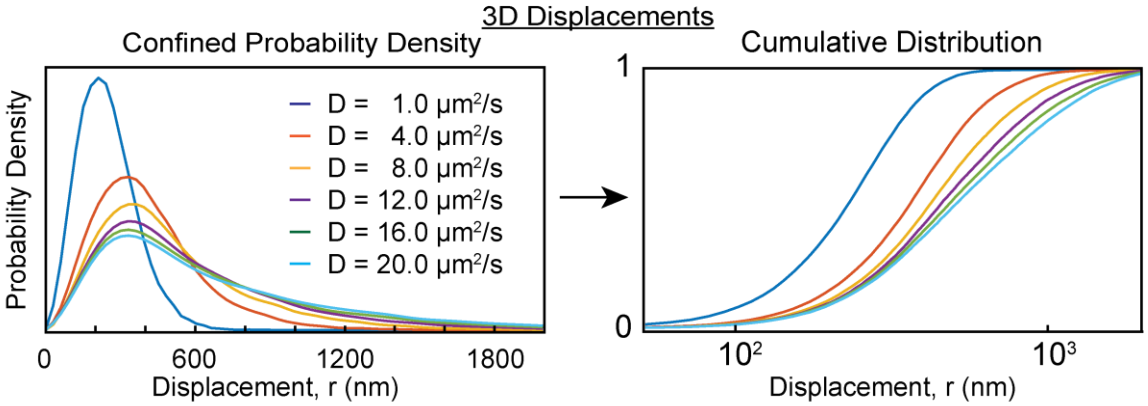

Fig. 5.8. Examples of the displacement distribution library for 3D displacements.

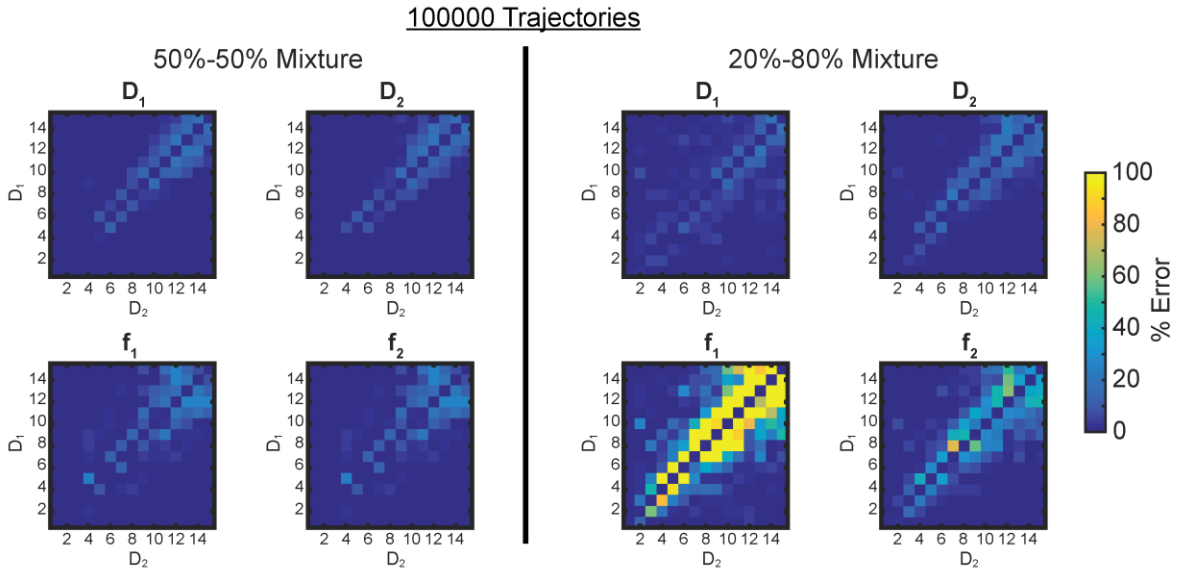

Fig. 5.9. 3D apparent diffusion coefficient distribution fitting of 2-state populations with 100000 trajectories for 50%-50% population fraction mixtures (left) or 20%-80% population fraction mixtures (right). The relative errors decrease compared to **Fig 5.4a** when the distributions are better sampled with more trajectories.

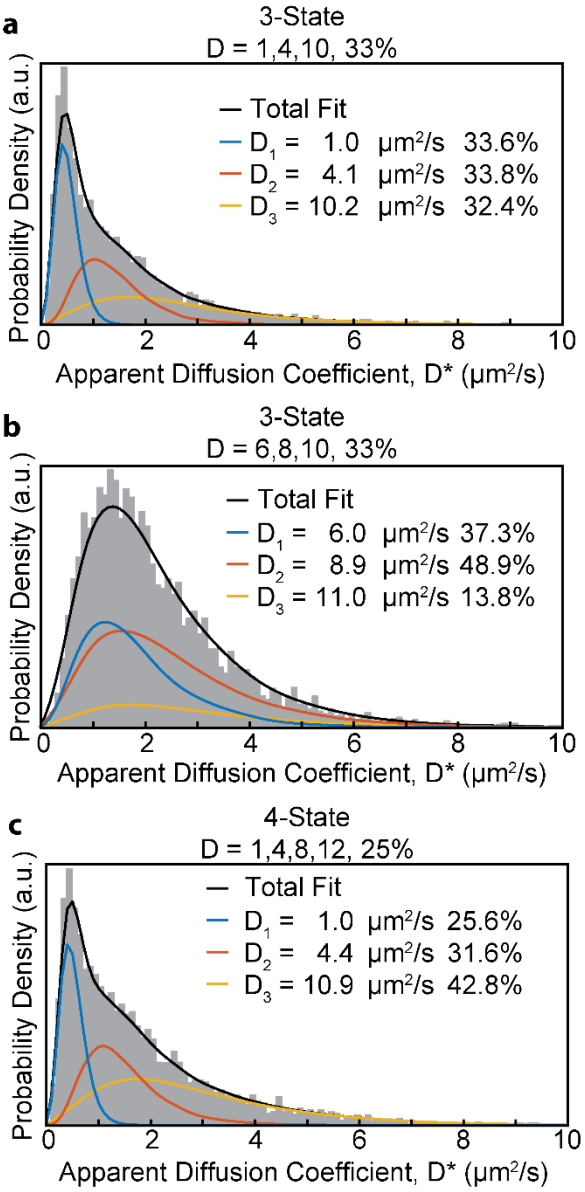

Fig. 5.10. Multiple diffusive state fitting examples. (a,b) 3-state distributions were simulated with equal population fractions of 33% each. In (a) the diffusion coefficients are well separated, and both the diffusion coefficients and respective population fractions were accurately fit. However, in (b) the diffusion coefficients were close in value, leading to increased error in the fitting parameters. (c) A 4-state distribution was simulated with equal population fractions of 25% each. The fitting algorithm determined that the best fit was

with a 3-state mixture. In this case, the fastest two diffusive states were combined into one state with an intermediate diffusion coefficient.

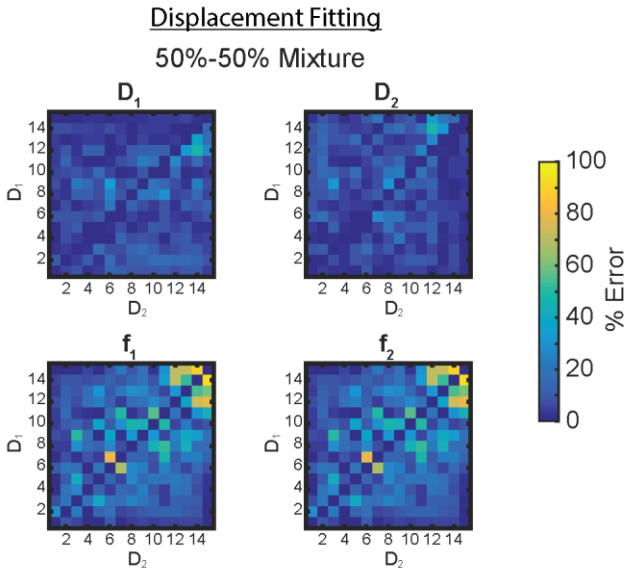

Fig. 5.11. 3D displacement distribution fitting of 2-state populations.

Table 5.1. List of strains and plasmids.

Strain Name	Characteristics	Ref
AG0003	pAH12-eYFP	(119)
AG0006	pBAD-mEos3.2	This work

Chapter 6: Single-molecule tracking of Sorting Platform Proteins

6.1 Introduction

Our previous work on the T3SS detailed in Chapter 4 proposed cytosolic complex formation of sorting platform proteins through high-throughput 3D single-molecule imaging (119). Our results suggested that functional regulation of the T3SS may occur through formation of distinct cytosolic complexes prior to association with the membrane-embedded injectisome. By comparing the diffusive behavior of SctQ and SctL in different genetic backgrounds, we were able to construct an initial model for cytosolic sorting platform complex composition.

Here we present an expansion to this work, however we note that the results presented in this chapter are unpublished as of the writing of this dissertation. We observe the diffusive properties of the sorting platform proteins SctQ, SctL, and SctN in a variety of additional genetic backgrounds to detect the resulting differences in behavior. We show that all three proteins diffuse within the bacterial cytosol as components of different sized protein complexes. Furthermore, their diffusive properties are dependent on the secretion state of the system, and exhibit greater diffusion rates (and therefore smaller complexes) on average under secreting conditions. Our results further add to a body of work suggesting that T3SS regulation may occur through a dynamic network of cytosolic complex formation, away from the membrane-embedded injectisome.

6.2 Experimental Procedures

6.2.1 Bacterial Strains and Plasmids

Yersinia enterocolitica strains were generated by allelic exchange as previously described (22, 155). Mutator plasmids harboring 250-500 bp flanking regions, the coding sequences of eYFP, and a glycine-rich 13 amino acid linker between the fluorescent protein and the target protein were introduced into *E. coli* SM10 λpir for conjugation with *Y. enterocolitica* pIML421asd (35). After sucrose counter-selection for the second allelic exchange event, fluorescent *Y. enterocolitica* were analyzed by PCR to confirm target insertion. The pBAD plasmids containing eYFP-SctN and eYFP-SctL were obtained from SynBio Technologies, and were transformed into the pYV- *Y. enterocolitica* strains through electroporation as described in Section 4.3.2. A list of all strains and plasmids can be found in **Table 6.3**.

6.2.2 Cell Culture

Y. enterocolitica cultures were prepared for imaging under secreting conditions as described in Section 4.3.2.

6.2.3 Super-resolution Fluorescence Imaging

Experiments were performed on a custom-built dual-color inverted fluorescence microscope as described in section 4.3.4.

6.2.4 Data Analysis

Raw image processing and analysis was carried out as described in section 3.1. Single molecule localizations were assigned to individual cells as described in section 3.2.1. Analysis of high density regions of localizations was carried out as described in section 3.2.2. Single-Molecule Tracking was performed as described in section 3.3.1. To resolve the unconfined diffusion coefficients of predominant molecular complexes in living cells based on the experimentally measured distribution of apparent diffusion coefficients, we performed Monte Carlo simulations of confined Brownian motion as described in section 3.3.2. Experimental distributions of apparent diffusion coefficients were fit using a linear combination of simulated distributions as described in section 3.3.3. Confidence intervals for all fitting parameters were obtained by bootstrapping and are reported in **Table 6.1**. The radial distributions in **Fig. 6.8** were created as described in section 3.2.2.

6.3 Results and Discussion

6.3.1 SctQ exhibits similar diffusive states in the absence of the inner membrane protein SctD compared to the wild-type background

We previously reported that eYFP-SctQ can exist in three different cytosolic diffusive states in the wild-type background, with D = 1.1, 4.0, and 13.9 $\mu m^2/s$ and corresponding population fractions of 17%, 36%, and 22% (119). We assigned these states to a hetero-oligomer containing SctQ and other T3SS proteins, a homo-oligomer of

SctQ:SctQ$_C$, and monomeric SctQ, respectively (119). Additionally, there is a stationary component ($D < 0.5$ μm^2/s) with population fraction of 24%, which we assign to the injectisome-bound fraction of SctQ.

Here we observe the diffusive behavior of eYFP-SctQ in a strain lacking the inner membrane ring protein SctD. SctD serves as the membrane-embedded attachment site for the sorting platform proteins, most likely through interaction with SctK (38, 58). Therefore, the sorting platform proteins and complexes should not associate with the membrane-embedded machine and the T3SS will not secrete proteins. When we tracked SctQ in a mutant strain lacking SctD, we observed similar diffusive states as in the wild-type background, with unconfined diffusion coefficients of D = 1.3, 3.9, and 13.5 μm^2/s (**Fig 6.1a, Table 6.1)**. However, in this case the relative population fractions of the diffusive states were shifted to 36%, 44%, and 8%, respectively. Thus, the majority of SctQ has shifted towards the diffusive states with D ~ 1 and 4 μm^2/s. In addition, the stationary component decreased by half, to 12%. Nevertheless, we do not observe dense clustering of SctQ localizations (**Fig 6.7b**) or a higher prevalence of stationary trajectories near the membrane in contrast to WT data sets (**Fig. 6.8b**). We would expect all diffusive states to increase in relative population fraction, since SctQ can no longer associate with the T3SS through sorting platform docking with SctD. However, the decrease in the relative population fraction for the fastest diffusive state, which we assign as monomeric SctQ, is somewhat unexpected. We speculate that this may arise because there is no longer molecular turnover of injectisome bound SctQ, as has been observed for secreting T3SSs (48). This molecular turnover may play a part in dissociation of monomeric SctQ from other sorting platform homo- or hetero-oligomeric complexes. The T3SS does not secrete

in the absence of SctD, so SctQ may essentially become 'stuck' as part of the larger complexes observed with D ~1 and 4 μm^2/s in both the wild-type and ΔSctD backgrounds.

We observe similar results to the ΔSctD background in a strain lacking the ATPase SctN, which also eliminates secretion of effector proteins. In addition to a stationary component of 12%, we obtain diffusive states of D = 1.0, 3.1, and 12.0 μm^2/s with population fractions of 36%, 44%, and 8%, respectively (**Fig 6.1b**). As was the case for the ΔSctD background, in the ΔSctN background diffusion shifts away from the assigned stationary and monomeric protein states towards the middle diffusive states. We do note, however, that there is a change in the diffusive state of 3.9 μm^2/s observed in the wild-type background to 3.1 μm^2/s in the ΔSctN background. It is possible that this state is slower compared to wild-type because SctQ associates with SctL at a higher rate, due to lack of competition with SctN. We also observed a diffusive state at D = 1.0 μm^2/s. Previously, in our model, we assigned the D = 1.0 μm^2/s diffusive state to a complex including SctQ, $SctQ_C$, SctL, and possibly SctK and SctN. As this state persists in the absence of SctN, SctN may not be a component of this large molecular weight complex. It is also plausible, due to the cradle-like structure of the T3SS sorting platform, the absence of SctN may not affect the diffusion of this large molecular weight complex as SctN sits at the center of the cradle, and does not increase the hydrodynamic radius of the complex (i.e. a larger hydrodynamic radius results in slower diffusion).

Interestingly, we observe low levels of eYFP-SctQ localization clustering in the ΔSctN mutant (**Fig. 6.7c**). Additionally, we observe a pronounced shift towards the membrane in the radial distribution of stationary trajectories (**Fig. 6.8c**). These results

demonstrate that SctQ, and possibly the rest of the sorting platform, is still able to associate with the membrane-embedded injectisome in the absence of the ATPase SctN. This interpretation is consistent with cryo-ET experiments showing decreased levels of assembled sorting platform proteins in the absence of the Salmonella T3SS ATPase InvC (38).

6.3.2 SctQ forms oligomeric complexes in the absence of $SctQ_c$

We have previously observed a diffusive state of $D \sim 4$ μm^2/s for eYFP-SctQ in both the *Y. enterocolitica* wild-type and pYV- (cells lacking all other T3SS components) backgrounds (119). However, in the absence of $SctQ_c$ the C-terminal fragment of SctQ, we no longer observed the D ~ 4 μm^2/s state for eYFP-$SctQ_{M218A}$ in the pYV- background (mutation of the internal translation initiation site in the *sctQ* coding sequence (M218A) results in a secretion-deficient phenotype (48, 54)). Instead, a previously unobserved state at D ~ 6.8 μm^2/s was present, leading us to conclude that the D ~ 6.8 μm^2/s state corresponds to an homo-oligomeric SctQ complex while the D ~ 4 μm^2/s state observed in the presence of the C-terminal fragment corresponds to an oligomeric SctQ:$SctQ_C$ complex (119).

Here we have observed the diffusive behavior of eYFP-$SctQ_{M218A}$ in the wild-type background (**Fig 6.2, Table 6.1**). Consistent with our experiment in the pYV- background, there is no longer a diffusive state at D ~ 4 μm^2/s. The fastest state at 5.8 μm^2/s may correspond to some homo-oligomeric SctQ complex similar to the results in the pYV- background. The D = 2.3 μm^2/s state is reduced in speed compared to the D ~ 4 μm^2/s state,

suggesting this is a larger oligomer than the SctQ:$SctQ_C$ complex, and indicate that SctQ can still associate with other sorting platform proteins in the absence of $SctQ_C$. Additionally, we do not observe association of eYFP-$SctQ_{M218A}$ with the membrane-embedded injectisome (**Fig 6.7a and 6.8a**), consistent with the fact that this strain is secretion deficient (48, 54).

6.3.3 SctN exists in at least 2 diffusive states in the cytosol

Localizations obtained for the ATPase SctN in the wild-type background show heavy clustering near the bacterial membrane (**Fig. 6.7g and 6.8g**). When we tracked eYFP-SctN we found that a majority of trajectories (55%) were in a stationary state. These results together suggest that SctN is primarily associated with the T3SS, with a smaller fraction diffusing within the cytosol. In addition to the large stationary population, we found that eYFP-SctN existed in three diffusive states with D = 1.0, 2.6, and 12.4 $\mu m^2/s$ with population fractions of 16%, 21%, and 8% respectively (**Fig. 3a, Table 6.1**). As the typical error for fitting of the diffusive state parameters is ~10%, we are cautious to place importance of any diffusive state with a population <10%, such as the state at D = 12.4 $\mu m^2/s$. Therefore, here we will focus on the two diffusive states at D = 1.0 and 2.6 $\mu m^2/s$. Previously we proposed that the D = 1.0 $\mu m^2/s$ state observed for eYFP-SctQ corresponded to a large diffusive complex containing SctQ, $SctQ_c$, SctL, and possibly SctK and SctN (119). The diffusive state seen here at D = 1.0 $\mu m^2/s$ for SctN is in good agreement with this hypothesis. In addition to this state, however, we see a state at 2.6 $\mu m^2/s$. We have not previously observed a diffusive state at this rate for SctQ, suggesting a new diffusive

complex. If SctQ is not part of this complex, it is unlikely SctK would be found in a complex with SctN based on their locations within the sorting platform. This limits potential candidates of the D = 2.6 μm^2/s state to a homo-oligomeric complex of SctN or a hetero-oligomeric complex of SctN, SctL, and potentially effector proteins. In fact, SctN and SctL have been shown to form hetero-trimers of $SctL_2$-SctN *in vitro* (163, 183).

We performed single-molecule tracking on eYFP-SctN in a strain lacking the inner membrane protein SctD. In the ΔSctD background we obtained results with similar diffusion coefficients as eYFP-SctN in the wild-type background, with D = 1.0, 2.3, and 15.0 μm^2/s (**Fig. 6.3b, Table 6.1**). However, the relative population fractions have shifted to 27%, 52%, and 5% respectively (from 16%, 21%, and 8%). Additionally, the stationary population is largely reduced, from 56% to 15%. These results mirror eYFP-SctQ in the wild-type and ΔSctD backgrounds, where we also see the same diffusive states present in both backgrounds, with the relative population fractions distributed differently. The complexes observed here can therefore assemble spontaneously in the cytosol prior to association with the membrane-embedded injectisome.

Finally, we observed eYFP-SctN in the pYV- background. In this strain we observed two different states for eYFP-SctN, with diffusion coefficients of D = 1.4 and 4.3 μm^2/s, with relative population fractions of 37% and 50%, respectively (**Fig. 6.3c, Table 6.1**). As we observe in most data sets, we also observe a small stationary population, however this fraction is not localized near the membrane (**Fig. 6.8i**). Assuming SctN does not associate with non-T3SS proteins, any observed diffusive states must correspond to homo-oligomeric complexes or monomeric SctN, as no other T3SS proteins are present. Importantly, we no longer observe the D = 2.6 μm^2/s state, suggesting that this state

requires the presence of other T3SS proteins, most likely SctL. SctN forms a hexameric structure *in vitro* (184), and the fully assembled injectisome was estimated to contain six SctN subunits *in situ* by fluorescence microscopy (23). Therefore, we posit that the slowest diffusive state corresponds to a homo-hexameric complex of SctN. The slower diffusive state at 4.3 $\mu m^2/s$ should also correspond to a homo-oligomeric complex of SctN, as it is much slower than monomeric protein. In addition to hexamers, soluble SctN has been shown to form homo-trimers (185), which may explain this diffusive state.

6.3.4 SctL diffuses as part of a cytosolic complex

Previously we observed SctL fluorescently tagged with the fluorescent protein PAmCherry1 (119). For consistency between all experiments, and slight differences in behavior between PAmCherry1 and eYFP, we repeated our SctL experiments with an eYFP label. Similar to SctN, localizations obtained for eYFP-SctL exhibited heavy clustering in the wild-type background near the bacterial membrane (**Fig. 6.7d and 6.8d**). We performed single-molecule tracking on eYFP-SctL in the wild-type background, and found most molecules to be in a stationary state (71%). Like SctN, SctL primarily exists as a T3SS associated component. We found that the remaining population exhibits three diffusive states at D = 1.0, 2.6, and 15.0 $\mu m^2/s$ with population fractions of 9%, 14%, and 7% respectively (**Fig. 4a, Table 6.1**). Notably, we observe a state at 2.6 $\mu m^2/s$, which was also observed for eYFP-SctN in the wild-type background, suggesting co-diffusion between the two proteins. As stated in the previous section, we are cautions to assign importance to the other low-abundance states (<10%) due to the error in obtaining the

relevant parameters. Nonetheless, the diffusive state at D = 1.0 μm^2/s is in good agreement with the diffusive state at D ~ 1.0 μm^2/s for SctQ and SctN in the wild-type background, suggesting a large molecular complex composed of SctQ, SctL, and SctN.

Similar to SctQ and SctN, we performed an initial single-molecule tracking experiment in the ΔSctD mutant for eYFP-SctL. The diffusive states that we obtain by fitting the distribution of apparent diffusion coefficients is found in **Fig. 4b and Table 6.1**. However, these states were extracted from a data set with the fewest single-molecule trajectories we have obtained to date from a single experiment (~1500). As we have shown previously, the diffusive state fitting is more reliable for higher numbers of trajectories (186). Therefore, we will not attempt to interpret these diffusive states at this time. Whether these states are real or an artifact of fitting a distribution of few trajectories is yet to be determined, and will require additional experiments. Nonetheless, the overall mean apparent diffusion coefficient can provide valuable information, and is not prone to error in fitting of the distributions. The mean apparent diffusion coefficient (D* > 0.15 μm^2/s) for non-stationary eYFP-SctL in the ΔSctD background is smaller than in the wild-type background (0.85 and 1.46 μm^2/s, respectively) (**Table 6.2**). Assuming our hypothesis that dynamic sorting platform complexes play a role in T3SS is correct, we would expect this result. Interestingly, in the pYV- background, SctL follows the same trend as SctQ and SctN of faster diffusion than in the ΔSctD mutant, at 1.24 μm^2/s (**Table 6.2**). The fact that we observe slower diffusion in the ΔSctD background suggests that SctL is diffusing as part of a complex with other T3SS components.

6.3.5 Sorting platform protein dynamics depend on T3SS secretion

If we consider only the mean apparent diffusion coefficients for the data sets we've obtained for SctQ, SctL, and SctN, it is apparent that SctQ is the most dynamic component of the sorting platform. In the wild-type background, the mean apparent diffusion coefficient for SctQ, SctL, and SctN is 1.69, 1.46, and 1.14 $\mu m^2/s$, respectively (**Fig 6.5, Table 6.2**). In the ΔSctD mutant SctQ also exhibits a higher diffusive rate compared to SctL and SctN, with mean apparent diffusion coefficients of 1.15, 0.85, and 0.95 $\mu m^2/s$, respectively. As these proteins are all of comparable size, these results suggest that overall, SctQ is diffusing as part of smaller complexes than SctL and SctN. Importantly, all three proteins shift to slower diffusion (i.e. larger complexes) in the non-secreting ΔSctD mutant. Faster diffusion in the presence of secreting T3SS is consistent with a model in which dynamic exchange of sorting-platform complexes plays a role in secretion. Furthermore, for all three proteins, diffusion is decreased in the ΔSctD mutant compared to the pYV- background (**Fig. 6.5**), indicating association with the other sorting platform proteins to form larger oligomers in the bacterial cytosol.

6.4 Conclusions

A growing body of work suggests that dynamic cytosolic complexes of sorting platform proteins play a role in T3SS function (48, 49, 119). By utilizing 3D single-molecule tracking in live bacterial cells, we have made progress towards elucidating the dynamic network of cytosolic complex formation. In addition to injectisome bound protein,

we have shown that SctQ, SctL, and SctN diffuse within the bacterial cell as part of cytosolic complexes. Taking into account the results from Chapter 4 as well as the new data presented here, we have constructed a model for T3SS sorting platform cytosolic complex formation (**Figure 6.6**). As before, the data are consistent with a model in which cytosolic SctQ undergoes dynamic assembly and disassembly steps to interconvert between at least three distinct molecular species that diffuse at different rates. We assign the fastest, and therefore smallest, state corresponds to SctQ monomers diffusing freely in the cytosol ($D > 10$ μm^2/s). SctQ also self-assembles into oligomeric SctQ:SctQ$_C$ complexes ($D \sim 4$ μm^2/s), which requires the C-terminal fragment SctQ$_C$. This oligomeric SctQ:SctQ$_C$ complex ($D \sim 4$ μm^2/s) does not require any other T3SS sorting platform proteins, as the state also appears the pYV- strain, but does not appear in either the SctL or SctN labeled experiments. We note the possibility that SctQ:SctQ$_C$ complexes contain SctK in wild-type cells, which has been shown to interact with SctQ (43-46). As SctQ is also found in a slower diffusive state at $D = 1$ μm^2/s, we posit that SctQ: SctQ$_C$ complexes associate with SctL, SctN, and possibly SctK to form high molecular weight complexes, as this state is also present in the eYFP-YscL, and eYFP-SctN data sets. The exact composition of the complex is unknown, however it is likely that it may be either an individual sorting platform pod or the entire assembled sorting platform itself. Upon tracking eYFP-SctN, a previously unobserved diffusive state emerged ($D = 2.6$ μm^2/s). As we did not observe this state for eYFP-SctQ, the corresponding complex must not contain SctQ or SctK. However, the fact that this state does not appear for eYFP-SctN in the pYV- strain suggests that this complex is a hetero-oligomer. Likely binding partners in a sub-complex containing SctN include SctL or possibly an effector-chaperone complex. Indeed,

we observe a small fraction of eYFP-SctL diffusing at D = 2.6 μm^2/s in the wild-type strain, suggesting that this complex may be comprised of SctN and SctL. This hypothesis is in good agreement with the fact that SctN and SctL have been shown to form hetero-trimers of $SctL_2$-SctN *in vitro* (163, 183).

While our experiments have provided valuable insight into the dynamic nature of the T3SS sorting platform, it is still unclear how this network of cytosolic interactions could regulate T3SS function. All sorting platform proteins observed here decreased in overall diffusivity in the absence of complete injectisomes, suggesting the proteins essentially become 'stuck' as part of larger complexes, and T3SS function may rely on association and dissociation of smaller complexes with the sorting platform. Such dynamic behavior may play a role in effector protein selection and transport to the membrane-embedded injectisome. Further experimentation on effector protein/chaperones dynamic behavior is necessary to elucidate the role of cytosolic sorting platform complex formation.

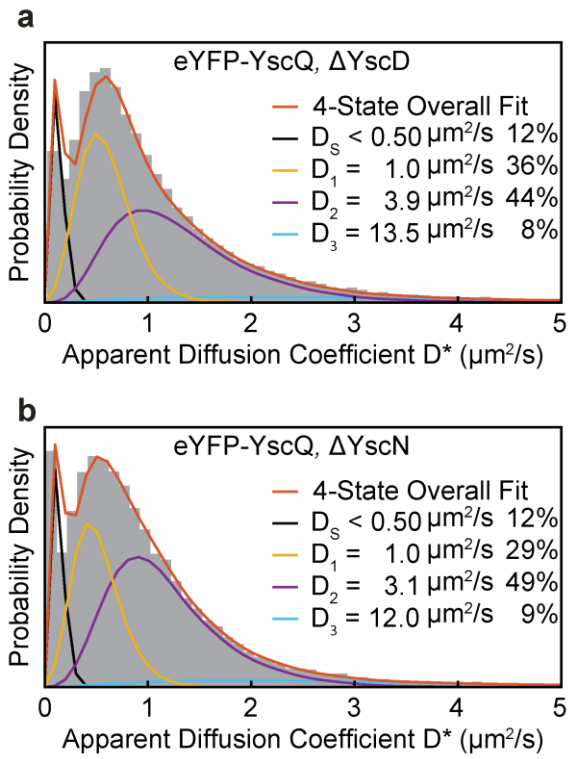

Figure 6.1. Diffusive behavior of eYFP-SctQ in T3SS non-functional strains. Fitting of the apparent diffusion coefficient distribution for eYFP-SctQ in the ΔSctD mutant (a) and ΔSctN mutant (b). Both data sets show depleted stationary and monomeric states compared to eYFP-SctQ in the wild-type strain.

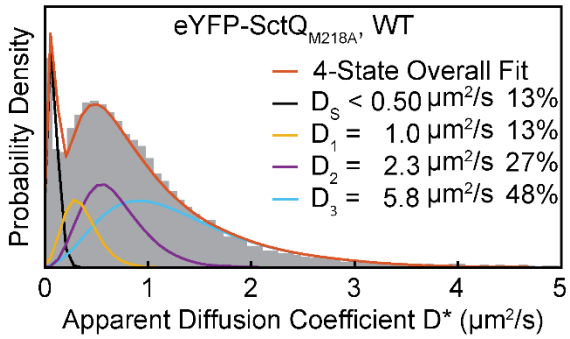

Figure 6.2. Fitting of the apparent diffusion coefficient distribution for eYFP-SctQ$_{M218A}$ mutant. In the absence of the c-terminal fragment SctQ no longer forms a homo-oligomeric complex at $D \sim 4$ µm^2/s.

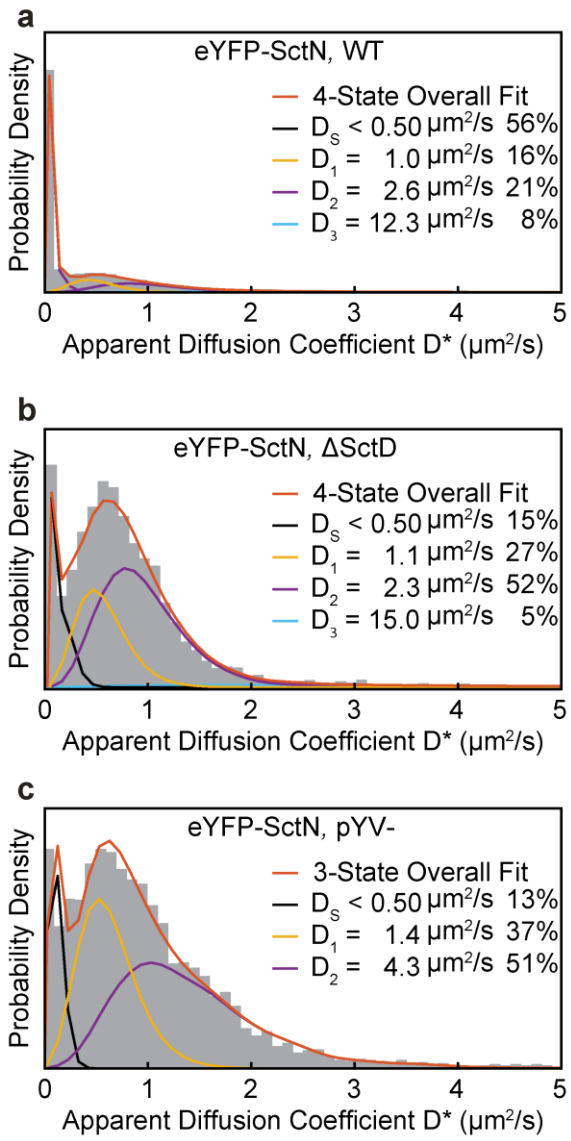

Figure 6.3. Comparison of the diffusive behavior of the ATPase SctN in different genetic backgrounds. Prevalent diffusive states for eYFP-SctN in the wild-type (a), ΔSctD, and ΔSctN strains.

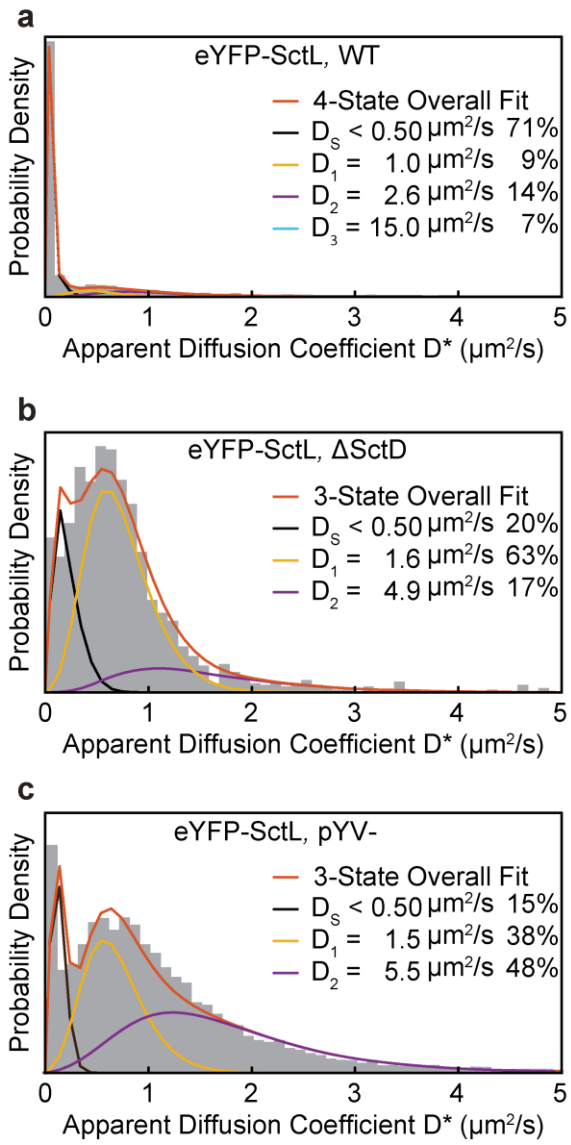

Figure 6.4. Comparison of the diffusive behavior of SctL in different genetic backgrounds. Prevalent diffusive states for eYFP-SctL in the wild-type (a), ΔSctD, and ΔSctN strains.

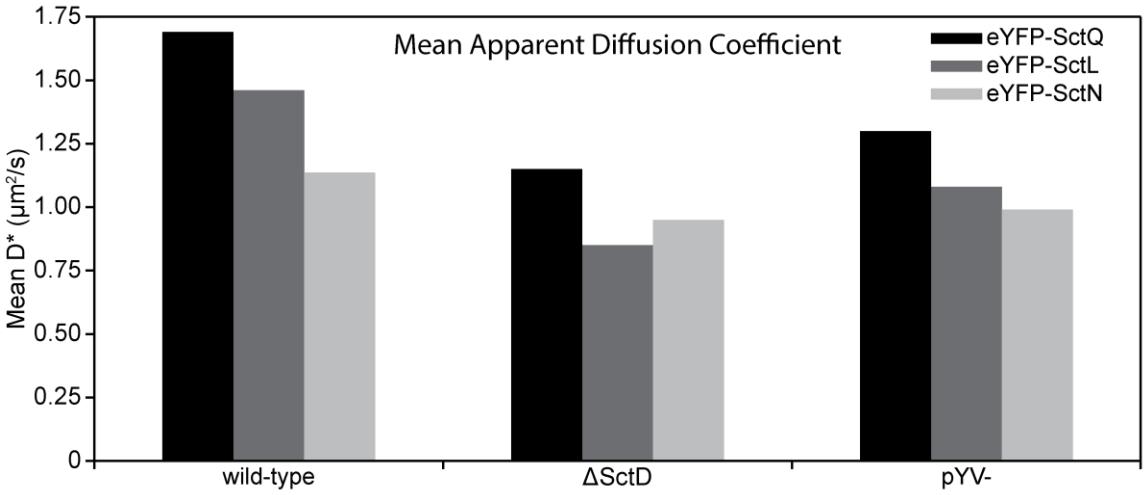

Figure 6.5. Comparison on the mean apparent diffusion coefficient (D*, $\mu m^2/s$) for SctQ, SctL, and SctN in various genetic backgrounds.

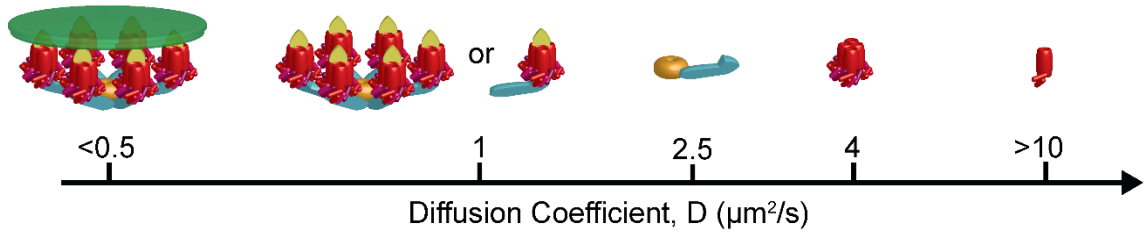

Figure 6.6. Current model of cytosolic assembly of the T3SS sorting platform proteins. Diffusive states: <0.5 μm^2/s – T3SS bound protein, 1 μm^2/s – individual pods of SctK,Q,L and possibly N or fully assembled sorting platforms, 2.5 μm^2/s – hetero-oligomer of SctN,SctL, 4 μm^2/s – homo-oligomer of SctQ:SctQ$_c$, >10 μm^2/s – monomeric protein.

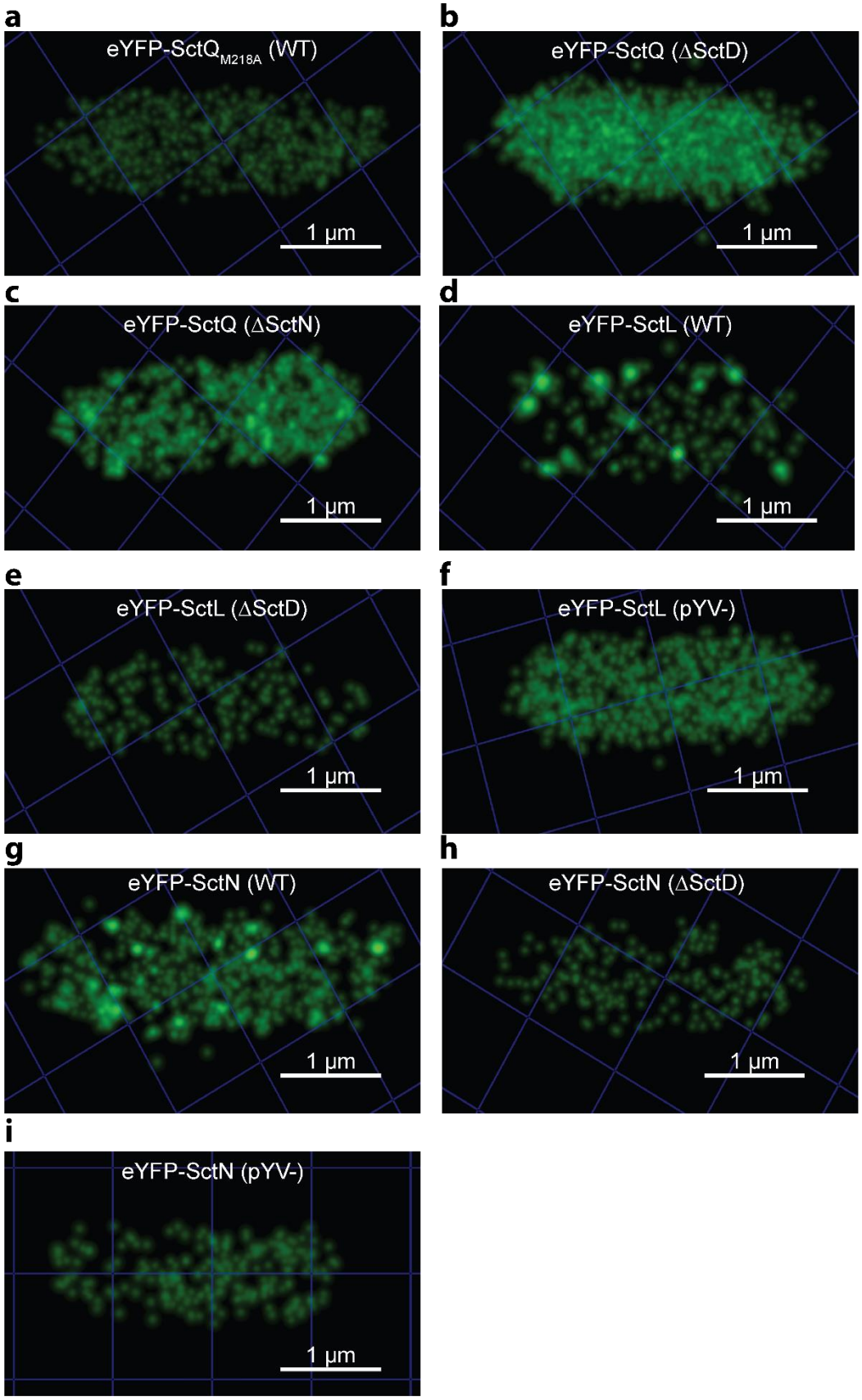
a
eYFP-SctQ$_{M218A}$ (WT)
1 µm
b
eYFP-SctQ (ΔSctD)
1 µm
c
eYFP-SctQ (ΔSctN)
1 µm
d
eYFP-SctL (WT)
1 µm
e
eYFP-SctL (ΔSctD)
1 µm
f
eYFP-SctL (pYV-)
1 µm
g
eYFP-SctN (WT)
1 µm
h
eYFP-SctN (ΔSctD)
1 µm
i
eYFP-SctN (pYV-)
1 µm

Figure 6.7. POVray renderings of representative cells for each data set. (a) eYFP-$SctQ_{M218A}$ (b) eYFP-SctQ, ΔSctD (c) eYFP-SctQ, ΔSctN (d) eYFP-YscL, WT (e) eYFP-SctL, ΔSctD (f) eYFP-SctL, ΔSctN (g) eYFP-YscN, WT (h) eYFP-SctN, ΔSctD (i) eYFP-SctN, ΔSctN

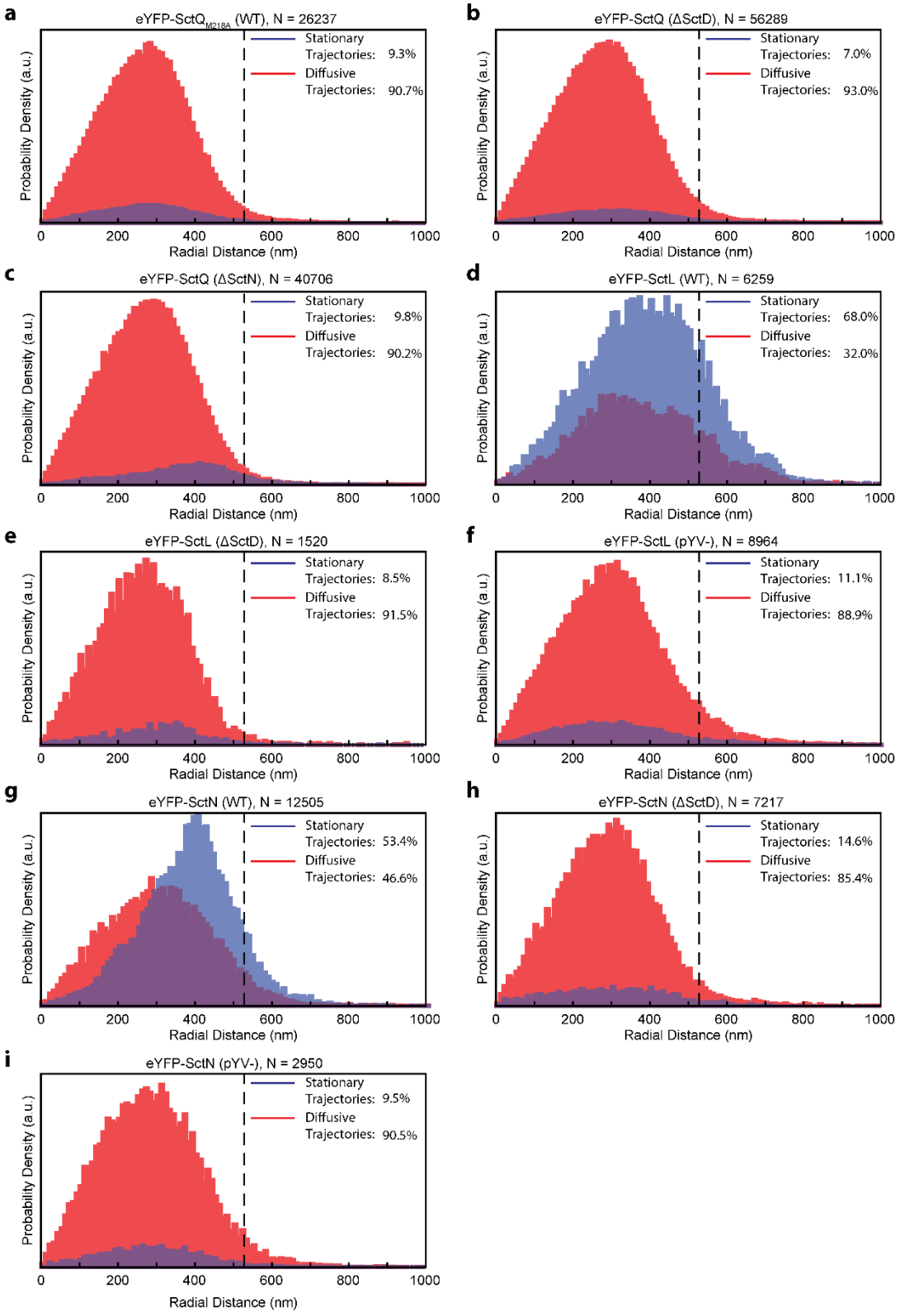
a
eYFP-SctQ$_{M218A}$ (WT), N = 26237
Stationary Trajectories: 9.3%
Diffusive Trajectories: 90.7%
b
eYFP-SctQ (ΔSctD), N = 56289
Stationary Trajectories: 7.0%
Diffusive Trajectories: 93.0%
c
eYFP-SctQ (ΔSctN), N = 40706
Stationary Trajectories: 9.8%
Diffusive Trajectories: 90.2%
d
eYFP-SctL (WT), N = 6259
Stationary Trajectories: 68.0%
Diffusive Trajectories: 32.0%
e
eYFP-SctL (ΔSctD), N = 1520
Stationary Trajectories: 8.5%
Diffusive Trajectories: 91.5%
f
eYFP-SctL (pYV-), N = 8964
Stationary Trajectories: 11.1%
Diffusive Trajectories: 88.9%
g
eYFP-SctN (WT), N = 12505
Stationary Trajectories: 53.4%
Diffusive Trajectories: 46.6%
h
eYFP-SctN (ΔSctD), N = 7217
Stationary Trajectories: 14.6%
Diffusive Trajectories: 85.4%
i
eYFP-SctN (pYV-), N = 2950
Stationary Trajectories: 9.5%
Diffusive Trajectories: 90.5%
Probability Density (a.u.)
Radial Distance (nm)
0
200
400
600
800
1000

Figure 6.8. Radial distribution plots for stationary ($D^* < 0.15$ μm^2/s) vs. diffusive ($D^* > 0.15$ μm^2/s) trajectory localizations for each data set. (a) eYFP-SctQ$_{M218A}$ (b) eYFP-SctQ, ΔSctD (c) eYFP-SctQ, ΔSctN (d) eYFP-YscL, WT (e) eYFP-SctL, ΔSctD (f) eYFP-SctL, ΔSctN (g) eYFP-YscN, WT (h) eYFP-SctN, ΔSctD (i) eYFP-SctN, ΔSctN

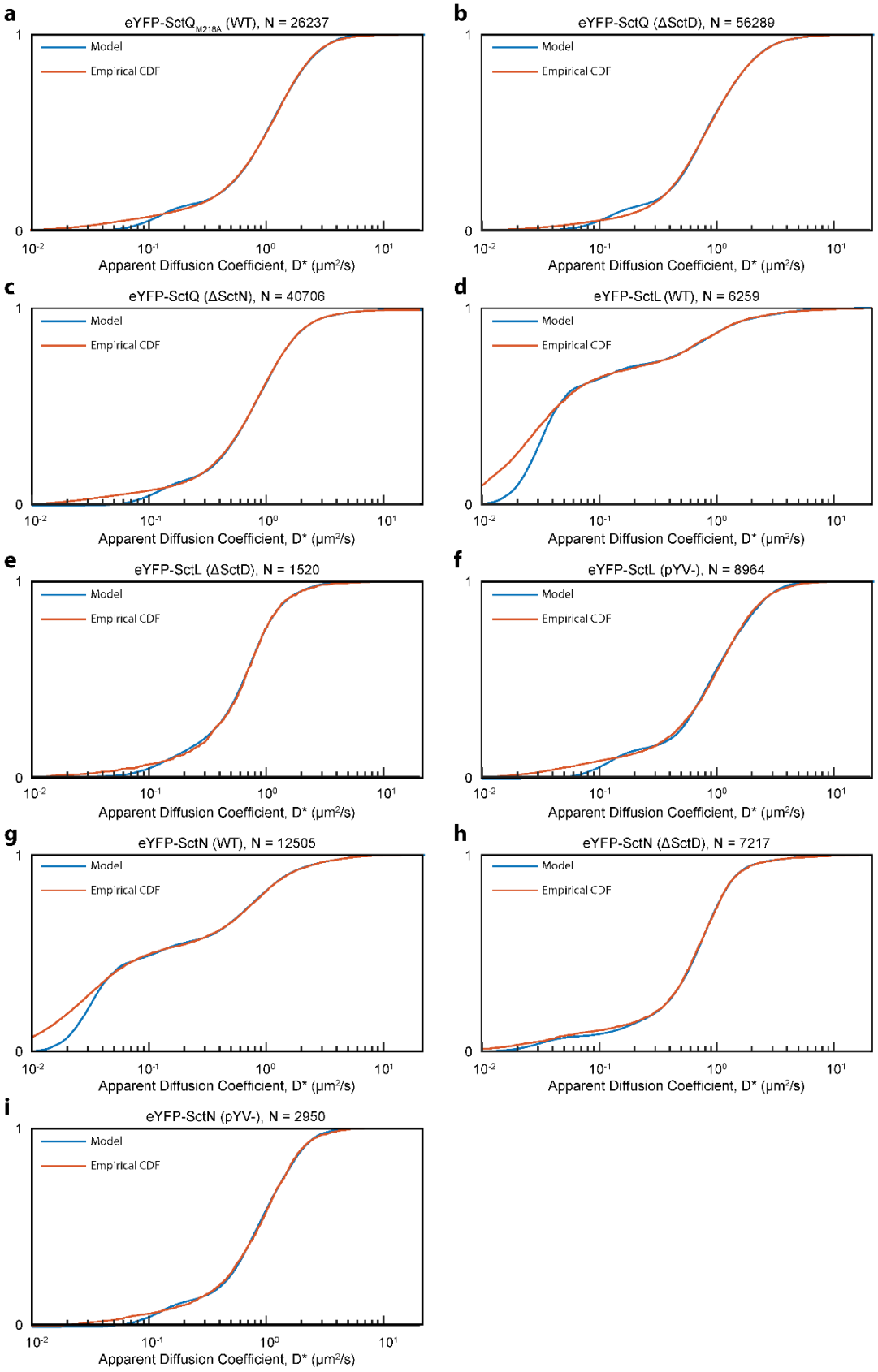
a
eYFP-SctQ$_{M218A}$ (WT), N = 26237
b
eYFP-SctQ (ΔSctD), N = 56289
c
eYFP-SctQ (ΔSctN), N = 40706
d
eYFP-SctL (WT), N = 6259
e
eYFP-SctL (ΔSctD), N = 1520
f
eYFP-SctL (pYV-), N = 8964
g
eYFP-SctN (WT), N = 12505
h
eYFP-SctN (ΔSctD), N = 7217
i
eYFP-SctN (pYV-), N = 2950
Model
Empirical CDF
Apparent Diffusion Coefficient, D* (μm²/s)

Figure 6.9. Cumulative distribution functions (CDF) for apparent diffusion coefficient distribution fitting. (a) eYFP-SctQ$_{M218A}$ (b) eYFP-SctQ, ΔSctD (c) eYFP-SctQ, ΔSctN (d) eYFP-YscL, WT (e) eYFP-SctL, ΔSctD (f) eYFP-SctL, ΔSctN (g) eYFP-YscN, WT (h) eYFP-SctN, ΔSctD (i) eYFP-SctN, ΔSctN

Table 6.1. Fitted diffusion coefficients and relative population fractions.

eYFP-SctQ$_{M218A}$ WT		**eYFP-SctQ ΔSctD**		**eYFP-SctQ ΔSctN**	
(%)	*D* (μm^2/s)	%	*D* (μm^2/s)	%	*D* (μm^2/s)
13	<0.50	12	<0.50	12	<0.50
13 (±1)	1.0 (±0.1)	36 (±4)	1.3 (±0.1)	29 (±1)	1.0 (±0.1)
27 (±4)	2.3 (±0.2)	44 (±3)	3.9 (±0.4)	49 (±2)	3.1 (±0.1)
48 (±4)	5.8 (±0.2)	8 (±2)	13.5 (±0.8)	9 (±1)	12.0 (±0.2)
eYFP-SctL WT		**eYFP-SctL ΔSctD**		**eYFP-SctL pYV$^-$**	
%	*D* (μm^2/s)	%	*D* (μm^2/s)	%	*D* (μm^2/s)
71	<0.50	20	<0.50	15	<0.50
9 (±1)	1.0 (±0.2)	63 (±5)	1.6 (±0.1)	38 (±2)	1.5 (±0.1)
14 (±3)	2.6 (±0.3)	17 (±5)	4.9 (±0.6)	48 (3)	5.5 (±0.2)
7 (±3)	15.0 (±0.2)				
eYFP-SctN WT		**eYFP-SctN ΔSctD**		**eYFP-SctN pYV$^-$**	
%	*D* (μm^2/s)	%	*D* (μm^2/s)	%	*D* (μm^2/s)
56	<0.50	15	<0.50	13	<0.50
16 (±2)	1.0 (±0.1)	27 (±4)	1.1 (±0.1)	37 (±5)	1.4 (±0.1)
21 (±1)	2.6 (±0.2)	52 (±4)	2.3 (±0.1)	50 (±5)	4.3 (±0.3)
8 (±1)	12.4 (±1.0)	5 (±1)	15.0 (±0.5)		

Table 6.2: Mean apparent diffusion coefficients (D* > 0.15 μm^2/s) for all data sets.

	Mean D* (μm^2/s)
eYFP-SctQ$_{M218A}$, WT	1.31
eYFP-SctQ, ΔSctD	1.15
eYFP-SctQ, ΔSctN	1.10
eYFP-SctL, WT	1.46
eYFP-SctL, ΔSctD	0.85
eYFP-SctL, pYV-	1.24
eYFP-SctN, WT	1.14
eYFP-SctN, ΔSctD	0.95
eYFP-SctN, pYV-	1.08

Table 6.3. List of strains and plasmids.

Strain Name	pYV Background	Characteristics	Ref
Wild-type	IML421	pYV40 *yopO*$_{\Delta 2\text{-}427}$ *yopE*$_{21}$ *yopH*$_{\Delta 1\text{-}352}$ *yopM*$_{23}$ *yopP*$_{23}$ *yopT*$_{135}$ Δ*asd*	(35)
pYV-	--	Lacking pYV40 plasmid	
AG0007	Wild-type	*eyfp-yscQ*$_{M218A}$	This work
AG0008	Wild-type	*eyfp-yscQ*, ΔyscN	This work
AG0009	Wild-type	*eyfp-yscQ*, ΔyscD	This work
AG0010	Wild-type	*eyfp-yscL*	This work
AG0011	Wild-type	*eyfp-yscL*, ΔyscD	This work
AG0012	Wild-type	*eyfp-yscN*	This work
AG0013	Wild-type	*eyfp-yscN*, ΔyscD	This work
AG0014	pYV-	pBAD-eYFP-YscL	This work
AG0015	pYV-	pBAD-eYFP-YsN	This work

Chapter 7: Conclusions and Future Directions

7.1 Significance

The Type 3 Secretion System is responsible for cell motility and provides a mechanism for bacterial pathogens to infect host cells. This work has focused on the virulence-associated injectisome. While the T3SS is found in many Gram-negative bacterial species, the machinery remains largely conserved between species, making the system an attractive drug target to combat its virulent properties. Despite attempts spanning several decades to understand the functional mechanisms of the system, many questions remain unanswered due to its complex nature and relatively small size. In particular, little is known about the functional importance of the loosely-associated cytosolic component at the inner-membrane interface, called the sorting platform.

Advances in cryo-ET have only recently provided high resolution images of the structural composition of the majority of the system, including the sorting platform (36-40). While much can be inferred about the function of a system by its static structure, any dynamic processes cannot be visualized in a fixed sample. Fluorescence microscopy is a preferred method for visualizing biological samples due to its ability to observe targeted molecules in live cells. Furthermore, the development of super-resolution fluorescence microscopy has provided the ability to observe individual fluorescent emitters with a precision on the nanometer scale. The sub-field of single-molecule tracking has therefore become a valuable tool to study interactions among freely diffusing proteins in living cells. Diffusive state-resolved results are not obtainable with traditional methods that probe for protein interactions, such as Foerster resonance energy transfer (FRET) or fluorescence recovery after photobleaching (FRAP). Single-molecule tracking has been applied to a

large variety of targets, including transcription factors and proteins required for cell wall synthesis(187).

Through super-resolution fluorescence microscopy, specifically single-molecule localization microscopy, this work provided insight into the dynamic behavior of proteins within the T3SS sorting platform. A major effort went into developing a diffusion analysis framework to resolve the prevalent diffusive states of fluorescently labeled proteins in the bacterial cytosol. To accomplish this, a variety of simulations were employed with known parameters to mimic experimental single-molecule tracking data to create, through forward convolution, distributions of apparent diffusion coefficients. Experimental data is then fit with these distributions to resolve diffusion coefficients and determine their relative population fractions of prevalent diffusive states. These states were used to infer the composition of diffusive complexes in the bacterial cytosol. By comparing the diffusive states present for the different sorting platform proteins in various genetic backgrounds, we were able to build a model for cytosolic complex formation.

By quantitatively analyzing large amounts of single-molecule tracking data, we have developed a novel approach for detecting dynamic protein complexes and potentially transient binding interactions in living cells. Recent work has shown that many protein complexes, which were initially regarded as stable structures, actually undergo dynamic subunit exchange (188). For example, subunit exchange has been observed in the bacterial flagellar motor(189-191) and the nuclear pore complex (192). With few modifications, the numerical analysis framework developed here can be adapted for the study of these systems.

7.2 Future Directions

In addition to the sorting platform, future work will also focus on the chaperone and effector proteins to determine the mechanisms of secretion. However, unlike the sorting platform proteins, effector proteins cannot be labeled with fluorescent proteins. Effector proteins must be unfolder prior to secretion through the narrow needle channel, and fluorescent proteins are too stable to be unfolded by the system. Therefore, any attempt to label an effector with a thermodynamically stable fluorescent protein will result in a clogged needle, and therefore a non-functional injectisome. Current attempts to observe effector proteins are limited to non-secreting strains or strains lacking the other T3SS components. It may be possible to label the effector with a fluorescent dye using a labeling strategy such as the Halo and SNAP tags, however there are conflicting reports on whether these can be secreted through the needle complex. A potential solution to this problem would be to utilize an unnatural amino acid labeling strategy that could bind a fluorescent dye, which would be small enough to be secreted. However, this approach is very challenging, as unnatural amino acid labeling strategies involve inserting the unnatural amino acid at all amber stop codon sites that are available on the genome. While this labeling strategy may be acceptable for certain *in vitro* assays, it may not be suitable for live cell fluorescence imaging, which requires high labeling specificity. If these concerns can be managed however, labeling with unnatural amino acids could provide a viable method to observe effector proteins not only in the bacterial cytosol, but in host cells after secretion. Current methods of observing effector proteins after secretion into host cells are limited to methods such as split GFP, where a single beta strand of GFP molecule is fused

to the effector protein in the bacteria, while the rest is expressed in the host cell. When the effector is secreted into the host cell, the two portions combine to produce a functional chromophore observable by fluorescence. The drawback to this method is the relatively long time for the two portions to combine and the GFP chromophore to mature. A labeling strategy, such as unnatural amino acid labeling, to observe the behavior of effector proteins in real-time would provide optimal insight into their function inside host cells.

More information can be obtained about the behavior of an individual molecule as the trajectory length increases. For example, as was shown in Chapter 5, long trajectories can be used to extract information on association and dissociation kinetics. This work utilized fluorescent proteins as markers for target proteins due to their ability to be genetically encoded, therefore ensuring complete specificity. A drawback to fluorescent proteins is their relatively low photon yields compared to other methods such as dye labeling. However, dye labeling can lead to artifacts such as incomplete labeling of all proteins and high levels of background noise due to insufficient washing of unbound dye. Utilizing a labeling strategy with a higher photon yield than fluorescent proteins with high labeling specificity would be desirable and potentially lead to more in depth analysis of the sorting platform proteins behavior.

On the computational front, there are several improvements that can be made to the diffusion analysis framework. Possibly the most important of these is the implementation of methods to account for or extract information on state-switching dynamics. While the foundation was laid out to show that information on state switching dynamics can, in principle, be extracted from single-molecule tracking in a two-state case using TAD

analysis in Chapter 5, a more in depth analysis would be required for more complex situations such as the presence of three or more interchanging diffusive states. Another assumption in the simulated single-molecule trajectories was that they only exhibited Brownian motion, and were not affected by compartmental confinement. It has been suggested that diffusion rates in the dense nucleoid region of the bacterial cell are affected by molecular confinement, however we have not observed this effect.

7.3 Conclusions

The work presented here on T3SS sorting platform proteins has added to a growing body of work suggesting a dynamic interaction network of sorting platform proteins plays a role in the secretion process. A novel diffusion analysis framework was developed to analyze the diffusive behavior of fluorescently labeled proteins. This framework was thoroughly tested to determine its potential applications and limitations. Through application of the framework to single-molecule localization microscopy data obtained on fluorescently labeled sorting platform proteins in live *Y. enterocolitica* cells, we were able to construct a model for cytosolic complex formation of sorting platform complexes. How exactly cytosolic complex formation plays a role in secretion is still unclear, however. Further study of the sorting platform proteins as well as effector and chaperone proteins will provide a more complete look into T3SS function.

References

1. Green, E. R., and J. Mecsas. 2016. Bacterial Secretion Systems: An Overview. Microbiology spectrum 4(1):10.1128/microbiolspec.VMBF-0012-2015.
2. Costa, T. R., C. Felisberto-Rodrigues, A. Meir, M. S. Prevost, A. Redzej, M. Trokter, and G. Waksman. 2015. Secretion systems in Gram-negative bacteria: structural and mechanistic insights. Nat Rev Microbiol 13(6):343-359.
3. Diepold, A., and J. P. Armitage. 2015. Type III secretion systems: the bacterial flagellum and the injectisome. Philosophical transactions of the Royal Society of London. Series B, Biological sciences 370(1679).
4. Hueck, C. J. 1998. Type III Protein Secretion Systems in Bacterial Pathogens of Animals and Plants. Microbiol. Mol. Biol. Rev. 62(2):379-433.
5. Cornelis, G. R. 2006. The type III secretion injectisome. Nat Rev Microbiol 4(11):811-825.
6. Buttner, D. 2012. Protein export according to schedule: architecture, assembly, and regulation of type III secretion systems from plant- and animal-pathogenic bacteria. Microbiol Mol Biol Rev 76(2):262-310.
7. Portaliou, A. G., K. C. Tsolis, M. S. Loos, V. Zorzini, and A. Economou. 2016. Type III Secretion: Building and Operating a Remarkable Nanomachine. Trends Biochem Sci 41(2):175-189.
8. Deng, W., N. C. Marshall, J. L. Rowland, J. M. McCoy, L. J. Worrall, A. S. Santos, N. C. Strynadka, and B. B. Finlay. 2017. Assembly, structure, function and regulation of type III secretion systems. Nat Rev Microbiol.

9. Galán, J. E., and H. Wolf-Watz. 2006. Protein delivery into eukaryotic cells by type III secretion machines. Nature 444:567.

10. Coburn, B., I. Sekirov, and B. B. Finlay. 2007. Type III secretion systems and disease. Clinical microbiology reviews 20(4):535-549.

11. Bai, F., Z. Li, A. Umezawa, N. Terada, and S. Jin. 2018. Bacterial type III secretion system as a protein delivery tool for a broad range of biomedical applications. Biotechnology Advances.

12. Wagner, S., I. Grin, S. Malmsheimer, N. Singh, C. E. Torres-Vargas, and S. Westerhausen. 2018. Bacterial type III secretion systems: a complex device for the delivery of bacterial effector proteins into eukaryotic host cells. FEMS microbiology letters 365(19):fny201.

13. Journet, L., C. Agrain, P. Broz, and G. R. Cornelis. 2003. The Needle Length of Bacterial Injectisomes Is Determined by a Molecular Ruler. Science 302(5651):1757.

14. Diepold, A. 2019. Assembly and Post-assembly Turnover and Dynamics in the Type III Secretion System. Curr Top Microbiol Immunol.

15. Pal, R. R., A. K. Baidya, G. Mamou, S. Bhattacharya, Y. Socol, S. Kobi, N. Katsowich, S. Ben-Yehuda, and I. Rosenshine. 2019. Pathogenic E. coli Extracts Nutrients from Infected Host Cells Utilizing Injectisome Components. Cell 177(3):683-696.e618.

16. Diepold, A., U. Wiesand, and G. R. Cornelis. 2011. The assembly of the export apparatus (YscR,S,T,U,V) of the Yersinia type III secretion apparatus occurs

independently of other structural components and involves the formation of an YscV oligomer. Molecular Microbiology 82(2):502-514.

17. Wagner, S., L. Königsmaier, M. Lara-Tejero, M. Lefebre, T. C. Marlovits, and J. E. Galán. 2010. Organization and coordinated assembly of the type III secretion export apparatus. Proceedings of the National Academy of Sciences 107(41):17745.

18. Kubori, T., A. Sukhan, S.-I. Aizawa, and J. E. Galán. 2000. Molecular characterization and assembly of the needle complex of the Salmonella typhimurium type III protein secretion system. Proceedings of the National Academy of Sciences 97(18):10225.

19. Kimbrough, T. G., and S. I. Miller. 2000. Contribution of Salmonella typhimurium type III secretion components to needle complex formation. Proceedings of the National Academy of Sciences 97(20):11008.

20. Sukhan, A., T. Kubori, J. Wilson, and J. E. Galán. 2001. Genetic Analysis of Assembly of theSalmonella enterica Serovar Typhimurium Type III Secretion-Associated Needle Complex. Journal of Bacteriology 183(4):1159.

21. Ogino, T., R. Ohno, K. Sekiya, A. Kuwae, T. Matsuzawa, T. Nonaka, H. Fukuda, S. Imajoh-Ohmi, and A. Abe. 2006. Assembly of the Type III Secretion Apparatus of Enteropathogenic Escherichia coli. Journal of Bacteriology 188(8):2801.

22. Diepold, A., M. Amstutz, S. Abel, I. Sorg, U. Jenal, and G. R. Cornelis. 2010. Deciphering the assembly of the Yersinia type III secretion injectisome. EMBO J 29(11):1928-1940.

23. Zhang, Y., M. Lara-Tejero, J. Bewersdorf, and J. E. Galan. 2017. Visualization and characterization of individual type III protein secretion machines in live bacteria. Proc Natl Acad Sci U S A 114(23):6098-6103.

24. Poyraz, Ö., H. Schmidt, K. Seidel, F. Delissen, C. Ader, H. Tenenboim, C. Goosmann, B. Laube, A. F. Thünemann, A. Zychlinsky, M. Baldus, A. Lange, C. Griesinger, and M. Kolbe. 2010. Protein refolding is required for assembly of the type three secretion needle. Nature Structural & Molecular Biology 17(7):788-792.

25. Martinez-Argudo, I., and A. J. Blocker. 2010. The Shigella T3SS needle transmits a signal for MxiC release, which controls secretion of effectors. Molecular microbiology 78(6):1365-1378.

26. Fowler, J. M., and R. R. Brubaker. 1994. Physiological basis of the low calcium response in Yersinia pestis. Infection and Immunity 62(12):5234.

27. Forsberg, A., and H. Wolf-Watz. 1988. The virulence protein Yop5 of Yersinia pseudotuberculosis is regulated at transcriptional level by plasmid-plB1 -encoded trans-acting elements controlled by temperature and calcium. Molecular Microbiology 2(1):121-133.

28. Kenjale, R., J. Wilson, S. F. Zenk, S. Saurya, W. L. Picking, W. D. Picking, and A. Blocker. 2005. The Needle Component of the Type III Secreton of Shigella Regulates the Activity of the Secretion Apparatus. Journal of Biological Chemistry 280(52):42929-42937.

29. Torruellas, J., M. W. Jackson, J. W. Pennock, and G. V. Plano. 2005. The Yersinia pestis type III secretion needle plays a role in the regulation of Yop secretion. Molecular Microbiology 57(6):1719-1733.

30. Portaliou, A. G., K. C. Tsolis, M. S. Loos, V. Balabanidou, J. Rayo, A. Tsirigotaki, V. F. Crepin, G. Frankel, C. G. Kalodimos, S. Karamanou, and A. Economou. 2017. Hierarchical protein targeting and secretion is controlled by an affinity switch in the type III secretion system of enteropathogenic Escherichia coli. EMBO J.

31. Kubori, T., Y. Matsushima, D. Nakamura, J. Uralil, M. Lara-Tejero, A. Sukhan, J. E. Galan, and S. Aizawa. 1998. Supramolecular structure of the Salmonella typhimurium type III protein secretion system. Science 280(5363):602-605.

32. Tamano, K., S.-I. Aizawa, E. Katayama, T. Nonaka, S. Imajoh-Ohmi, A. Kuwae, S. Nagai, and C. Sasakawa. 2000. Supramolecular structure of the Shigella type III secretion machinery: the needle part is changeable in length and essential for delivery of effectors. The EMBO Journal 19(15):3876-3887.

33. Blocker, A., N. Jouihri, E. Larquet, P. Gounon, F. Ebel, C. Parsot, P. Sansonetti, and A. Allaoui. 2001. Structure and composition of the Shigella flexneri‘needle complex’, a part of its type III secreton. Molecular Microbiology 39(3):652-663.

34. Schraidt, O., and T. C. Marlovits. 2011. Three-dimensional model of Salmonella's needle complex at subnanometer resolution. Science 331(6021):1192-1195.

35. Kudryashev, M., M. Stenta, S. Schmelz, M. Amstutz, U. Wiesand, D. Castano-Diez, M. T. Degiacomi, S. Munnich, C. K. Bleck, J. Kowal, A. Diepold, D. W.

Heinz, M. Dal Peraro, G. R. Cornelis, and H. Stahlberg. 2013. In situ structural analysis of the Yersinia enterocolitica injectisome. Elife 2:e00792.

36. Nans, A., M. Kudryashev, H. R. Saibil, and R. D. Hayward. 2015. Structure of a bacterial type III secretion system in contact with a host membrane in situ. Nat Commun 6:10114.

37. Makino, F., D. Shen, N. Kajimura, A. Kawamoto, P. Pissaridou, H. Oswin, M. Pain, I. Murillo, K. Namba, and A. J. Blocker. 2016. The Architecture of the Cytoplasmic Region of Type III Secretion Systems. Scientific Reports 6:33341. Article.

38. Hu, B., M. Lara-Tejero, Q. Kong, J. E. Galán, and J. Liu. 2017. In Situ Molecular Architecture of the Salmonella Type III Secretion Machine. Cell 168(6):1065-1074.e1010.

39. Hu, B., D. R. Morado, W. Margolin, J. R. Rohde, O. Arizmendi, W. L. Picking, W. D. Picking, and J. Liu. 2015. Visualization of the type III secretion sorting platform of Shigella flexneri. Proc Natl Acad Sci U S A 112(4):1047-1052.

40. Park, D., M. Lara-Tejero, M. N. Waxham, W. Li, B. Hu, J. E. Galan, and J. Liu. 2018. Visualization of the type III secretion mediated Salmonella-host cell interface using cryo-electron tomography. Elife 7.

41. Lara-Tejero, M., J. Kato, S. Wagner, X. Liu, and J. E. Galan. 2011. A Sorting Platform Determines the Order of Protein Secretion in Bacterial Type III Systems. Science 331(6021):1188-1191.

42. Lara-Tejero, M. 2019. The Type III Secretion System Sorting Platform. Curr Top Microbiol Immunol.

43. Jackson, M. W., and G. V. Plano. 2000. Interactions between type III secretion apparatus components from Yersinia pestis detected using the yeast two-hybrid system. FEMS microbiology letters 186(1):85-90.

44. Jouihri, N., M.-P. Sory, A.-L. Page, P. Gounon, C. Parsot, and A. Allaoui. 2004. MxiK and MxiN interact with the Spa47 ATPase and are required for transit of the needle components MxiH and MxiI, but not of Ipa proteins, through the type III secretion apparatus of Shigella flexneri. Molecular Microbiology 49(3):755-767.

45. Morita-Ishihara, T., M. Ogawa, H. Sagara, M. Yoshida, E. Katayama, and C. Sasakawa. 2006. Shigella Spa33 is an essential C-ring component of type III secretion machinery. The Journal of biological chemistry 281(1):599-607.

46. Spaeth, K. E., Y. S. Chen, and R. H. Valdivia. 2009. The Chlamydia type III secretion system C-ring engages a chaperone-effector protein complex. PLoS Pathog 5(9):e1000579.

47. Johnson, S., and A. Blocker. 2008. Characterization of soluble complexes of the Shigella flexneri type III secretion system ATPase. FEMS Microbiol Lett 286(2):274-278.

48. Diepold, A., M. Kudryashev, N. J. Delalez, R. M. Berry, and J. P. Armitage. 2015. Composition, formation, and regulation of the cytosolic c-ring, a dynamic component of the type III secretion injectisome. PLoS Biol 13(1):e1002039.

49. Diepold, A., E. Sezgin, M. Huseyin, T. Mortimer, C. Eggeling, and J. P. Armitage. 2017. A dynamic and adaptive network of cytosolic interactions governs protein export by the T3SS injectisome. Nat Commun 8:15940.

50. Zhu, S., T. Nishikino, B. Hu, S. Kojima, M. Homma, and J. Liu. 2017. Molecular architecture of the sheathed polar flagellum in Vibrio alginolyticus. Proc Natl Acad Sci U S A.

51. Schuster, S. C., and E. Baeuerlein. 1992. Location of the basal disk and a ringlike cytoplasmic structure, two additional structures of the flagellar apparatus of Wolinella succinogenes. Journal of Bacteriology 174(1):263-268.

52. Francis, N. R., G. E. Sosinsky, D. Thomas, and D. J. DeRosier. 1994. Isolation, Characterization and Structure of Bacterial Flagellar Motors Containing the Switch Complex. J. Mol. Biol. 235(4):1261-1270.

53. Yu, X. J., M. Liu, S. Matthews, and D. W. Holden. 2011. Tandem translation generates a chaperone for the Salmonella type III secretion system protein SsaQ. The Journal of biological chemistry 286(41):36098-36107.

54. Bzymek, K. P., B. Y. Hamaoka, and P. Ghosh. 2012. Two translation products of Yersinia yscQ assemble to form a complex essential to type III secretion. Biochemistry 51(8):1669-1677.

55. McDowell, M. A., J. Marcoux, G. McVicker, S. Johnson, Y. H. Fong, R. Stevens, L. A. Bowman, M. T. Degiacomi, J. Yan, A. Wise, M. E. Friede, J. L. Benesch, J. E. Deane, C. M. Tang, C. V. Robinson, and S. M. Lea. 2016. Characterisation of Shigella Spa33 and Thermotoga FliM/N reveals a new model for C-ring assembly in T3SS. Molecular microbiology 99(4):749-766.

56. Notti, R. Q., S. Bhattacharya, M. Lilic, and C. E. Stebbins. 2015. A common assembly module in injectisome and flagellar type III secretion sorting platforms. Nat Commun 6:7125.

57. Lara-Tejero, M., Z. Qin, B. Hu, C. Butan, J. Liu, and J. E. Galan. 2019. Role of SpaO in the assembly of the sorting platform of a Salmonella type III secretion system. PLoS Pathog 15(1):e1007565.

58. Soto, E., N. Espinosa, M. Díaz-Guerrero, M. O. Gaytán, J. L. Puente, and B. González-Pedrajo. 2017. Functional Characterization of EscK (Orf4), a Sorting Platform Component of the Enteropathogenic Escherichia coli Injectisome. Journal of Bacteriology 199(1):e00538-00516.

59. Blaylock, B., K. E. Riordan, D. M. Missiakas, and O. Schneewind. 2006. Characterization of the Yersinia enterocolitica Type III Secretion ATPase YscN and Its Regulator, YscL. Journal of Bacteriology 188(10):3525.

60. Akeda, Y., and J. E. Galan. 2005. Chaperone release and unfolding of substrates in type III secretion. Nature 437(7060):911-915.

61. Majewski, D. D., L. J. Worrall, C. Hong, C. E. Atkinson, M. Vuckovic, N. Watanabe, Z. Yu, and N. C. J. Strynadka. 2019. Cryo-EM structure of the homohexameric T3SS ATPase-central stalk complex reveals rotary ATPase-like asymmetry. Nature Communications 10(1):626.

62. Evans, L. D. B., and C. Hughes. 2009. Selective binding of virulence type III export chaperones by FliJ escort orthologues InvI and YscO. FEMS Microbiology Letters 293(2):292-297.

63. Diepold, A., and S. Wagner. 2014. Assembly of the bacterial type III secretion machinery. FEMS Microbiol Rev 38(4):802-822.

64. Hell, S. W., and J. Wichmann. 1994. Breaking the diffraction resolution limit by stimulated-emission - stimulated-emission-depletion fluorescence microscopy. Optics Letters 19(11):780-782.

65. Betzig, E., G. H. Patterson, R. Sougrat, O. W. Lindwasser, S. Olenych, J. S. Bonifacino, M. W. Davidson, J. Lippincott-Schwartz, and H. F. Hess. 2006. Imaging intracellular fluorescent proteins at nanometer resolution. Science 313(5793):1642-1645.

66. Klar, T. A., and S. W. Hell. 1999. Subdiffraction resolution in far-field fluorescence microscopy. Optics Letters 24(14):954-956.

67. Hell, S. W. 2007. Far-field optical nanoscopy. Science 316(5828):1153-1158.

68. Dickson, R. M., A. B. Cubitt, R. Y. Tsien, and W. E. Moerner. 1997. On/off blinking and switching behaviour of single molecules of green fluorescent protein. Nature 388(6640):355-358.

69. Moerner, W. E., and D. P. Fromm. 2003. Methods of single-molecule fluorescence spectroscopy and microscopy. Review of Scientific Instruments 74(8):3597-3619. Review.

70. Hofmann, M., C. Eggeling, S. Jakobs, and S. W. Hell. 2005. Breaking the diffraction barrier in fluorescence microscopy at low light intensities by using reversibly photoswitchable proteins. Proc Natl Acad Sci U S A 102(49):17565-17569. Research Support, Non-U.S. Gov't.

71. Gustafsson, M. G. L. 2000. Surpassing the lateral resolution limit by a factor of two using structured illumination microscopy. Journal of Microscopy 198(2):82-87.

72. Gustafsson, M. G. L. 2005. Nonlinear structured-illumination microscopy: Wide-field fluorescence imaging with theoretically unlimited resolution. Proceedings of the National Academy of Sciences 102(37):13081-13086.

73. Thompson, R. E., D. R. Larson, and W. W. Webb. 2002. Precise Nanometer Localization Analysis for Individual Fluorescent Probes. Biophysical Journal 82(5):2775-2783.

74. Rust, M. J., M. Bates, and X. W. Zhuang. 2006. Sub-diffraction-limit imaging by stochastic optical reconstruction microscopy (STORM). Nature Methods 3(10):793-795.

75. Huang, B., W. Q. Wang, M. Bates, and X. W. Zhuang. 2008. Three-dimensional super-resolution imaging by stochastic optical reconstruction microscopy. Science 319(5864):810-813. Article.

76. Dempsey, G. T., J. C. Vaughan, K. H. Chen, M. Bates, and X. Zhuang. 2011. Evaluation of fluorophores for optimal performance in localization-based super-resolution imaging. Nature Methods 8(12):1027-1036.

77. Shroff, H., C. G. Galbraith, J. A. Galbraith, and E. Betzig. 2008. Live-cell photoactivated localization microscopy of nanoscale adhesion dynamics. Nature Methods 5(5):417-423.

78. Lando, D., U. Endesfelder, H. Berger, L. Subramanian, P. D. Dunne, J. McColl, D. Klenerman, A. M. Carr, M. Sauer, R. C. Allshire, M. Heilemann, and E. D. Laue. Quantitative single-molecule microscopy reveals that CENP-ACnp1 deposition occurs during G2 in fission yeast. Open Biology 2(7):120078.

79. Gunzenhäuser, J., N. Olivier, T. Pengo, and S. Manley. 2012. Quantitative Super-Resolution Imaging Reveals Protein Stoichiometry and Nanoscale Morphology of Assembling HIV-Gag Virions. Nano Letters 12(9):4705-4710.

80. Lehmann, M., S. Rocha, B. Mangeat, F. Blanchet, H. Uji-i, J. Hofkens, and V. Piguet. 2011. Quantitative multicolor super-resolution microscopy reveals Tetherin HIV-1 interaction. PLoS Pathogens 7(12):e1002456.

81. Annibale, P., S. Vanni, M. Scarselli, U. Rothlisberger, and A. Radenovic. 2011. Quantitative Photo Activated Localization Microscopy: Unraveling the Effects of Photoblinking. Plos One 6(7):e22678.

82. Ptacin, J. L., A. Gahlmann, G. R. Bowman, A. M. Perez, A. R. von Diezmann, M. R. Eckart, W. E. Moerner, and L. Shapiro. 2014. Bacterial scaffold directs pole-specific centromere segregation. Proc Natl Acad Sci U S A 111(19):E2046-2055.

83. Hess, S. T., T. P. K. Girirajan, and M. D. Mason. 2006. Ultra-high resolution imaging by fluorescence photoactivation localization microscopy. Biophysical journal 91(11):4258-4272.

84. Heilemann, M., S. van de Linde, M. Schuttpelz, R. Kasper, B. Seefeldt, A. Mukherjee, P. Tinnefeld, and M. Sauer. 2008. Subdiffraction-resolution fluorescence imaging with conventional fluorescent probes. Angewandte Chemie International Edition 47(33):6172-6176. Article.

85. van de Linde, S., M. Sauer, and M. Heilemann. 2008. Subdiffraction-resolution fluorescence imaging of proteins in the mitochondrial inner membrane with photoswitchable fluorophores. Journal of Structural Biology 164(3):250-254. Article.

86. Biteen, J. S., M. A. Thompson, N. K. Tselentis, G. R. Bowman, L. Shapiro, and W. E. Moerner. 2008. Super-resolution imaging in live *Caulobacter crescentus* cells using photoswitchable EYFP. Nature Methods 5(11):947-949.

87. Brown, J. K., A. D. Pemberton, S. H. Wright, and H. R. P. Miller. 2004. Primary Antibody–Fab Fragment Complexes: A Flexible Alternative to Traditional Direct and Indirect Immunolabeling Techniques. Journal of Histochemistry & Cytochemistry 52(9):1219-1230.

88. Keppler, A., H. Pick, C. Arrivoli, H. Vogel, and K. Johnsson. 2004. Labeling of fusion proteins with synthetic fluorophores in live cells. Proceedings of the National Academy of Sciences of the United States of America 101(27):9955.

89. Gautier, A., A. Juillerat, C. Heinis, I. R. Corrêa, M. Kindermann, F. Beaufils, and K. Johnsson. 2008. An Engineered Protein Tag for Multiprotein Labeling in Living Cells. Chemistry & Biology 15(2):128-136.

90. Los, G. V., L. P. Encell, M. G. McDougall, D. D. Hartzell, N. Karassina, C. Zimprich, M. G. Wood, R. Learish, R. F. Ohana, M. Urh, D. Simpson, J. Mendez, K. Zimmerman, P. Otto, G. Vidugiris, J. Zhu, A. Darzins, D. H. Klaubert, R. F. Bulleit, and K. V. Wood. 2008. HaloTag: A Novel Protein Labeling Technology for Cell Imaging and Protein Analysis. research-article.

91. Bates, M., B. Huang, G. T. Dempsey, and X. W. Zhuang. 2007. Multicolor super-resolution imaging with photo-switchable fluorescent probes. Science 317(5845):1749-1753.

92. Egner, A., C. Geisler, C. von Middendorff, H. Bock, D. Wenzel, R. Medda, M. Andresen, A. C. Stiel, S. Jakobs, C. Eggeling, A. Schönle, and S. W. Hell. 2007.

Fluorescence Nanoscopy in Whole Cells by Asynchronous Localization of Photoswitching Emitters. Biophysical Journal 93(9):3285-3290.

93. Smith, C. S., N. Joseph, B. Rieger, and K. A. Lidke. 2010. Fast, single-molecule localization that achieves theoretically minimum uncertainty. Nature Methods 7(5):373-U352. Article.

94. Holden, S. J., S. Uphoff, and A. N. Kapanidis. 2011. DAOSTORM: an algorithm for high- density super-resolution microscopy. Nature Methods 8(4):279-280.

95. Zhu, L., W. Zhang, D. Elnatan, and B. Huang. 2012. Faster STORM using compressed sensing. Nature Methods 9(7):721-723.

96. Cox, S., E. Rosten, J. Monypenny, T. Jovanovic-Talisman, D. T. Burnette, J. Lippincott-Schwartz, G. E. Jones, and R. Heintzmann. 2012. Bayesian localization microscopy reveals nanoscale podosome dynamics. Nature Methods 9(2):195-200.

97. Babcock, H., Y. M. Sigal, and X. Zhuang. 2012. A high-density 3D localization algorithm for stochastic optical reconstruction microscopy. Optical Nanoscopy 1(1):6.

98. Pavani, S. R. P., and R. Piestun. 2008. Three dimensional tracking of fluorescent microparticles using a photon-limited double-helix response system. Optics Express 16(26):22048-22057. Article.

99. Pavani, S. R. P., M. A. Thompson, J. S. Biteen, S. J. Lord, N. Liu, R. J. Twieg, R. Piestun, and W. E. Moerner. 2009. Three-dimensional, single-molecule fluorescence imaging beyond the diffraction limit by using a double-helix point

spread function. Proceedings of the National Academy of Sciences of the United States of America 106(9):2995-2999.

100. Shechtman, Y., L. E. Weiss, A. S. Backer, S. J. Sahl, and W. E. Moerner. 2015. Precise Three-Dimensional Scan-Free Multiple-Particle Tracking over Large Axial Ranges with Tetrapod Point Spread Functions. Nano Lett 15(6):4194-4199.

101. Lew, M. D., S. F. Lee, M. Badieirostami, and W. E. Moerner. 2011. Corkscrew point spread function for far-field three-dimensional nanoscale localization of pointlike objects. Optics Letters 36(2):202-204.

102. Backer, A. S., M. P. Backlund, A. R. von Diezmann, S. J. Sahl, and W. E. Moerner. 2014. A bisected pupil for studying single-molecule orientational dynamics and its application to three-dimensional super-resolution microscopy. Applied Physics Letters 104(19):193701.

103. Jia, S., J. C. Vaughan, and X. Zhuang. 2014. Isotropic three-dimensional super-resolution imaging with a self-bending point spread function. Nature Photonics 8:302.

104. Waldchen, S., J. Lehmann, T. Klein, S. van de Linde, and M. Sauer. 2015. Light-induced cell damage in live-cell super-resolution microscopy. Sci Rep 5:15348.

105. Schneckenburger, H., P. Weber, M. Wagner, S. Schickinger, V. Richter, T. Bruns, W. S. L. Strauss, and R. Wittig. 2011. Light exposure and cell viability in fluorescence microscopy. Journal of Microscopy:no-no.

106. Knight, M. M., S. R. Roberts, D. A. Lee, and D. L. Bader. 2003. Live cell imaging using confocal microscopy induces intracellular calcium transients and

cell death. American Journal of Physiology-Cell Physiology 284(4):C1083-C1089.

107. Stockley, J. H., K. Evans, M. Matthey, K. Volbracht, S. Agathou, J. Mukanowa, J. Burrone, and R. T. Káradóttir. 2017. Surpassing light-induced cell damage in vitro with novel cell culture media. Scientific Reports 7(1):849.

108. Hoebe, R. A., C. H. Van Oven, T. W. Gadella, Jr., P. B. Dhonukshe, C. J. Van Noorden, and E. M. Manders. 2007. Controlled light-exposure microscopy reduces photobleaching and phototoxicity in fluorescence live-cell imaging. Nat Biotechnol 25(2):249-253.

109. Axelrod, D. 2001. Total Internal Reflection Fluorescence Microscopy in Cell Biology. Traffic 2(11):764-774.

110. Huisken, J., J. Swoger, F. Del Bene, J. Wittbrodt, and E. H. K. Stelzer. 2004. Optical Sectioning Deep Inside Live Embryos by Selective Plane Illumination Microscopy. Science 305(5686):1007.

111. Chen, B. C., W. R. Legant, K. Wang, L. Shao, D. E. Milkie, M. W. Davidson, C. Janetopoulos, X. S. Wu, J. A. Hammer, 3rd, Z. Liu, B. P. English, Y. Mimori-Kiyosue, D. P. Romero, A. T. Ritter, J. Lippincott-Schwartz, L. Fritz-Laylin, R. D. Mullins, D. M. Mitchell, J. N. Bembenek, A. C. Reymann, R. Bohme, S. W. Grill, J. T. Wang, G. Seydoux, U. S. Tulu, D. P. Kiehart, and E. Betzig. 2014. Lattice light-sheet microscopy: imaging molecules to embryos at high spatiotemporal resolution. Science 346(6208):1257998.

112. Fadero, T. C., T. M. Gerbich, K. Rana, A. Suzuki, M. DiSalvo, K. N. Schaefer, J. K. Heppert, T. C. Boothby, B. Goldstein, M. Peifer, N. L. Allbritton, A. S.

Gladfelter, A. S. Maddox, and P. S. Maddox. 2018. LITE microscopy: Tilted light-sheet excitation of model organisms offers high resolution and low photobleaching. J Cell Biol 217(5):1869-1882.

113. Meddens, M. B. M., S. Liu, P. S. Finnegan, T. L. Edwards, C. D. James, and K. A. Lidke. 2016. Single objective light-sheet microscopy for high-speed whole-cell 3D super-resolution. Biomedical Optics Express 7(6):2219.

114. Dean, K. M., P. Roudot, C. R. Reis, E. S. Welf, M. Mettlen, and R. Fiolka. 2016. Diagonally Scanned Light-Sheet Microscopy for Fast Volumetric Imaging of Adherent Cells. Biophys J 110(6):1456-1465.

115. Dean, K. M., P. Roudot, E. S. Welf, G. Danuser, and R. Fiolka. 2015. Deconvolution-free Subcellular Imaging with Axially Swept Light Sheet Microscopy. Biophys J 108(12):2807-2815.

116. Gao, L. 2015. Extend the field of view of selective plan illumination microscopy by tiling the excitation light sheet. Opt Express 23(5):6102-6111.

117. Vettenburg, T., H. I. Dalgarno, J. Nylk, C. Coll-Llado, D. E. Ferrier, T. Cizmar, F. J. Gunn-Moore, and K. Dholakia. 2014. Light-sheet microscopy using an Airy beam. Nat Methods 11(5):541-544.

118. Rocha, J. M., and A. Gahlmann. 2019. Single-Molecule Tracking Microscopy - A Tool for Determining the Diffusive States of Cytosolic Molecules. Journal of Visualized Experiments 151(151):e59387.

119. Rocha, J. M., C. J. Richardson, M. Zhang, C. M. Darch, E. Cai, A. Diepold, and A. Gahlmann. 2018. Single-molecule tracking in live Yersinia enterocolitica

reveals distinct cytosolic complexes of injectisome subunits. Integrative Biology 10(9):502-515.

120. Lasker, K., A. von Diezmann, D. G. Ahrens, T. H. Mann, W. E. Moerner, and L. Shapiro. 2018. Phospho-signal flow from a pole-localized microdomain spatially patterns transcription factor activity. bioRxiv.

121. Kapanidis, A. N., S. Uphoff, and M. Stracy. 2018. Understanding Protein Mobility in Bacteria by Tracking Single Molecules. J. Mol. Biol.

122. Elf, J., G. W. Li, and X. S. Xie. 2007. Probing Transcription Factor Dynamics at the Single-Molecule Level in a Living Cell. Science 316(5828):1191-1194.

123. Badrinarayanan, A., R. Reyes-Lamothe, S. Uphoff, M. C. Leake, and D. J. Sherratt. 2012. *In Vivo* Architecture and Action of Bacterial Structural Maintenance of Chromosome Proteins. Science 338(6106):528-531.

124. Mohapatra, S., H. Choi, X. Ge, S. Sanyal, and J. C. Weisshaar. 2017. Spatial Distribution and Ribosome-Binding Dynamics of EF-P in Live Escherichia coli. MBio 8(3).

125. Stracy, M., M. Jaciuk, S. Uphoff, A. N. Kapanidis, M. Nowotny, D. J. Sherratt, and P. Zawadzki. 2016. Single-molecule imaging of UvrA and UvrB recruitment to DNA lesions in living Escherichia coli. Nat Commun 7:12568.

126. Persson, F., M. Lindén, C. Unoson, and J. Elf. 2013. Extracting intracellular diffusive states and transition rates from single-molecule tracking data. Nature Methods 10(3):265-269.

127. Bakshi, S., H. Choi, and J. C. Weisshaar. 2015. The spatial biology of transcription and translation in rapidly growing Escherichia coli. Front Microbiol 6:636.

128. Mustafi, M., and J. C. Weisshaar. 2018. Simultaneous Binding of Multiple EF-Tu Copies to Translating Ribosomes in Live Escherichia coli. mBio 9(1).

129. Stracy, M., C. Lesterlin, F. Garza de Leon, S. Uphoff, P. Zawadzki, and A. N. Kapanidis. 2015. Live-cell superresolution microscopy reveals the organization of RNA polymerase in the bacterial nucleoid. Proceedings of the National Academy of Sciences 112(32):E4390-E4399.

130. Plochowietz, A., I. Farrell, Z. Smilansky, B. S. Cooperman, and A. N. Kapanidis. 2017. In vivo single-RNA tracking shows that most tRNA diffuses freely in live bacteria. Nucleic Acids Res 45(2):926-937.

131. Chen, T. Y., W. Jung, A. G. Santiago, F. Yang, L. Krzeminski, and P. Chen. 2015. Quantifying Multistate Cytoplasmic Molecular Diffusion in Bacterial Cells via Inverse Transform of Confined Displacement Distribution. J Phys Chem B 119(45):14451-14459.

132. Koo, P. K., and S. G. Mochrie. 2016. Systems-level approach to uncovering diffusive states and their transitions from single-particle trajectories. Phys Rev E 94(5-1):052412.

133. Uphoff, S., R. Reyes-Lamothe, F. Garza de Leon, D. J. Sherratt, and A. N. Kapanidis. 2013. Single-molecule DNA repair in live bacteria. Proceedings of the National Academy of Sciences of the United States of America 110(20):8063-8068. Research Support, Non-U.S. Gov't.

134. Bakshi, S., Benjamin P. Bratton, and James C. Weisshaar. 2011. Subdiffraction-Limit Study of Kaede Diffusion and Spatial Distribution in Live Escherichia coli. Biophysical Journal 101(10):2535-2544.

135. Bakshi, S., A. Siryaporn, M. Goulian, and J. C. Weisshaar. 2012. Superresolution imaging of ribosomes and RNA polymerase in live Escherichia coli cells. Molecular Microbiology 85(1):21-38.

136. Thompson, M. A., M. D. Lew, M. Badieirostami, and W. E. Moerner. 2010. Localizing and tracking single nanoscale emitters in three dimensions with high spatiotemporal resolution using a double-helix point spread function. Nano Lett. 10(1):211-218. Article.

137. Tolansky, S. C. F. p. d. N. 1967. Frits Zernike. 1888-1966. Biographical Memoirs of Fellows of the Royal Society 13:393-402.

138. Lew, M. D., A. R. S. von Diezmann, and W. E. Moerner. 2013. Easy-DHPSF open-source software for three-dimensional localization of single molecules with precision beyond the optical diffraction limit. Protocol Exchange:doi:10.1038/protex.2013.1026.

139. Abraham, A. V., S. Ram, J. Chao, E. S. Ward, and R. J. Ober. 2009. Quantitative study of single molecule location estimation techniques. Optics Express 17(26):23352-23373.

140. Huang, F., T. M. P. Hartwich, F. E. Rivera-Molina, Y. Lin, W. C. Duim, J. J. Long, P. D. Uchil, J. R. Myers, M. A. Baird, W. Mothes, M. W. Davidson, D. Toomre, and J. Bewersdorf. 2013. Video-rate nanoscopy using sCMOS camera-specific single-molecule localization algorithms. Nat Meth 10(7):653-658.

141. Hoogendoorn, E., K. C. Crosby, D. Leyton-Puig, R. M. Breedijk, K. Jalink, T. W. Gadella, and M. Postma. 2014. The fidelity of stochastic single-molecule super-resolution reconstructions critically depends upon robust background estimation. Sci Rep 4:3854.

142. Douglass, K. M., C. Sieben, A. Archetti, A. Lambert, and S. Manley. 2016. Super-resolution imaging of multiple cells by optimised flat-field epi-illumination. Nat Photonics 10(11):705-708.

143. Zhao, Z., B. Xin, L. Li, and Z. L. Huang. 2017. High-power homogeneous illumination for super-resolution localization microscopy with large field-of-view. Opt Express 25(12):13382-13395.

144. Paintdakhi, A., B. Parry, M. Campos, I. Irnov, J. Elf, I. Surovtsev, and C. Jacobs-Wagner. 2015. Oufti: An integrated software package for high-accuracy, high-throughput quantitative microscopy analysis. Molecular microbiology.

145. Michalet, X., and A. J. Berglund. 2012. Optimal diffusion coefficient estimation in single-particle tracking. Physical Review E 85(6).

146. Gahlmann, A., and W. E. Moerner. 2014. Exploring bacterial cell biology with single-molecule tracking and super-resolution imaging. Nature Reviews Microbiology 12(1):9-22.

147. Michalet, X. 2010. Mean square displacement analysis of single-particle trajectories with localization error: Brownian motion in an isotropic medium. Phys Rev E Stat Nonlin Soft Matter Phys 82(4 Pt 1):041914.

148. Backlund, M. P., R. Joyner, and W. E. Moerner. 2015. Chromosomal locus tracking with proper accounting of static and dynamic errors. Phys Rev E Stat Nonlin Soft Matter Phys 91(6):062716.

149. Hansen, A. S., M. Woringer, J. B. Grimm, L. D. Lavis, R. Tjian, and X. Darzacq. 2018. Robust model-based analysis of single-particle tracking experiments with Spot-On. Elife 7.

150. Lee, A., K. Tsekouras, C. Calderon, C. Bustamante, and S. Presse. 2017. Unraveling the Thousand Word Picture: An Introduction to Super-Resolution Data Analysis. Chem Rev 117(11):7276-7330.

151. Kapanidis, M. S. C. L. F. G. d. L. S. U. P. Z. A. N. 2015. <StracyKapanidis_2015_RNAPolyInNucleoid.pdf>.

152. Rowland, D. J., H. H. Tuson, and J. S. Biteen. 2016. Resolving Fast, Confined Diffusion in Bacteria with Image Correlation Spectroscopy. Biophys J 110(10):2241-2251.

153. Berglund, A. J. 2010. Statistics of camera-based single-particle tracking. Physical Review E 82(1):011917.

154. Gahlmann, A., J. L. Ptacin, G. Grover, S. Quirin, A. R. S. von Diezmann, M. K. Lee, M. P. Backlund, L. Shapiro, R. Piestun, and W. E. Moerner. 2013. Quantitative Multicolor Subdiffraction Imaging of Bacterial Protein Ultrastructures in Three Dimensions. Nano Lett. 13(3):987-993.

155. Kaniga, K., I. Delor, and G. R. Cornelis. 1991. A wide-host-range suicide vector for improving reverse genetics in Gram-negative bacteria: inactivation of the blaA gene of Yersinia enterocolitica. Gene 109(1):137-141.

156. Thanbichler, M., A. A. Iniesta, and L. Shapiro. 2007. A comprehensive set of plasmids for vanillate- and xylose-inducible gene expression in Caulobacter crescentus. Nucleic Acids Research 35(20):e137-e137.

157. Subach, F. V., G. H. Patterson, S. Manley, J. M. Gillette, J. Lippincott-Schwartz, and V. V. Verkhusha. 2009. Photoactivatable mCherry for high-resolution two-color fluorescence microscopy. Nature Methods 6(2):153-159.

158. Ester, M., H.-P. Kriegel, J. Sander, and X. Xu. 1996. A density-based algorithm for discovering clusters a density-based algorithm for discovering clusters in large spatial databases with noise. In Proceedings of the Second International Conference on Knowledge Discovery and Data Mining. AAAI Press, Portland, Oregon. 226-231.

159. Elowitz, M. B., M. G. Surette, P.-E. Wolf, J. B. Stock, and S. Leibler. 1999. Protein Mobility in the Cytoplasm of Escherichia coli. Journal of bacteriology 181(1):197-203.

160. Kumar, M., M. S. Mommer, and V. Sourjik. 2010. Mobility of cytoplasmic, membrane, and DNA-binding proteins in Escherichia coli. Biophysical journal 98(4):552-559.

161. Thomas, J., G. P. Stafford, and C. Hughes. 2004. Docking of cytosolic chaperone-substrate complexes at the membrane ATPase during flagellar type III protein export. Proceedings of the National Academy of Sciences of the United States of America 101(11):3945-3950.

162. Minamino, T., M. Kinoshita, K. Imada, and K. Namba. 2012. Interaction between FliI ATPase and a flagellar chaperone FliT during bacterial flagellar protein export. Molecular Microbiology 83(1):168-178.

163. Bai, F., Y. V. Morimoto, S. D. Yoshimura, N. Hara, N. Kami-Ike, K. Namba, and T. Minamino. 2014. Assembly dynamics and the roles of FliI ATPase of the bacterial flagellar export apparatus. Sci Rep 4:6528.

164. González-Pedrajo, B., T. Minamino, M. Kihara, and K. Namba. 2006. Interactions between C ring proteins and export apparatus components: a possible mechanism for facilitating type III protein export. Molecular Microbiology 60(4):984-998.

165. McMurry, J. L., J. W. Murphy, and B. González-Pedrajo. 2006. The FliN−FliH Interaction Mediates Localization of Flagellar Export ATPase FliI to the C Ring Complex. Biochemistry 45(39):11790-11798.

166. Crocker, J. C., and D. G. Grier. 1996. Methods of Digital Video Microscopy for Colloidal Studies. Journal of Colloid and Interface Science 179(1):298-310.

167. Balzarotti, F., Y. Eilers, K. C. Gwosch, A. H. Gynnå, V. Westphal, F. D. Stefani, J. Elf, and S. W. Hell. 2017. Nanometer resolution imaging and tracking of fluorescent molecules with minimal photon fluxes. Science 355(6325):606-612.

168. English, B. P., V. Hauryliuk, A. Sanamrad, S. Tankov, N. H. Dekker, and J. Elf. 2011. Single-molecule investigations of the stringent response machinery in living bacterial cells. Proceedings of the National Academy of Sciences of the United States of America 108(31):E365-E373.

169. Montero Llopis, P., O. Sliusarenko, J. Heinritz, and C. Jacobs-Wagner. 2012. In vivo biochemistry in bacterial cells using FRAP: insight into the translation cycle. Biophysical journal 103(9):1848-1859.

170. Mika, J. T., G. van den Bogaart, L. Veenhoff, V. Krasnikov, and B. Poolman. 2010. Molecular sieving properties of the cytoplasm of Escherichia coli and consequences of osmotic stress. Mol Microbiol 77(1):200-207.

171. Parry, B. R., I. V. Surovtsev, M. T. Cabeen, C. S. O'Hern, E. R. Dufresne, and C. Jacobs-Wagner. 2014. The bacterial cytoplasm has glass-like properties and is fluidized by metabolic activity. Cell 156(1-2):183-194.

172. Lill, Y., W. Kaserer, S. Newton, M. Lill, P. Klebba, and K. Ritchie. 2012. Single-molecule study of molecular mobility in the cytoplasm of Escherichia coli. Physical Review E 86(2).

173. Slade, K. M., R. Baker, M. Chua, N. L. Thompson, and G. J. Pielak. 2009. Effects of Recombinant Protein Expression on Green Fluorescent Protein Diffusion in Escherichia coli(). Biochemistry 48(23):5083-5089.

174. Mullineaux, C. W., A. Nenninger, N. Ray, and C. Robinson. 2006. Diffusion of Green Fluorescent Protein in Three Cell Environments in Escherichia Coli. Journal of Bacteriology 188(10):3442-3448.

175. Konopka, M. C., I. A. Shkel, S. Cayley, M. T. Record, and J. C. Weisshaar. 2006. Crowding and Confinement Effects on Protein Diffusion In Vivo. Journal of Bacteriology 188(17):6115-6123.

176. Kruse, G. M. a. J. R. a. E. F.-F. a. N. K. a. P. S. a. K. 2006. Mobility of Min-proteins in Escherichia coli measured by fluorescence correlation spectroscopy. Physical Biology 3(4):255.

177. Huang, B., S. A. Jones, B. Brandenburg, and X. W. Zhuang. 2008. Whole-cell 3D STORM reveals interactions between cellular structures with nanometer-scale resolution. Nature Methods 5(12):1047-1052.

178. Shechtman, Y., S. J. Sahl, A. S. Backer, and W. E. Moerner. 2014. Optimal Point Spread Function Design for 3D Imaging. Physical Review Letters 113(13).

179. Saurabh, S., A. M. Perez, C. J. Comerci, L. Shapiro, and W. E. Moerner. 2016. Super-resolution Imaging of Live Bacteria Cells Using a Genetically Directed, Highly Photostable Fluoromodule. J Am Chem Soc 138(33):10398-10401.

180. Bisson-Filho, A. W., Y.-P. Hsu, G. R. Squyres, E. Kuru, F. Wu, C. Jukes, Y. Sun, C. Dekker, S. Holden, M. S. VanNieuwenhze, Y. V. Brun, and E. C. Garner. 2017. Treadmilling by FtsZ filaments drives peptidoglycan synthesis and bacterial cell division. Science 355(6326):739-743.

181. Liu, H., P. Dong, M. S. Ioannou, L. Li, J. Shea, H. A. Pasolli, J. B. Grimm, P. K. Rivlin, L. D. Lavis, M. Koyama, and Z. Liu. 2018. Visualizing long-term single-molecule dynamics in vivo by stochastic protein labeling. Proc Natl Acad Sci U S A 115(2):343-348.

182. Santiago, A. G., T. Y. Chen, L. A. Genova, W. Jung, A. M. George Thompson, M. M. McEvoy, and P. Chen. 2017. Adaptor protein mediates dynamic pump assembly for bacterial metal efflux. Proc Natl Acad Sci U S A 114(26):6694-6699.

183. Minamino, T., and R. M. Macnab. 2000. FliH, a soluble component of the type III flagellar export apparatus of Salmonella, forms a complex with FliI and inhibits its ATPase activity. Molecular Microbiology 37(6):1494-1503.

184. Akeda, Y., and J. E. Galan. 2004. Genetic Analysis of the Salmonella enterica Type III Secretion-Associated ATPase InvC Defines Discrete Functional Domains. Journal of Bacteriology 186(8):2402-2412.

185. Burgess, J. L., H. B. Jones, P. Kumar, R. T. t. Toth, C. R. Middaugh, E. Antony, and N. E. Dickenson. 2016. Spa47 is an oligomerization-activated type three secretion system (T3SS) ATPase from Shigella flexneri. Protein Sci 25(5):1037-1048.

186. Rocha, J., J. Corbitt, T. Yan, C. Richardson, and A. Gahlmann. 2019. Resolving Cytosolic Diffusive States in Bacteria by Single-Molecule Tracking. Biophysical Journal 116(10):1970-1983.

187. Kim, S. Y., Z. Gitai, A. Kinkhabwala, L. Shapiro, and W. E. Moerner. 2006. Single molecules of the bacterial actin MreB undergo directed treadmilling motion in *Caulobacter crescentus*. Proceedings of the National Academy of Sciences of the United States of America 103(29):10929-10934.

188. Tusk, S. E., N. J. Delalez, and R. M. Berry. 2018. Subunit Exchange in Protein Complexes. J Mol Biol.

189. Leake, M. C., J. H. Chandler, G. H. Wadhams, F. Bai, R. M. Berry, and J. P. Armitage. 2006. Stoichiometry and turnover in single, functioning membrane protein complexes. Nature 443(7109):355-358.

190. Delalez, N. J., R. M. Berry, and J. P. Armitage. 2014. Stoichiometry and Turnover of the Bacterial Flagellar Switch Protein FliN. mBio 5(4):e01216-01214.

191. Delalez, N. J., G. H. Wadhams, G. Rosser, Q. Xue, M. T. Brown, I. M. Dobbie, R. M. Berry, M. C. Leake, and J. P. Armitage. 2010. Signal-dependent turnover of the bacterial flagellar switch protein FliM. Proceedings of the National Academy of Sciences 107(25):11347.

192. Rabut, G., V. Doye, and J. Ellenberg. 2004. Mapping the dynamic organization of the nuclear pore complex inside single living cells. Nature Cell Biology 6(11):1114-1121.